



저작자표시-비영리-변경금지 2.0 대한민국

이용자는 아래의 조건을 따르는 경우에 한하여 자유롭게

- 이 저작물을 복제, 배포, 전송, 전시, 공연 및 방송할 수 있습니다.

다음과 같은 조건을 따라야 합니다:



저작자표시. 귀하는 원저작자를 표시하여야 합니다.



비영리. 귀하는 이 저작물을 영리 목적으로 이용할 수 없습니다.



변경금지. 귀하는 이 저작물을 개작, 변형 또는 가공할 수 없습니다.

- 귀하는, 이 저작물의 재이용이나 배포의 경우, 이 저작물에 적용된 이용허락조건을 명확하게 나타내어야 합니다.
- 저작권자로부터 별도의 허가를 받으면 이러한 조건들은 적용되지 않습니다.

저작권법에 따른 이용자의 권리는 위의 내용에 의하여 영향을 받지 않습니다.

이것은 [이용허락규약\(Legal Code\)](#)을 이해하기 쉽게 요약한 것입니다.

[Disclaimer](#)

Ph.D. DISSERTATION

**Overcoming the Non-ideal Behavior
of Atomic Layer Deposition of SrTiO₃ Thin Films
for DRAM Capacitor**

by

Woongkyu Lee

August 2014

DEPARTMENT OF MATERIALS SCIENCE AND ENGINEERING

COLLEGE OF ENGINEERING

SEOUL NATIONAL UNIVERSITY

**Overcoming the Non-ideal Behavior
of Atomic Layer Deposition of SrTiO₃ Thin Films
for DRAM Capacitor**

Advisor : Prof. Cheol Seong Hwang

by

Woongkyu Lee

A thesis submitted to the Graduate Faculty of Seoul National
University in partial fulfillment of the requirements for the
Degree of Doctor of Philosophy
Department of Materials Science and Engineering

August 2014

Approved

by

Chairman of Advisory Committee : Hyeong Joon Kim

Vice-chairman of Advisory Committee : Cheol Seong Hwang

Advisory Committee : Seungwu Han

Advisory Committee : Seong Keun Kim

Advisory Committee : Sang Woon Lee

Abstract

The current generation DRAM capacitors in mass production employ zirconium oxide as dielectric materials with an interposed alumina layer for leakage current density reducing. However, in order to further scale down DRAM devices to sub 20nm design rules, application of materials with higher dielectric constants is necessary. Although there are many candidate materials such as tantalum oxide, titanium oxide, and so on, strontium titanate (SrTiO_3 , STO) is one of the most promising next generation dielectric materials. In spite of its relatively small energy band gap, the superior dielectric constant of perovskite structured STO gives DRAM technology a real chance to overcome the adversities of extreme scaling. To adopt STO as the dielectric of next generation DRAM capacitors, three prerequisites must be fulfilled; a stable STO atomic layer deposition (ALD) process for good step coverage, easy access to noble metal electrodes such as ruthenium for low leakage current, and high temperature growth modes for in-situ crystallization.

In this study, STO films were grown by ALD with various kinds of Sr and Ti precursors; $\text{Sr}(\text{}^i\text{Pr}_3\text{Cp})_2$, $[\text{Sr}(\text{demamp})(\text{tmhd})]_2$, $\text{Ti}(\text{O-}^i\text{Pr})_2(\text{tmhd})_2$, and $\text{Ti}(\text{Me}_5\text{Cp})(\text{OMe})_3$. The growth behaviors of STO deposition processes with various combinations of these precursors were investigated and film

properties including the electrical properties of fabricated metal-insulator-metal (MIM) capacitors were evaluated.

First, $\text{Sr}(\text{}^i\text{Pr}_3\text{Cp})_2$ and $\text{Ti}(\text{O-}^i\text{Pr})_2(\text{tmhd})_2$ were employed for the Sr and Ti precursors, respectively, for the deposition of ALD STO. Through previous studies with the same precursors, Sr excess incorporation was observed during the initial stage of STO deposition on Ru substrates. Initial Sr overgrowth caused strontium carbonate formation which was undesirable since this not only made precise control of thickness difficult, but also aggravated the electrical properties of resultant MIM capacitors. Since the violent reaction between the gas phase $\text{Sr}(\text{}^i\text{Pr}_3\text{Cp})_2$ and the oxygen ion containing Ru substrate was pointed out as the main cause of this unwanted abnormal growth, in previous studies, TiO_2 layers with thicknesses larger than 3 nm was deposited before STO deposition to prevent this phenomenon. Interposing the TiO_2 layer was successful in preventing the initial excess growth, but sparing a physical thickness of 3 nm to a buffer TiO_2 film is not a negligible loss in total dielectric property when it comes to DRAM capacitor technology, considering that the whole dielectric film is only 10 nm. Therefore, in this study, Al_2O_3 which has lower oxygen diffusivity than TiO_2 , was adopted instead of TiO_2 for barrier layer to resolve this issue. Only a 0.4-nm-thick Al_2O_3 layer could effectively suppress the initial excessive incorporation of Sr, and a 1-nm-thick Al_2O_3 layer had a blocking effect that was equivalent to that of a 3-nm-thick TiO_2 layer. The STO films

were crystallized in-situ at 370 °C without any additional annealing process by the assistance of a crystallized 3-nm-thick STO seed layer that was pre-deposited and annealed. The bulk dielectric constant of STO calculated by the slope of equivalent oxide thickness vs. physical thickness was 173 on the 1-nm-thick Al₂O₃/Ru substrate. However, the adverse contribution of the Al₂O₃ layers to capacitance was found to be more severe than the TiO₂ layers.

Also, the characteristics of ALD STO films were examined for metal-insulator-metal capacitors, with Cp-based precursors, Sr(iPr₃Cp)₂ and Ti(Me₅Cp)(OMe)₃, employed as the Sr and Ti precursors, respectively. The enhanced reactivity of this Ti precursor compared to Ti(OⁱPr)₂(tmhd)₂ was found to suppress the unwanted excessive incorporation of Sr into the film in situ. Formation of strontium carbonate was also repressed. A possible mechanism for these phenomena is suggested in detail. By controlling the sub-cycle ratio of the SrO and TiO₂ layers, stoichiometric STO could be obtained, even without employing a deleterious reaction barrier layer. This improved the attainable minimum equivalent oxide thickness of the RuO₂/STO/Ru capacitor to 0.39 nm, with acceptable leakage current density ($\sim 9 \times 10^{-8}$ A/cm²). This indicates an improvement of $\sim 46\%$ in the capacitance density compared with previous work. However, the bulk dielectric constant was only about 100 which indicates the possibility to further improve the electrical property of capacitor. Careful analyses carried out on the films

revealed the presence of microdefects in the STO films. The stress generated from the difference between the thermal expansion coefficients of the STO films and the substrate was found to be the main reason for the formation of these anomalies. By adjusting the cooling rate after crystallization annealing of seed layer, the STO films showed an improved bulk dielectric constant of 135, but only with worse interfacial characteristics.

Finally, STO deposition using $[\text{Sr}(\text{demamp})(\text{tmhd})]_2$ and $\text{Ti}(\text{Me}_5\text{Cp})(\text{OMe})_3$ for the Sr and Ti precursors, respectively, was investigated. This Sr precursor portrayed a similar saturated growth rate of SrO films with $\text{Sr}(\text{iPr}_3\text{Cp})_2$. However, there was no portent of abnormal growth behavior in the initial stage of deposition. Although the deposition rate of the STO films was reduced to a certain extent, carbon contamination in STO film was decreased and no evidence of strontium carbonate formation was observed. Moreover, the decreased deposition rate seemed to produce rather denser films and avoid microdefect generation after crystallization annealing. With ideal ALD growth behavior, conformal STO films could be obtained on three dimensional hole structures with aspect ratios of 10:1. Since the observed bulk dielectric constant was ~ 143 , this is still quite promising considering the fact that there is still room available to improve the electrical characteristics of the capacitor by controlling interface properties.

In conclusion, by suppressing the non-ideal initial overgrowth of Sr with an interposed Al₂O₃ layer, in-situ crystallized STO was grown without SrCO₃ formation by adopting a pre-crystallized STO seed layer. Moreover, with a more reactive Ti-precursor, stoichiometric STO was deposited without any barrier layer and the electrical property showed a t_{ox} of 0.39 nm with a leakage current density of 9×10^{-8} A/cm². The microstructure was improved as well by adjusting the annealing condition. Finally, by employing a novel Sr-precursor with appropriate reactivity, ideal ALD growth behavior were acquired with satisfactory dielectric properties and conformal STO films were deposited in hole structures with the aspect ratio of ~10:1.

Keywords: dynamic random access memory, capacitor, dielectric, electrode, SrO, TiO₂, SrTiO₃, Ru, RuO₂, O₃, H₂O, atomic layer deposition, high-k, capacitance, equivalent oxide thickness, leakage current, in-situ crystallization

Student Number: 2009-23050

Woongkyu Lee

Table of Contents

Abstract.....	i
Table of Contents	vi
List of Tables.....	ix
List of Figures	x
List of Abbreviations.....	xvii
1. Introduction	1
1.1. Dynamic Random Access Memory	1
1.2. Atomic Layer Deposition	6
1.3. Bibliography.....	9
2. Controlling Initial Growth of SrTiO₃ Films by Interposing Al₂O₃ Layers.....	10
2.1. Introduction	10
2.2. Experimental	17
2.3. Results and Discussions.....	20
2.4. Summary	44
2.5. Bibliography.....	46

3. Countervailing Excess Growth of Sr with Reactive Ti-precursor	50
3.1. Growth Behavior and Properties of SrTiO ₃ Films.....	50
3.1.1. Introduction	50
3.1.2. Experimental	56
3.1.3. Results and Discussion	60
3.1.4. Summary	87
3.1.5. Bibliography.....	88
3.2. Reducing Microdefects Formation by Adjusting Rapid Thermal Annealing Cooling Rate	91
3.2.1. Introduction	91
3.2.2. Experimental	93
3.2.3. Results and Discussion	95
3.2.4. Summary	113
3.2.5. Bibliography.....	114
4. Atomic Layer Deposition of SrTiO₃ Films with novel Sr-precursor	117
4.1. Introduction	117

4.2. Experimental	123
4.3. Results and Discussions.....	127
4.4. Summary	146
4.5. Bibliography.....	147
5. Conclusion.....	150
Curriculum Vitae.....	153
List of publications	158
Abstract (in Korean)	171

[1] Lee et al., J. Mater. Chem. 22, 15037, 2012.

[2] Lee et al., Chem. Mater. 25, 953, 2013.

[3] Lee et al., Submission preparation.

[4] Lee et al., Submission preparation.

List of Tables

Table 1.1 Electrical properties of major candidate dielectrics ^[5]	5
Table 4.1 Work functions of major electrode materials ^[10-12]	122

List of Figures

Figure 1.1 Schematic diagram of DRAM cell ^[2]	4
Figure 1.2 Schematic diagrams of one atomic layer deposition cycle. (a) A source injection step (b) A source purge step (c) B source injection step (d) B source purge step.....	8
Figure 2.1. Process sequence for the deposition of (a) TiO ₂ , (b) Al ₂ O ₃ , and (c) SrTiO ₃ films.....	19
Figure 2.2 (a) Variations in the layer densities (inset numbers of Sr and Ti atoms) of the STO films deposited on Al ₂ O ₃ barriers as a function of Al ₂ O ₃ barrier thickness and (b) comparison between the blocking effects of the TiO ₂ and Al ₂ O ₃ barriers on Sr incorporation.....	35
Figure 2.3 Variations in the (a) Sr layer density (number of Sr atoms), (b) Ti layer density (number of Ti atoms), and (c) Sr composition of the STO film as a function of STO super-cycle number on Ru, 1-nm Al ₂ O ₃ /Ru, and 3-nm Al ₂ O ₃ /Ru substrates and (d) the variation of Sr composition as a function of Sr/(Sr+Ti) sub-cycle ratio on 1-nm Al ₂ O ₃ /Ru and on 3-nm Al ₂ O ₃ /Ru	36
Figure 2.4 Variations of the Sr composition in the main layer STO as a function of Sr/(Sr+Ti) sub-cycle ratio for main STO layer deposition (a) on the seed layer STO with Sr composition of 55% on 3-nm-thick TiO ₂ /Ru, 1-nm-thick Al ₂ O ₃ /Ru, and 3-nm-thick	

Al ₂ O ₃ /Ru and (b) on the seed layer STO with Sr compositions of 62%, 55%, and 51% on 0.8-nm-thick Al ₂ O ₃ /Ru, 1-nm-thick Al ₂ O ₃ /Ru, and 1.2-nm-thick Al ₂ O ₃ /Ru.....	37
Figure 2.5 Glancing angle mode X-ray diffraction patterns of STO films on the (a) TiO ₂ and (b) Al ₂ O ₃ barriers.....	38
Figure 2.6 The AES depth profiles of (a) 8-nm-thick STO films on the 3-nm-thick TiO ₂ barrier and (b) 10-nm-thick STO films on the 1-nm-thick Al ₂ O ₃ barrier	39
Figure 2.7 Scanning electron microscopy image of (a) the surface and (b) the tilted view cross-section of the 11-nm-thick STO film. The XP spectra of (c) O 1 s and (d) the valence band structure of the 10-nm-thick STO film. Inset figure in (d) shows the AFM topographic image of the 11-nm-thick STO film. The root-mean-squared roughness was only 0.6 nm. All STO films were grown on the 1-nm-thick Al ₂ O ₃ /Ru.....	40
Figure 2.8 Variations of t _{ox} with different Sr composition of the STO main layer with (a) 3-nm-thick TiO ₂ barrier layers and (b) 1-nm-thick Al ₂ O ₃ barrier layers	41
Figure 2.9 Variations of (a) bulk dielectric constant and (b) interfacial t _{ox} extracted from Figure 8 as a function of Sr composition.....	42
Figure 2.10 The leakage current density (@ 0.8 V) vs. t _{ox} plot of STO films with (a) 3-nm-thick TiO ₂ barrier layers and (b) 1-nm-thick Al ₂ O ₃ barrier layers on a Ru substrate.....	43

Figure 3.1 The schematic chemical structures of (a) Ti-A precursor and (b) Ti-B precursor.....	59
Figure 3.2 Variations of Ti layer densities of TiO ₂ films as a function of (a) feeding times and (b) purge times of Ti-B precursor and ozone. 76	76
Figure 3.3 The comparison of (a) thickness and (b) Ti layer densities of TiO ₂ films as a function of deposition cycles deposited by Ti-A precursor and Ti-B precursor.....	77
Figure 3.4 (a) Variations of film thicknesses and growth rates of STO films and (b) variations of layer densities of Sr and Ti in STO films on Ru substrate and on TiO ₂ coated Ru substrate as a function of STO super-cycles (sub-cycle ratio TiO ₂ :SrO = 4:1).	78
Figure 3.5 (a) Comparison of variations of Sr layer densities and (b) cation ratio (Sr / Ti) of STO films as a function of super-cycles deposited with Ti-A precursors (sub-cycle ratio TiO ₂ :SrO = 4:1) and with Ti-B precursors (sub-cycle ratio TiO ₂ :SrO = 3:1) Data for Ti-A precursor case was reproduced from Ref.13.	79
Figure 3.6 The schematic diagrams of the reaction flow of the STO ALD process with Sr(ⁱ Pr ₃ Cp) ₂ as Sr precursor and Ti-A (left hand panel) or Ti-B (right hand panel) precursors as Ti precursor: (a) O ₃ injection step, (b) Ti precursor injection step, (c) O ₃ injection step and (d) Sr precursor injection step. At this stage, TiO ₂ and SrO already diffuse and form SrTiO ₃ even though the schematic figure does not show the inter-diffusion.	80

Figure 3.7 Variations of the cation compositions ($\text{Sr}/(\text{Sr}+\text{Ti})$) of STO films deposited on various substrate with various super-cycles as a function of sub-cycle ratio ($\text{SrO}/(\text{SrO}+\text{TiO}_2)$).....	81
Figure 3.8 The XP spectra of (a) C 1s, (b) O 1s, and (c) valence band structure of STO(11 nm)/Ru and (d) C 1s, (e) O 1s, and (f) valence band structure of STO(6nm) /TiO ₂ -(4 nm)/Ru.	82
Figure 3.9 The AES depth profiles of (a) 6-nm-thick main STO layer with Sr composition of 50% + 3-nm-thick seed STO layer with 55% Sr composition, which was initially 6-nm thick before crystallization annealing; (b) 4-nm-thick main STO layer with Sr composition of 47% + 2-nm-thick seed STO layer with 55% Sr composition, which was 3-nm thick before RTA + 3-nm-thick TiO ₂ barrier layer).....	83
Figure 3.10 Glancing angle mode X-ray diffraction patterns of Ru and RuO ₂ substrates, and STO films on Ru and RuO ₂ substrates.....	84
Figure 3.11 Variations of t_{ox} of STO films deposited with different Ti precursors as a function of t_{phy} and (b) the leakage current density(@0.8 V) versus t_{ox} plot of STO films deposited on Ru substrate with Ti-B precursor. Data for Ti-A precursor case was reproduced from Ref.13.	85
Figure 3.12 The t_{ox} and the dielectric constant and (b) the leakage current density versus applied voltage plot of the in-situ crystallized STO deposited on Ru substrate and on RuO ₂ substrate with Ti-B	

precursor.....	86
Figure 3.13 SEM and AFM image of 14nm thick STO film.....	102
Figure 3.14 SEM and AFM image of (a) STO seed layer (b) annealed STO seed layer (c) STO main layer.....	103
Figure 3.15 The schematic diagram of origins of (a) intrinsic stress induced by grain growth and (b) extrinsic stress induced by temperature increase	104
Figure 3.16 rapid cooling (650 °C → room temperature) and slow cooling (650°C → 500°C 30s → 350°C 30s → 200°C 30s → room temperature) after RTA process.....	105
Figure 3.17 SEM and AFM images with RMS roughness of (a) STO seed layer after slow cooling and (b) STO main layer	106
Figure 3.18 The variations of RMS roughness of sample surface variation at each step.....	107
Figure 3.19 XP Spectra of (a) C 1s and (b) O 1s of STO films with rapid cooling process and slow cooling process	108
Figure 3.20 GAXRD of STO films with rapid cooling process and slow cooling process	109
Figure 3.21 Electrical properties of STO films. (a) Minimum equivalent oxide thickness vs. physical oxide thickness and (b) leakage current density vs. minimum equivalent oxide thickness.	110
Figure 3.22 cross-section TEM image of Pt - in-situ crystallized STO - Ru structure with rapid cooling process	111

Figure 3.23 cross-section TEM image of Pt - in-situ crystallized STO - Ru structure (a) with rapid cooling process and (b) with slow cooling process.....	112
Figure 4.1 The schematic chemical structure of $[\text{Sr}(\text{demamp})(\text{tmhd})]_2$ precursor	126
Figure 4.2 Variation of Sr layer densities of SrO films as a function of feeding times of precursor injection, precursor purge, oxidant injection, and oxidant purge time on (a) Ru, (b) Si, and (c) Pt substrate. (d) Summary of variation of Sr layer density as a function of precursor injection time on Ru, Si, and Pt substrate.	134
Figure 4.3 The comparison of growth behavior of SrO films deposited with $\text{Sr}(\text{iPr}_3\text{Cp})_2$ and $[\text{Sr}(\text{demamp})(\text{tmhd})]_2$ on various substrates....	135
Figure 4.4 (a) Atomic concentration of C and N in SrO films by AES and (b) XP spectra of N 1s in SrO film	136
Figure 4.5 AES depth profile of SrO films deposited by $\text{Sr}(\text{iPr}_3\text{Cp})_2$ and $[\text{Sr}(\text{demamp})(\text{tmhd})]_2$ on Ru, Si, and Pt substrate.	137
Figure 4.6 XP spectra of (a) C 1s, (b) O 1s, and (c) Sr 3d in SrO films deposited by $\text{Sr}(\text{iPr}_3\text{Cp})_2$ and $[\text{Sr}(\text{demamp})(\text{tmhd})]_2$ on Ru, Si, and Pt substrate.....	138
Figure 4.7 Variation of cation composition as a function of (a) subcycle ratio and (b) supercycle ($\text{TiO}_2 : \text{SrO} = 2 : 3$).....	139
Figure 4.8 (a) Variation of layer density of Sr and Ti element and (b) thickness of STO films as a function of supercycle	140

Figure 4.9 XP spectra of (a) C 1s, (b) O 1s, and (d) N 1s of STO films and (c) AES depth profile of STO films.....	141
Figure 4.10 (a) Glancing angle XRD of STO films (b) XRR of as-deposited, ex-situ crystallized, and in-situ crystallized STO films.....	142
Figure 4.11 SEM images of (a) as-deposited, (b) ex-situ crystallized, (c) in-situ crystallized STO films deposited with [Sr(demamp)(tmhd)] ₂ , and (d) ex-situ crystallized STO films deposited with Sr(iPr ₃ Cp) ₂	143
Figure 4.12 Electrical properties of STO films. (a) t _{ox} vs. t _{phy} and (b) J vs. t _{ox}	144
Figure 4.13 (a) Cross-section TEM image of STO films deposited on SiO ₂ hole structure (opening diameter ~100 nm, depth ~1μm, aspect ratio~10:1) and (b) the variation of cation composition of STO films according to the hole position measured by EDS and XRF	145

List of Abbreviations

AES	Auger Electron Spectroscopy
AFM	Atomic Force Microscope
ALD	Atomic Layer Deposition
BE	Bottom Electrode
CBO	Conduction Band Offset
CVD	Chemical Vapor Deposition
C-V	Capacitance-Voltage
DRAM	Dynamic Random Access Memory
E_g	Bandgap
GAXRD	Grazing Angle incidence X-ray Diffraction
I-V	Current-Voltage
J_g	Leakage current density
MIM	Metal-Insulator-Metal
PDA	Post-Deposition Annealing
RAM	Random Access Memory
RTA	Rapid Thermal Annealing
SEM	Scanning Electron Microscope
TE	Top Electrode
TEM	Transmission Electron Microscope
TEC	Thermal Expansion Coefficient
t_{ox}	Equivalent oxide thickness
t_{phy}	Physical oxide thickness
VBO	Valence Band Offset
XPS	X-ray photoelectron Spectroscopy

XRD

X-Ray Diffraction

ϵ_r

Dielectric constant

1. Introduction

1.1. Dynamic Random Access Memory

Dynamic Random Access Memory (DRAM) is the basic device with CPU to be used in wide range of microelectronic device such as a personal computer, workstation, game consol, mobile application, and so on. DRAM was first developed by Rober H. Dennard who was researcher in IBM at 1967.^[1] Until now, DRAM has been the only high density memory device used for about half a hundred years although there have been many candidates to replace it such as FRAM, RRAM, and MRAM for its high density, short read / write / erase time, and many read / write cycles.

One DRAM cell consists of a transistor and a capacitor (1T1C), which operates as a switch and which acts as a charge storage, respectively. Schematic diagrams of DRAM are shown in figure 1.^[2] To write data, the capacitor can be charged or discharged when cell transistor state is ‘turn on’ and the bit line has higher voltage or lower voltage than capacitor, respectively. When the transistor state becomes ‘turn off’, no charge can path through the transistor and capacitor is remained as the information was wrote;

these two charged and uncharged states produce the binary information of ‘1’ and ‘0’.

As the density of DRAM increases, many difficulties occur on both transistor and capacitor to play their role due to its decreasing cell size. Among them, the scaling problem in capacitor was concretely dealt in this research. Capacitance of one memory cell is a significant parameter that determines sensing voltage and speed, data retention time, endurance, and reliability. For normal operation, minimum cell capacitance of 20 ~ 25fF per cell is required regardless of memory density and cell size.^[3] The capacitance is represented as following equation 1.

$$C = \epsilon_r \epsilon_0 A / t \dots \dots \dots \text{equation 1}$$

C, ϵ_r , ϵ_0 , A, and t are the capacitance, dielectric constant of dielectric, permittivity of vacuum, surface area of electrode, and film thickness, respectively. The strategies to increase cell capacitance are the use of 3-dimensional complicated structure with high aspect ratio to increase A, decrease t until the capacitor has limit leakage current and increase ϵ_r by employing material with higher dielectric constant as a dielectric.^[4]

Until current generation DRAM capacitor, from SiO_2 , silicon oxide/nitride composite (ONO), and Al_2O_3 , to ZrO_2 was employed as the dielectric materials. However, these materials have relatively low dielectric constant under 50, which is not sufficient for further device scaling. (table 1)^[5] Even optimized ZrO_2 based dielectric with interposed Al_2O_3 layer to reduce leakage current is facing to the limit nowadays. Therefore, dedicated studies have been made in search of alternative dielectric materials with high permittivity such as TiO_2 and SrTiO_3 (STO). STO is a ternary perovskite structure material made up of one Sr^{2+} , one Ti^{4+} , and three O^{2-} ions. It has a relatively low band gap of 3.2eV, however, the dielectric constant of bulk material is about 300.^[6, 7] There are many dielectric materials which have advantage in leakage current property for their more than twice larger band gap than STO, however, dielectric constant of STO is surprisingly high since other typical dielectrics are mostly near or under 100. Since the capacitor structure is expected to be changed from cylinder to pedestal and the possible aspect ratio is also facing the upper limit, study of ultrahigh dielectric constant material such as STO is necessary.

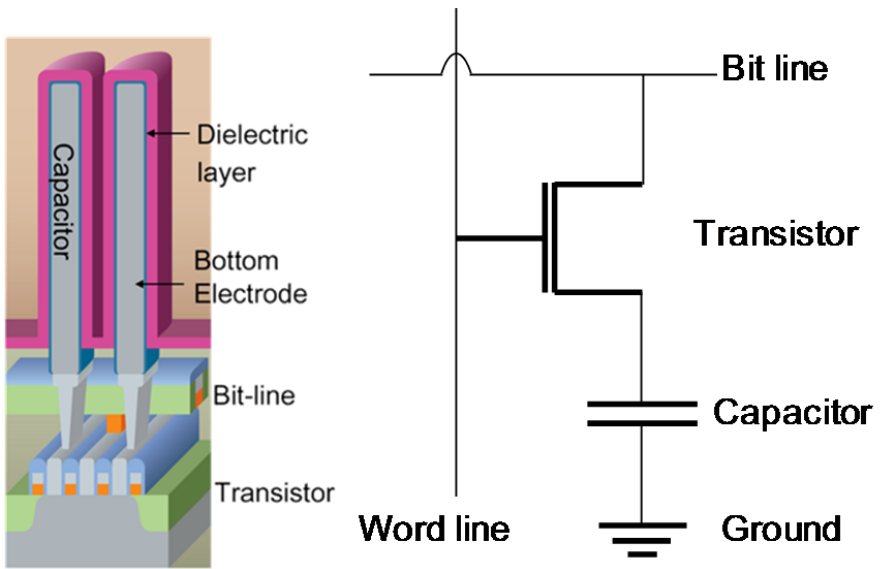


Figure 1.1 Schematic diagram of DRAM cell ^[2]

Table 1.1 Electrical properties of major candidate dielectrics ^[5]

dielectric	dielectric constant	Band gap [eV]	CB offset on Si [eV]
SiO ₂	3.9	9	3.2
Al ₂ O ₃	9	8.8	2.8 (not ALD)
HfO ₂	14-28	5.8	1.4
Ta ₂ O ₅	25-50	4.4	0.35
ZrO ₂	35-50	5.8	1.5
TiO ₂ (anatase)	~40	3.5	0
TiO ₂ (rutile)	80-170	3.5	0
SrTiO ₃	>100	3.2	0

1.2. Atomic Layer Deposition

Atomic Layer Deposition (ALD) is a deposition method which is based on the chemical vapor deposition. The main difference in ALD compared with CVD is separate feeding of precursor and reactant gas to achieve a precise control over film thickness.^[8] One cycle of ALD process is consisted of four steps as shown in figure 2: source injection, purge, another source injection, and purge. Source can be chemical precursor with reactive ligands attached to the target element or reactant such as oxidant or reductant. In ideal case, the thickness of deposited film is dependent only on the number of cycles. Sequential control of the growth in ALD is based on unique characteristics which is self-limiting mechanism between the reaction surface and source. There are two kinds of adsorption when the precursor is exposed to the substrate: physisorption and chemisorption. Physisorbed precursor has weak bonding energy with substrate involving Van der Waals force but chemisorbed precursor forms strong chemical bonds by ionic or covalent bonding with the surface.

At first step, precursor exposed on surface and surface group forms a tight binding monolayer on the surface. The following purge step removes all the physisorbed precursors from the surface. When the next reaction gas is supplied into the chamber, reactant gas faces the surface monolayer and produces the target layer with gas byproducts. The unnecessary byproducts

are purged out through the final step and consequently, only the desired layer remains on the substrate. By repeating these steps for certain cycles, the final wanted film is deposited in the target thickness.

With this deposition method, due to the self-limited mechanism of process, materials grow layer by layer in the shape of substrate structure which is as complex as source molecules can reach to. It does not matter whether the target is three dimensional or not and intensely conformal film can be obtained on high aspect ratio structure.

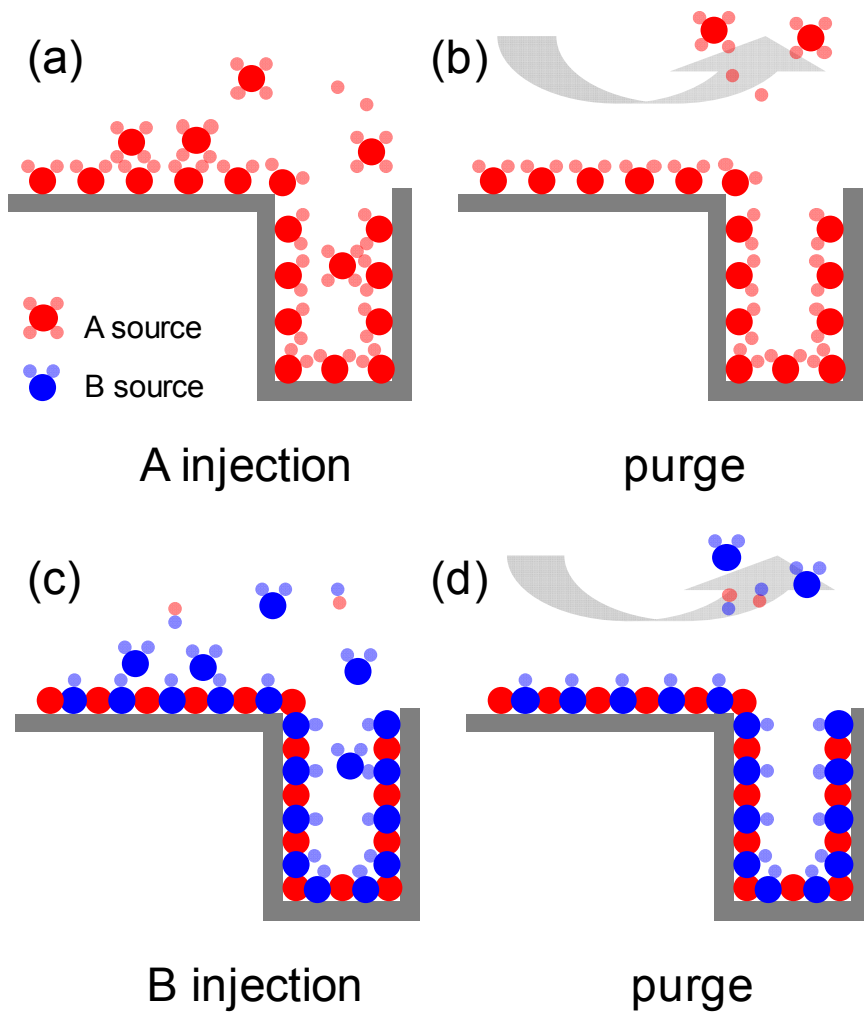


Figure 1.2 Schematic diagrams of one atomic layer deposition cycle. (a) A source injection step (b) A source purge step (c) B source injection step (d) B source purge step

1.3. Bibliography

1. S. K. Kim, S. W. Lee, J. H. Han, B. Lee, S. Han, and C. S. Hwang, Adv. Funct. Mater., 2010, 20, 2989.
2. R. H. Dennard, United States Patent 3387286, July 14, 1967.
3. ITRS roadmap 2013.
4. W. Lee, J. H. Han, S. W. Lee, S. Han, W. J. Jeon, and C. S. Hwang, J. Mater. Chem., 2012, 22, 15037.
5. J. Robertson, Rep. Prog. Phys., 2006, 69, 327.
6. A. Eriksson, A. Deleniv, and S. Gevorgian, J. Appl. Phys. 2003, 93, 2848.
7. R. C. Neville, B. Hoeneisen, and C. A. Mead, J. Appl. Phys. 1972, 43, 2124.
8. C. S. Hwang, "Atomic Layer Deposition for semiconductors", Springer, 2013.

2. Controlling Initial Growth of SrTiO₃ Films by Interposing Al₂O₃ Layers

2.1. Introduction

Development of highly scaled dynamic random access memory (DRAM) to a design rule < 20 nm has been hindered by the difficulty of fabricating a cell capacitor with sufficient capacitance (25 fF/cell).^[1] Since $C = \epsilon_r \epsilon_0 A/d$, where C , ϵ_r , ϵ_0 , A and d are the cell capacitance, dielectric constant, vacuum permittivity, area of overlap of the two electrodes, and dielectric thickness, respectively, keeping the capacitance at a sufficiently high level becomes extremely difficult since the cell size shrinks dramatically. The current dielectric material for DRAM mass production is ZrO₂/Al₂O₃/ZrO₂ dielectric stack in which TiN top and bottom electrodes are adopted.^[2] Perhaps the next generation dielectric material is TiO₂-based materials such as the Al-doped TiO₂ (ATO)^[3] with Ru or RuO₂ electrodes.^[3-7] However, the reported minimum oxide equivalent thickness (t_{ox}) of the ATO remains at 0.46 nm^[4], which is not sufficiently small for the DRAM with design rules < 20 nm. Therefore, SrTiO₃ (STO) film, which has a higher bulk ϵ_r grown by atomic layer deposition (ALD) becomes an important research topic.

There have been many reports on this topic, and several representative results have recently been summarized.^[1] The key features are described briefly below. The achievement of a well-saturated ALD process is generally dependent on the availability of appropriate precursors. There is much variety in the available Ti precursors, but Sr has scarcely been reported due to its large atomic size and heavy weight. There are 2 commonly reported Sr precursors: $\text{Sr}(\text{tmhd})_2$ ($\text{Sr}(\text{C}_{11}\text{H}_{19}\text{O}_2)_2$) (tmhd = 2,2,6,6-tetramethyl-3,5-heptanedione) and cyclopentadienyl (C_5H_5 , Cp) ring-based precursors like $\text{Sr}(\text{}^i\text{Pr}_3\text{Cp})_2$ in which ${}^i\text{Pr}$ refers to the isopropyl ligand. The variously available Ti precursors contain alkoxides, amines, amidinates, β -diketonates, and Cp compounds.

$\text{Sr}(\text{tmhd})_2$ has been reported to have limited ALD reactivity with H_2O .^[8] However, when the $\text{Sr}(\text{tmhd})_2$ precursor was vaporized at temperatures < 200 °C (typically 180–190 °C) to suppress the oligomerization, fluent ALD reaction with H_2O forming SrO was achieved.^[9] Therefore, STO films were achieved by combination with the TiO_2 ALD steps in which Ti-tetraisopropoxide ($\text{Ti}(\text{O}^i\text{Pr})_4$ [TTIP]) was used at a typical growth temperature (T_g) of 250 °C.^[9] Another earlier report on the ALD and STO was made by a group at Helsinki University, where the $\text{Sr}(\text{}^i\text{Pr}_3\text{Cp})_2$ and several Ti-alkoxides were used as the Sr and Ti precursors, respectively, with H_2O as the oxygen source at T_g near 250–325 °C in which thermal decomposition of the Sr precursor was not observed.^[10] The Cp-based Sr precursor showed a fluent

ALD reaction with H₂O due to the weaker bonding energy between the Cp ring and the Sr metal ion. In both cases, conformal film depositions on the three-dimensional structure have been achieved using the fluent ALD reactions.

However, the as-grown films were mostly amorphous with a fairly low density compared to the theoretical value, which caused a serious problem during crystallization by post-deposition annealing (PDA). PDA at temperatures > ~600 °C also results in significant thickness shrinkage (~70–80% of the original thickness),^[11] which evidently degraded the leakage current density. These discouraging properties were attributed mainly to the low ALD temperature (< ~280 °C) due to the limited thermal stability of the alkoxide-based Ti precursor used, even though the Sr precursors generally have much higher thermal decomposition temperature (~400 °C). It was reported that in situ crystallization with a fine grain size (<< ~50 nm in diameter) is very important to achieving a reliable leakage current property from the STO film.^[12] The in situ crystallization requires a higher T_g (minimum ~ 450 °C), even in sputtering^[12] and metal-organic chemical vapor deposition.^[13]

On the other hand, Pawlak et al. reported ALD of Sr-rich STO, which is adopted to reduce the cracking-related leakage problem, deposited at 250 °C using Sr(^tBu₃Cp)₂ and Ti(OMe)₄ as Sr and Ti precursors, respectively, where

^tBu and Me refer to tertiary butoxy and methoxy ligands, respectively, and H₂O as the oxygen source. To compensate for the Ti deficiency, they employed a 1-nm-thick TiO₂ layer interposed between the Sr-rich STO layer and oxidized Ru layer to make the composition stoichiometric after being intermixed by the PDA for the crystallization. The Sr-rich STO film crystallized with small grain size and showed plausible dielectric performance.^[14]

A rather different approach was to adopt a different Ti precursor, the thermal decomposition temperature of which is much higher, such as Ti(O-ⁱPr)₂(tmhd)₂ (Ti(O-*i*-C₃H₇)₂(C₁₁H₁₉O₂)₂), which showed a thermal decomposition behavior at ALD temperatures > ~390 °C.^[15] Lee et al. showed ALD of STO film using Sr(tmhd)₂ and Ti(O-ⁱPr)₂(tmhd)₂ with H₂O at growth temperatures up to 390 °C (typically at 370 °C) on a Ru substrate. The film density increased significantly with no notable thickness shrinkage after PDA. Due to the still not high enough growth temperature, however, the as-grown film was also amorphous on the non-lattice-matched Ru electrode, and the PDA resulted in a large grain size (>>100 nm in diameter) and micro- or nano-scale cracks. In situ crystallization during the film growth was attempted using a so-called two-step process in which the thin crystallized (~3–5 nm) layer of STO was deposited first followed by ALD of the main STO layer (> ~10 nm). The thin crystallized STO layer (called the seed layer) can be grown by ALD at 370 °C, at which temperature the film is still amorphous, followed

by crystallization annealing at 650–700 °C. Due to local lattice matching between the crystallized seed layer and the main layer, the overall film was crystallized in situ with an average grain size of $\ll \sim 50$ nm and very promising electrical properties.^[15,16] However, the slow growth rate of the STO films (typically ~ 0.015 nm/cycle) was not compatible with the mass-production process. This was mainly attributed to the slow growth rate of the SrO layer, which might be due to either a higher bonding energy between the β -diketone ligand with the metal ions or the bulkiness of the Sr precursors.

The authors therefore selected $\text{Sr}(\text{}^i\text{Pr}_3\text{Cp})_2$ and $\text{Ti}(\text{O-}^i\text{Pr})_2(\text{tmhd})_2$ as the metal precursors.^[17] In this study, O_3 and H_2O were used as the oxygen source for the growth of the TiO_2 and SrO layers, respectively. It was found that the $\text{Sr}(\text{}^i\text{Pr}_3\text{Cp})_2$ precursor was prone to thermal decomposition at temperatures as low as 320 °C when they were pulsed on the OH-terminated surface. Therefore, O_3 was used as the oxygen source for the TiO_2 layer because the $\text{Sr}(\text{}^i\text{Pr}_3\text{Cp})_2$ precursor was pulsed on the (O_3 -pulsed) TiO_2 terminated surface during ALD. When this process sequence was adopted, the decomposition temperature of $\text{Sr}(\text{}^i\text{Pr}_3\text{Cp})_2$ was increased to ~ 390 °C.^[17] The stoichiometric STO films were achieved by appropriate control of the pulse ratio of each sub-cycle for the SrO and TiO_2 layers and an approximate saturation growth rate of ~ 0.1 nm/cycle, 6–7 times higher than the previous case, was achieved at a T_g of 370 °C. This process also requires a crystallized seed layer of STO to achieve the in situ crystallization.

This ALD process invoked another complication in film composition control, which is the main research topic of this work; the incorporation of Sr onto the Ru surface was strongly enhanced compared to the TiO₂ layer, resulting in a Sr-rich composition at the film–Ru interface.^[17] This finding was attributed to the following. During the early ALD stage of the STO film, the surface Ru layer oxidized, especially when the O₃ was pulsed.^[18,19] The surface RuO_x was prone to reduction during the subsequent metal precursor pulse steps. The weaker binding energy between the Cp ligands and the Sr ion would make the Sr ion react more easily with the oxygen atoms provided from the reduction of the RuO_x compared with the stronger Ti–O bond between the tmhd ligand and the Ti ion in the Ti precursor. Therefore, Sr-rich composition was achieved, which is even more activated at a high T_g (370 °C).

Similar enhancement of the ALD rate during the initial stage by the surface oxygen was also observed in TiO₂.^[19] This phenomenon prevented precise composition control of the stoichiometric Sr/Ti ratio and achieving promising electrical properties at thinner films (<10 nm). Therefore, the Ru surface was coated with a ~3-nm-thick TiO₂ layer prior to the STO seed layer growth (4 nm thick), which can suppress the enhanced Sr incorporation. As a result, STO films with a bulk ϵ_r value as high as 146 was achieved.^[17] However, the achieved minimum t_{ox} was maintained at 0.68 nm (from a 12.2-nm-thick film) while the leakage current density (J) value was maintained as low as $\sim 2 \times 10^{-8}$ Acm⁻² at -1.0–1.0 V.^[17] Further decreases in film thickness did not result in t_{ox}

reduction but did increase the J value. This finding was attributed to the presence of the relatively thick barrier TiO₂ layer, for which the ϵ_r is relatively low. It was attempted to reduce the barrier layer thickness, but 3 nm appeared to be the minimum required to achieve a sufficient barrier effect.^[20]

In this study, another thinner material that had a better diffusion barrier property against oxygen diffusion, ALD Al₂O₃, was adopted. Since the diffusivity of oxygen in TiO₂ and Al₂O₃ is $7.2 \times 10^5 \text{ nm}^2/\text{s}$ ^[21] and $0.45 \text{ nm}^2/\text{s}$ ^[22], respectively, at 900 °C, the blocking effect of the Al₂O₃ layer between the Sr precursor and oxygen from the Ru substrate is expected to be stronger than that of TiO₂ layer. This was confirmed previously for the ALD of TiO₂ on Ru even at a low temperature of 250 °C.^[23] In this study, growth behavior and electrical properties of STO films on the Al₂O₃ barrier layers were examined, and the results are compared with those on the TiO₂ barrier layer. In the meantime, it was believed that the ALD Al₂O₃ layer having a relatively low density and amorphous structure may not have such a $\sim 10^6$ times higher oxygen barrier effect than TiO₂ although the reported diffusivity of bulk materials differs by that amount.

2.2. Experimental

A traveling wave-type ALD reactor (CN-1 Co, Plus-100) for a 4-in-diameter single wafer was used to grow the TiO₂, Al₂O₃, and STO films. Sr(i-Pr₃Cp)₂, Ti(Oⁱ-Pr)₂(tmhd)₂, (synthesized by Air Liquide Co.) and Al(CH₃)₃ were used as the Sr, Ti, and Al precursors, respectively. The canisters of the Ti and Sr precursors were heated to 130 and 90 °C, respectively, while that of the Al precursor was cooled to 3 °C to achieve the appropriate vapor pressures. The Sr and Ti precursors were delivered to the ALD chamber with the assistance of Ar carrier gas at a flow rate of 200 sccm through bubblers, and the working pressure of the ALD reactor was 0.7 Torr. H₂O and O₃ were used as the oxygen source for the SrO and TiO₂ sub-layers, respectively.^[17] H₂O was cooled to 3 °C to control its high vapor pressure, and the concentration of ozone was 250 g/m³. Figures 1 (a)-(c) show the ALD process sequences of TiO₂, Al₂O₃, and STO thin films. Every ALD sub-cycle process, except Al₂O₃ deposition, consisted of precursor feeding (3s) - Ar purge (5s) - oxygen source feeding (2s) - Ar purge (5s), which was confirmed to be consistent with the saturated ALD conditions. The super-cycles of STO deposition consist of ALD sub-cycles of SrO and TiO₂ layers with different cycle ratios to vary the cation composition. The STO films were grown at a T_g of 370 °C. Different thicknesses of the Al₂O₃ barrier layer were deposited at the same T_g using O₃

as the oxygen source by varying the number of deposition cycles. The $\text{Al}(\text{CH}_3)_3$ pulse time was 0.5 s and other conditions were the same as in the STO process. Sputter-deposited Ru(30 nm)/ Ta_2O_5 (8 nm)/thermally oxidized SiO_2 (100 nm)/Si wafers were used as substrates. Crystallization-annealing of the thin seed STO layer was performed in a rapid thermal annealing (RTA) system at 650 °C for 2 minutes in a pure N_2 atmosphere (purity > 99.99%).

The physical thickness of the STO films was measured using an ellipsometer, and the layer density and cation composition were confirmed by X-ray fluorescent spectroscopy (XRF, Themoscscientific, ARL Quant'X). The impurity concentration, including carbon, in the films and the depth profile were examined by Auger electron spectroscopy (AES, Perkin-Elmer, PHI 660). The film surface morphology was examined using field-emission scanning electron microscopy (FESEM, Hitachi, S-4800) and atomic force microscopy (AFM, JEOL, JSPM-5200).

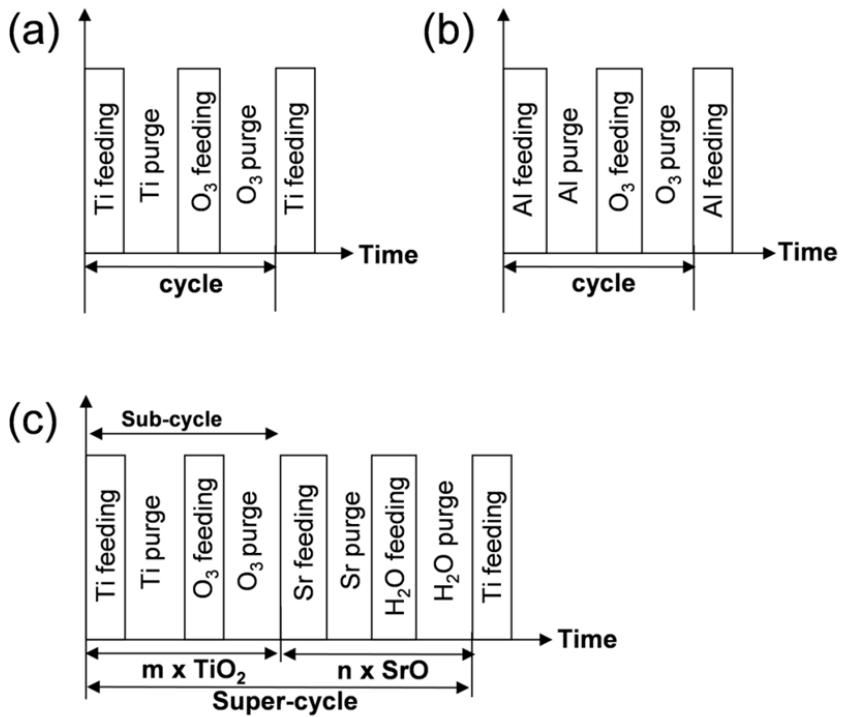


Figure 2.1. Process sequence for the deposition of (a) TiO_2 , (b) Al_2O_3 , and (c) SrTiO_3 films

2.3. Results and Discussions

Figure 2 (a) shows the variations in the layer densities of the Sr and Ti of the STO films deposited (14 super-cycles with a Ti:Sr cycle ratio of 3:1) on the Al₂O₃ barriers as a function of the Al₂O₃ barrier thickness (t_b^{AlO}). The inset figure is the same data, representing the numbers of each atoms converted from the layer densities and the atomic numbers. The layer density of the Sr was very high when there was no Al₂O₃ barrier, which is consistent with an earlier report [17], and it decreased abruptly with increasing t_b^{AlO} values up to ~2 nm and then saturated at a constant value. On the other hand, the layer density of Ti does not change at all over the entire t_b^{AlO} , suggesting that the Ru substrate has negligible influence on the incorporation of Ti into the film. Lee et al. previously reported that TiO₂ growth on Ru using the same precursors and process temperature results in enhanced Ti incorporation during the early stage of film growth.[19] Therefore, the lack of initial increases in Ti incorporation shown in Fig. 2 (a) suggests that the oxygen supplied from the Ru(O) substrate is mostly consumed by Sr atoms, which have higher oxidation potential than Ti atoms. Figure 2 (b) compares the blocking effects of the TiO₂ and Al₂O₃ barriers on Sr incorporation. Although both barrier layers show the blocking effect on the excessive Sr deposition and a constant Sr deposition was observed at thick enough barrier thicknesses, saturation was observed when the Al₂O₃ and TiO₂ barriers were ~2–3 and ~3–4 nm thick,

respectively, suggesting that the Al_2O_3 had a more efficient barrier effect. The 3–4 nm of the effective TiO_2 barrier thickness also coincides with the report by Lee et al.^[17] This is ascribed to the lower diffusivity of oxygen in Al_2O_3 compared to TiO_2 as mentioned earlier.

The non-ideal structure of Al_2O_3 (amorphous structure and lower density) film induced not so evident improvement compared to the much lower bulk diffusivity. However, only 0.5–1-nm-thick Al_2O_3 barrier layer results in the similar Sr layer density to that of the 3–4-nm-thick TiO_2 barrier layer. Another interesting finding is that the saturation levels of Sr layer density, even for the given STO ALD conditions, are different; it is higher on the TiO_2 barrier layer than that on the Al_2O_3 barrier layer. Since the fact that a saturated growth of Sr at thick enough TiO_2 and Al_2O_3 barrier layers is achieved reveals that the oxygen diffusion from the underlying Ru(O) layer is completely blocked, this discrepancy must be understood from the inherently different affinity of the two barriers for the ALD of the SrO layer. The lower affinity of the Al_2O_3 layer compared to the TiO_2 layer might also be ascribed to the lower probability of it supplying oxygen due to the stronger bonding energy between the Al and O atoms compared to that between Ti and O atoms, although the other possibility cannot be completely excluded. Similar retardation of the TiO_2 layer growth on the Al_2O_3 surface, whereas enhancement of Al_2O_3 on the TiO_2 surface was observed in the ALD of Al-doped TiO_2 .^[24] The negligible influence of Al_2O_3 layer thickness on the Ti

incorporation shown in Fig. 2 (a) suggests that the oxygen take-up effect from the barrier layer itself is mostly committed by Sr atoms, a finding that is consistent with the results from the substrate Ru(O) layer.

Because the t_b^{AlO} of 1 nm results in an Sr layer density that is necessary to form the stoichiometric composition of STO film, this thickness of the Al_2O_3 barrier layer was adopted and more detailed ALD behavior of STO film on this Al_2O_3 barrier layer was examined. Figures 3 (a) and (b) show the variation in the Sr and Ti layer densities of the STO film as a function of STO super-cycle number on Ru, on 1-nm $\text{Al}_2\text{O}_3/\text{Ru}$, and on 3-nm $\text{Al}_2\text{O}_3/\text{Ru}$ substrates. Here, the Ti:Sr sub-cycle ratio was 3:1. The growth rate of Sr was sensitively affected by substrate type due to the different supply rate of the O atoms from the substrates. As reported previously, the Sr incorporation on bare Ru was substantially enhanced during the initial stage of film growth up to 2 super-cycles and was saturated afterwards. The abrupt decrease in the Sr growth rate at ~ 3 super-cycles on Ru suggests that the Ru substrate is effectively covered by the growing STO film and that the oxygen diffusion effect was blocked by the grown STO film (5.5–6-nm thickness). Only the 1-nm-thick Al_2O_3 layer abruptly decreased the initial fast growth, and the 3-nm-thick Al_2O_3 layer almost completely blocked the excessive Sr growth. Although these results qualitatively matched the data shown in Figs. 2(a) and (b), there are several quantitative discrepancies as described below. The growth rates of Sr calculated by the saturated slope of the Sr layer density

versus the super-cycle were $0.057 \mu\text{g}/\text{cm}^2\text{cy}^{-1}$, $0.050 \mu\text{g}/\text{cm}^2\text{cy}^{-1}$, and $0.039 \mu\text{g}/\text{cm}^2\text{cy}^{-1}$ for Ru, 1-nm $\text{Al}_2\text{O}_3/\text{Ru}$, and 3-nm $\text{Al}_2\text{O}_3/\text{Ru}$, respectively. Since the oxygen effect from the substrate can be disregarded for the Ru case over the 3 super-cycles and over entire super-cycles for the 3-nm $\text{Al}_2\text{O}_3/\text{Ru}$ case, the different saturation growth rates represent the genuine ALD rate of the Sr-O layer.

Due to the excessive incorporation of Sr during the initial two to three super-cycles, the overall composition of the STO film is very Sr-rich on the Ru substrate (Fig. 3 (c)), suggesting that the Sr-rich composition further enhances the Sr incorporation. The exact reason for this behavior is not yet clearly understood. The intermediate saturation growth rate on the 1-nm $\text{Al}_2\text{O}_3/\text{Ru}$ reflects the non-negligible contribution from the oxygen diffusion through the 1-nm-thick Al_2O_3 and slightly Sr-rich composition of these STO films. On the other hand, the Ti layer density increases linearly at an almost identical increase rate irrespective of substrate type or the number of super-cycles (Fig. 3 (b)). This means that the excessively supplied oxygen atoms are mostly consumed by the Sr precursors, a finding that is in accordance with the results shown in Fig. 2 (a), and that the Ti incorporation rate is independent of Sr composition. According to these effects, the cation composition ratios of the growing STO films have different values depending on substrate type and the number of super-cycles as shown in Fig. 3 (c), even under the given deposition conditions. Figure 3 (d) shows the variation of the Sr composition

(Sr composition [at%] = (# of Sr atom)/{(# of Sr atom)+(# of Ti atom)}) as a function of the Sr/(Sr+Ti) sub-cycle ratio on 1-nm Al₂O₃/Ru and 3-nm Al₂O₃/Ru, respectively. The Sr composition almost linearly increased with increasing Sr sub-cycle ratio for both substrates. As can be expected, the Sr composition of the films on the 1-nm Al₂O₃/Ru was generally high due to the higher substrate oxygen effect, but the difference decreases as the Sr sub-cycle ratio increases. This phenomenon is due to the enhanced Sr incorporation effect on the Sr-rich surface even on the 3-nm Al₂O₃/Ru substrate as the Sr/(Sr+Ti) sub-cycle ratio increased.

As discussed in the Introduction section, the in-situ crystallization of the STO film is crucial to achieving the promising electrical performance, which requires adoption of the crystallized STO seed layer (typically ~3-nm-thick). The crystallized STO seed layer can be achieved by depositing a thin stoichiometric STO layer and rapid thermal annealing under an N₂ atmosphere at 650 °C for 2 minutes. It is desirable to have the identical cation composition ratio of the main STO layer as that of the seed STO layer when they were deposited under the same conditions. However, the structure and chemical composition of seed STO layer are modified by the RTA step, which in turn influences the deposition of main STO layer. The modification in the seed STO layer during the RTA was influenced also by the barrier layer underneath. Therefore, the influences of seed layer composition, types of the barrier layer underneath the seed layer, and thermal treatment on the growth

of main layer STO were carefully examined. The influences of the seed layer on the growth behavior of the main STO layer, which is typically 4-nm-thick in this case, were examined as shown in Fig. 4. Here, the Sr compositions of only main STO layer were estimated by subtracting the XRF signal intensity of the seed layer (and barrier layer for the TiO₂ case) from the total measured XRF signal intensities.

Figure 4 (a) shows the variation of the Sr composition in the main STO layer as a function of the Sr/(Sr+Ti) sub-cycle ratio (for main STO layer deposition). Here, the 3-nm-thick TiO₂ and 1- and 3-nm-thick Al₂O₃ barriers were deposited on Ru first, and the 4-nm-thick STO seed layers were deposited and crystallized by RTA prior to the main layer STO deposition. The thickness of crystallized STO seed layer should be reduced to 2–3 nm considering the thickness change by densification. To make the seed STO layer composition identical, the Ti:Sr sub-cycle ratio of 2:1 was adopted on 3-nm-thick TiO₂ and 1-nm-thick Al₂O₃ barrier layers, while that of 3:2 was used for the 3-nm-thick Al₂O₃ barrier layer. These cycle ratios result in identical Sr composition (~55%) of the seed layer. It is interesting to note that the main STO layers on the 1- and 3-nm-thick Al₂O₃ barrier layers have similar Sr compositions (difference of <5%) as opposed to the results shown in Fig. 3 (d), where the Sr composition difference of the seed STO layers was ~10% in the similar input Sr/(Sr+Ti) sub-cycle ratio range. Here, the Sr composition of the

main layer STO on the seed STO/3-nm Al₂O₃ barrier is generally higher for the given Sr:Ti sub-cycle ratio compared to the data shown in Fig. 3 (d).

Since the oxygen diffusion from the Ru(O) substrate was already stopped by the 3-nm-thick Al₂O₃, which is believed to have remained intact even after the annealing at 650 °C, this increase in the Sr composition of the main layer STO is due to the better growth behavior of Sr–O layer on STO compared to that on the Al₂O₃ surface. The Sr composition of the main STO layer on the seed STO/1-nm Al₂O₃ barrier is generally comparable with the data shown in Fig. 3 (d) under the given ALD conditions. This finding suggests that the 3-nm-thick crystallized seed layer plays partly as an oxygen diffusion barrier (in addition to the 1-nm-thick Al₂O₃), so that the enhanced Sr incorporation on the seed STO layer compared to that on the amorphous Al₂O₃ layer must be compensated by the decreased oxygen effect. However, the results on the 3nm-thick TiO₂ barrier layer show a very distinctive trend, a much higher Sr composition over the entire Sr/(Sr+Ti) sub-cycle ratio range, although the barrier layer was supposed to suppress the oxygen diffusion sufficiently.

Considering that the seed STO layer has the same chemical composition as to the other two cases, this must be ascribed to the degraded barrier performance of the TiO₂ layer as well as the seed STO layer by the RTA. The easier crystallization property, which will induce the grain boundary formation, and the lower melting point of TiO₂ compared to those of

amorphous Al_2O_3 may degrade its diffusion barrier property during the RTA and main layer deposition. Therefore, the STO could have a higher oxygen supply from the substrate through the degraded TiO_2 layer, which eventually results in the higher Sr composition. Another possibility is as follows: the as-deposited seed layer with slightly Sr-rich composition may react with the underlying TiO_2 barrier during the RTA, which may form a well crystallized and rather thick STO layer (5–6 nm) and may contain high-density micro- or nano-cracks. This can also largely degrade the oxygen barrier property of the supposed STO/ TiO_2 seed layer, and the overgrowing main STO layer ultimately has a high Sr concentration, even in the presence of the TiO_2 barrier layer.

Figure 4 (b) shows slightly different experimental results on the barrier effect of the Al_2O_3 layers with different thicknesses. Here, the 0.8-, 1-, and 1.2-nm-thick Al_2O_3 layers were deposited and the ~4-nm-thick seed STO layer was deposited with a given Ti:Sr sub-cycle ratio of 2:1. Due to the insufficient oxygen blocking effect of the three different Al_2O_3 layers, the seed STO layer has the Sr compositions of 62, 55, and 51% on the 0.8-, 1-, and 1.2-nm-thick Al_2O_3 layers, respectively. The main STO layer, which is also 4 nm thick, has a different Sr composition (Fig. 4 (b)). The thinner Al_2O_3 barrier layer generally results in the Sr-richer STO layer due to the oxygen diffusion effect, and this Sr-richer seed layer further enhances Sr incorporation into the main STO layer. The main STO layer for the case of 0.8-nm-thick Al_2O_3 layer

is influenced by both effects and has a very high Sr composition all over the Ti:Sr sub-cycle ratio range. These results clearly indicate the complicated process of STO ALD and the requirement of a thorough understanding of each step of the entire seed layer deposition, seed layer annealing, and main layer deposition process. The Al₂O₃ barrier layer generally has a superior ability to achieve accurate cation composition control to TiO₂.

Figures 5 (a) and (b) show the glancing angle mode X-ray diffraction patterns of STO films with slightly different Sr concentrations in the main STO layers (10–12 nm thick) on the TiO₂ and Al₂O₃ barriers, respectively. The main STO layers were deposited on the crystallized seed STO layers, and all of the STO films showed in situ crystallized perovskite peaks corresponding to the (110) and (200) planes. There are no peaks corresponding to the Ruddlesden-Popper phases, suggesting that the different barrier types do not influence the crystallization of the main STO layer films.

Figures 6 (a) and (b) show the AES depth profiles of 8-nm-thick and 10-nm-thick STO films on the 3-nm-thick TiO₂ and 1-nm-thick Al₂O₃ barrier layers, respectively. The cation compositions of STO films were 48% and 54% for the TiO₂ barrier and Al₂O₃ barrier samples, respectively. The Sr and Ti distribution along the thickness direction was a bit more uniform on the TiO₂ barrier. For the carbon contamination, there is a little more C element in Al₂O₃ barrier sample than TiO₂ barrier sample near the surface. However, when it

comes to the bulk region, C concentration shrinks to below 2% with Al₂O₃ barrier layer which is lower than with TiO₂ barrier layer which indicates the pureness of STO layer. Since Sr easily forms SrCO₃ with C and O for its very low Gibbs free energy,^[17] Sr-richer layer near surface in Al₂O₃ barrier sample caused this large C contamination. The Al hardly diffused to the surface of the STO film. The AES depth profile data of the film after cure annealing at 400°C in air for 30 min which is grown with the identical process with the sample shown in Fig. 6 (b) was appended in the same graph using the straight lines. There are little changes in the distribution of Sr, Ti, Al, and Ru atoms along the direction normal to the substrate surface. However, carbon concentrations in the STO layers are uniformly reduced through the whole film, which may contribute to the improved electrical properties of the sample after the cure annealing. Also, oxygen from air diffused to the STO surface and increased the oxygen concentration slightly. The as-grown ALD STO layer could be oxygen-deficient containing the oxygen vacancies which degrade the electrical performance, perhaps due to the imperfect oxidation or ligand exchange.

Figures 7 (a) and (b) show the surface morphology and the cross-sectional view, respectively, observed by SEM of the 11-nm-thick STO film (deposited by 25 super-cycles) grown on the 1-nm-thick Al₂O₃/Ru substrate. The film shows a very smooth surface and a uniformly small grain size (~20 nm) without any abnormally shaped grains. Also, the inset figure in Figure 7 (d) is

the AFM topographic image of the same sample. The root-mean-squared (rms) roughness of the STO film was 0.6nm, which shows the smooth surface quantitatively. XPS of O1s signal can serve us another feasible indicator for the suppression of excessive SrO deposition and accompanying SrCO₃ formation. Lee et al. showed that the O1s XPS peak is almost exclusively composed of the signal at the binding energy that corresponds to SrCO₃ when no appropriate barrier layer was adopted.^[17] However, when the adverse reaction was appropriately suppressed by the adoption of thin barrier layer (TiO₂ in Ref. 17) the O 1s XPS peak was mainly composed of the signal that corresponds to STO although the peak corresponding to the SrCO₃ was not completely removed due to the formation of that component on the film surface during the exposure of the sample to air atmosphere before the XPS analysis. Figure 7 (c) is XPS of O 1 s of the STO film (Sr ~50%) on the Al₂O₃ barrier. The XPS peak positions were calibrated using the adventitious C 1 s peak position (C–C bonding 284.5 eV).^[25] The peak shape is quite similar to that of the sample on the TiO₂ barrier layer,^[17] and the peak deconvolution showed that there are two components corresponding to SrCO₃ (binding energy of 531.2 eV) and STO (binding energy of 529.2 eV). Sharp and clear STO peak indicates that the formation of SrCO₃ was well suppressed. Figure 7 (d) shows the valence band edge (VBE) structure of the same sample obtained by XPS. The scattering of photoelectrons with the valence band electrons leads to the loss of energy of photoelectrons, by which valence band structure

of the STO films can be inferred. As the upper level of valence band could be mainly composed of O 2p states, monitoring the XPS O 2p can give viable information on the valence band structure. When the Fermi level (E_F) of the film is equilibrated with that of the XPS system, which works as the reference energy level (0 eV), the extrapolation of the tailing edge with the best-linear fitted graph to base line gives the VBE. For the given energy gap of STO, the difference between conduction band edge (CBE) and E_F can be also calculated by a simple subtraction ($CBE - E_F = E_g - (E_F - VBE)$).^[3] The valence band offset between the Fermi level of the Ru substrate and the STO VBE was ~ 1.84 eV. Since the band gap of STO is ~ 3.2 eV^[26], the deposited STO film should be of an n-type property, possibly due to the presence of oxygen vacancies.

The electrical properties of the STO films on the 3-nm-thick TiO_2 and 1-nm-thick Al_2O_3 barrier layers were examined in detail. To accomplish this goal systematically, the STO films with different thicknesses were prepared adopting the identical crystalline seed layers. After depositing the top Pt electrode (80-nm thickness), all of the samples were annealed at 400 °C in air for 30 min to cure the possible damaging effect from the electron beam evaporation process of top Pt. Since the metal-insulator-metal samples in this study have a rather complicated structure, a simple capacitance measurement cannot provide meaningful information on the dielectric constant. Therefore, the t_{ox} data of various samples grown under the different Ti:Sr sub-cycle ratios (or Sr compositions) was plotted as a function of physical thickness (t_{phy}) of

the film as shown in Figs. 8 (a) and (b). From the relationship between t_{ox} and t_{phy} [$t_{\text{ox}} = t_{\text{phy}} \times (3.9/\epsilon_r) + t_{\text{ox}}^i$], where the ϵ_r is the bulk dielectric constant of STO and t_{ox}^i represents all of the possible contributions from the interfaces, the ϵ_r and t_{ox}^i of the different STO films were extracted from the inverse slope and the y-axis intercepts, respectively, of the best linear fitted graphs, and the results are summarized in Figs. 9 (a) and (b).

The data shown in Fig. 9 (a) corresponds well to the general trend of ϵ_r vs. Sr concentration of the STO films^[12-13,17], where the peak dielectric constant was achieved near the stoichiometric composition. A maximum ϵ_r of 173 was achieved from the STO films with a Sr concentration of 51% on the Al_2O_3 barrier layer. It appears that the types of barrier layers do not influence ϵ_r , which must be a reasonable consequence. Considering that the maximum heat-treatment temperature after the main STO layer deposition was only 400 °C, this is a very promising result, indicating the appropriateness of the adopted method. It can be noted that there is a change of slope in Figure 8 (b) for the Sr concentration of 39%, which corresponds to an ϵ_r change from 121 to 33. This is due to the following reason: when the thickness of the main STO layer is very thin, the Sr-deficient composition of the main layer must be compensated by the slightly Sr-rich composition of the seed layer by inter-diffusion and the overall film becomes quite cation stoichiometric. It appears that ϵ_r of these thin layers is ~ 121 , which is a quite reasonable value. As the main layer thickness increased, the composition of the overall layer was

dominated by the Sr-deficient main layer and t_{ox} is also dominated by the non-stoichiometric STO bulk and a smaller ϵ_r was achieved.

The contributions from the t_{ox}^i in both cases are quite detrimental as shown in Fig. 9 (b). As the overall Sr concentration increases, the t_{ox}^i tends to slightly decrease, suggesting the diffusion of Sr into the barrier layers. However, the t_{ox}^i remained at 0.3–0.5 nm and 0.7–1.1 nm for the TiO_2 and Al_2O_3 barriers. Since there could be various contributions to t_{ox}^i such as interfacial contamination and intrinsic dead layer^[27] in addition to the barrier layers, the dielectric constant of the barrier cannot be calculated from these values, even when their thickness can be estimated. However, it is quite obvious that scaling down the t_{ox} value to <0.5 nm is impossible with these barriers, especially Al_2O_3 due to its lower dielectric constant despite a thickness as low as 1 nm.

Figures 10 (a) and (b) show the leakage current density at an applied voltage of 0.8 V vs. t_{ox} plots for the TiO_2 and Al_2O_3 barrier samples, respectively. Due to the contribution from the t_{ox}^i , the minimum achievable t_{ox} values with acceptable leakage current density ($<10^{-7} \text{ A/cm}^2$ @ 0.8 V) were only 0.69 nm and 1.14 nm for TiO_2 and Al_2O_3 barrier samples, respectively, even with such a promising dielectric constant of the STO film. Therefore, another method that can reduce the contribution from the interfacial barrier

layer or the ALD process of the STO layer that does not require adoption of the barrier layer is necessary.

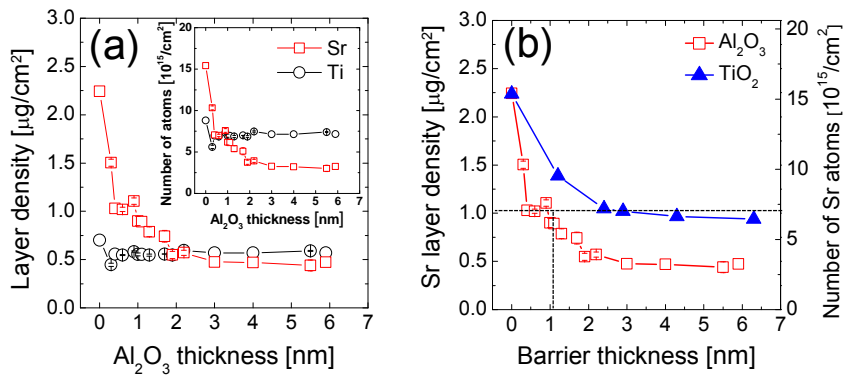


Figure 2.2 (a) Variations in the layer densities (inset numbers of Sr and Ti atoms) of the STO films deposited on Al₂O₃ barriers as a function of Al₂O₃ barrier thickness and (b) comparison between the blocking effects of the TiO₂ and Al₂O₃ barriers on Sr incorporation

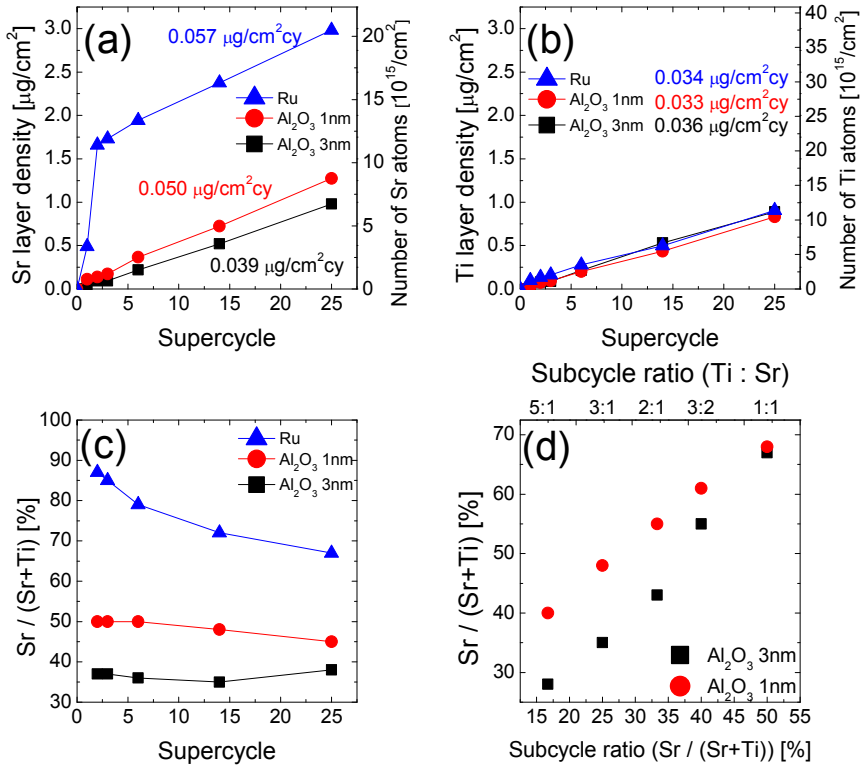


Figure 2.3 Variations in the (a) Sr layer density (number of Sr atoms), (b) Ti layer density (number of Ti atoms), and (c) Sr composition of the STO film as a function of STO super-cycle number on Ru, 1-nm $\text{Al}_2\text{O}_3/\text{Ru}$, and 3-nm $\text{Al}_2\text{O}_3/\text{Ru}$ substrates and (d) the variation of Sr composition as a function of Sr/(Sr+Ti) sub-cycle ratio on 1-nm $\text{Al}_2\text{O}_3/\text{Ru}$ and on 3-nm $\text{Al}_2\text{O}_3/\text{Ru}$

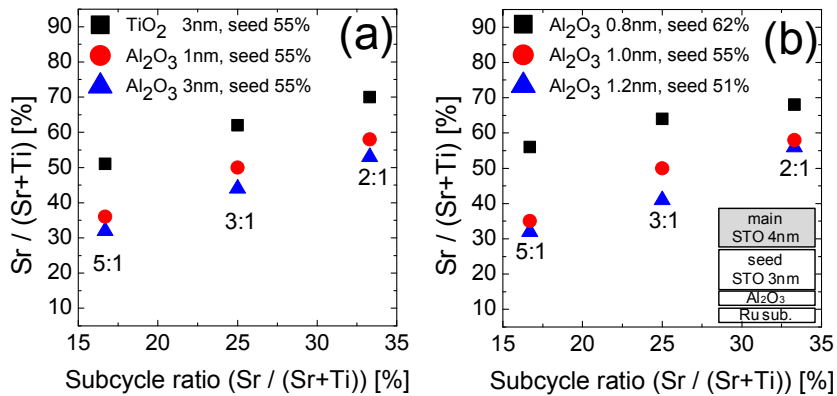


Figure 2.4 Variations of the Sr composition in the main layer STO as a function of Sr/(Sr+Ti) sub-cycle ratio for main STO layer deposition (a) on the seed layer STO with Sr composition of 55% on 3-nm-thick TiO₂/Ru, 1-nm-thick Al₂O₃/Ru, and 3-nm-thick Al₂O₃/Ru and (b) on the seed layer STO with Sr compositions of 62%, 55%, and 51% on 0.8-nm-thick Al₂O₃/Ru, 1-nm-thick Al₂O₃/Ru, and 1.2-nm-thick Al₂O₃/Ru

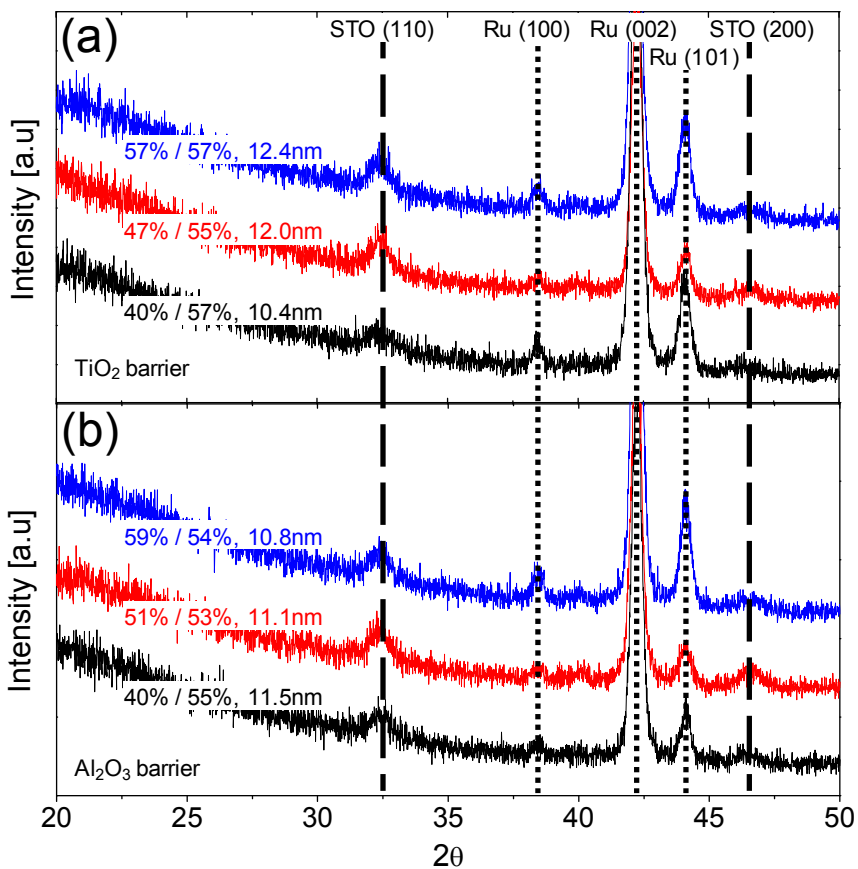


Figure 2.5 Glancing angle mode X-ray diffraction patterns of STO films on the (a) TiO_2 and (b) Al_2O_3 barriers

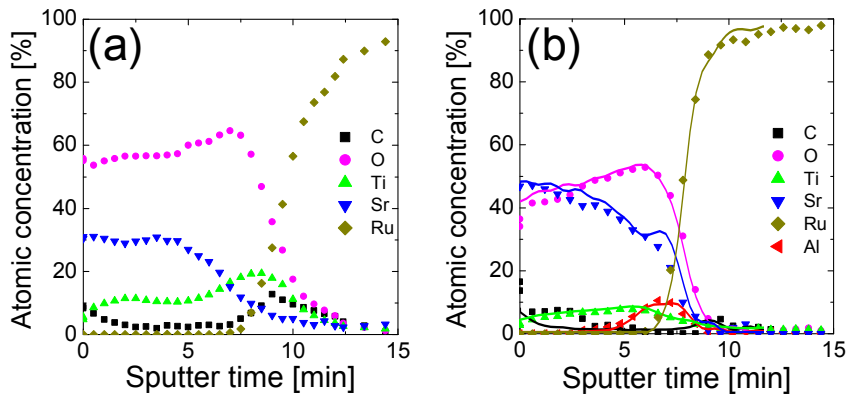


Figure 2.6 The AES depth profiles of (a) 8-nm-thick STO films on the 3-nm-thick TiO_2 barrier and (b) 10-nm-thick STO films on the 1-nm-thick Al_2O_3 barrier

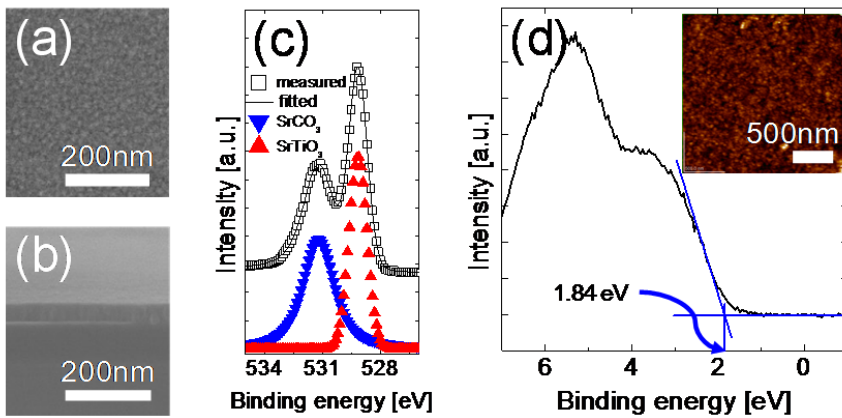


Figure 2.7 Scanning electron microscopy image of (a) the surface and (b) the tilted view cross-section of the 11-nm-thick STO film. The XP spectra of (c) O 1 s and (d) the valence band structure of the 10-nm-thick STO film. Inset figure in (d) shows the AFM topographic image of the 11-nm-thick STO film. The root-mean-squared roughness was only 0.6 nm. All STO films were grown on the 1-nm-thick $\text{Al}_2\text{O}_3/\text{Ru}$.

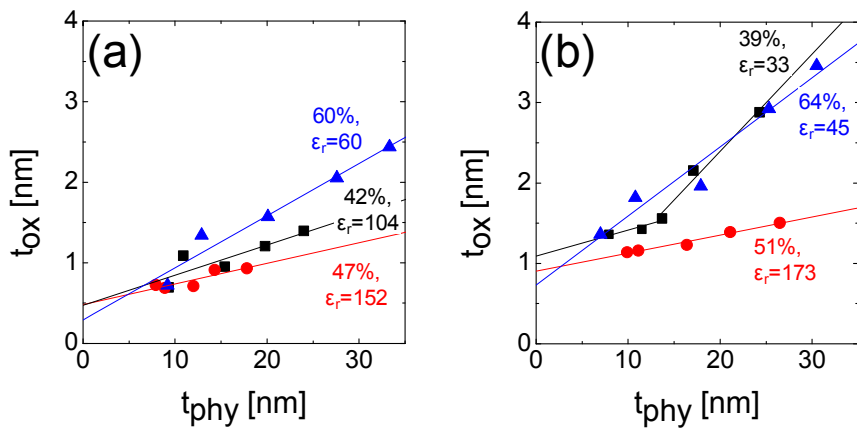


Figure 2.8 Variations of t_{ox} with different Sr composition of the STO main layer with (a) 3-nm-thick TiO_2 barrier layers and (b) 1-nm-thick Al_2O_3 barrier layers

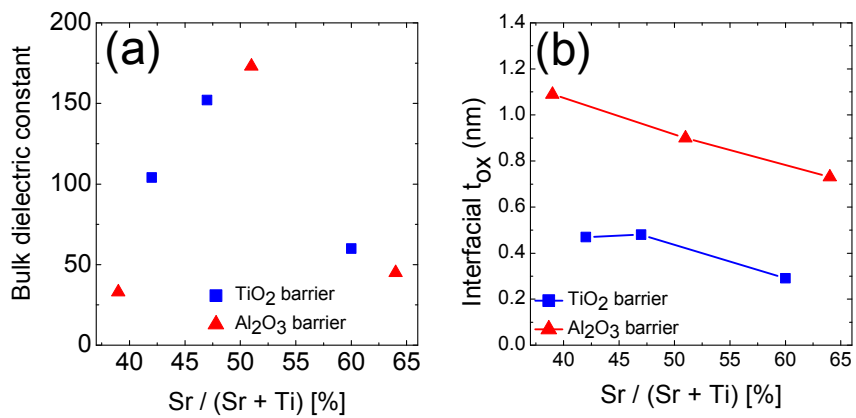


Figure 2.9 Variations of (a) bulk dielectric constant and (b) interfacial t_{ox} extracted from Figure 8 as a function of Sr composition

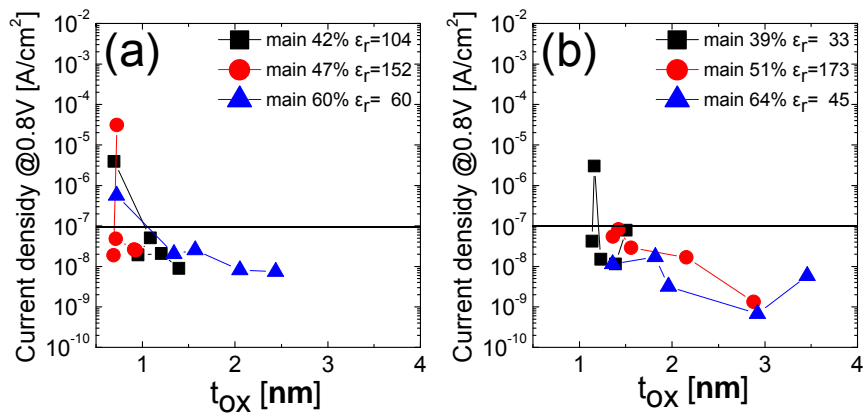


Figure 2.10 The leakage current density (@ 0.8 V) vs. t_{ox} plot of STO films with (a) 3-nm-thick TiO₂ barrier layers and (b) 1-nm-thick Al₂O₃ barrier layers on a Ru substrate

2.4. Summary

Thin STO films were grown on Ru-coated Si wafers by ALD using $\text{Ti}(\text{O-}^i\text{Pr})_2(\text{tmhd})_2/\text{O}_3$ and $\text{Sr}(^i\text{Pr}_3\text{Cp})_2/\text{H}_2\text{O}$ as Ti and Sr precursors/oxygen source at a substrate temperature of 370 °C. According to the previous reports on the initial excessive incorporation of Sr due to the supply of oxygen from the oxidized Ru substrate, the effects of the TiO_2 and Al_2O_3 barrier layers were examined. Ultimately, 3–4 nm-thick TiO_2 and 2–3 nm-thick Al_2O_3 barrier layers were necessary to completely suppress the oxygen diffusion from the underlying Ru layer, suggesting the better diffusion barrier property of Al_2O_3 . The 3-nm-thick TiO_2 and 1-nm-thick Al_2O_3 barrier layers produced almost identical Sr incorporations due to the catalytic effect of the Ti-O surface on the chemical adsorption of the Sr precursor (but with no oxygen effect), and appropriate oxygen permeation through the 1-nm-thick Al_2O_3 barrier layer (but with no catalytic effect). Adoption of the 3-nm-thick crystallized seed STO layer induced the in situ crystallization of the main STO layer. A careful and separate control of the sub-cycle ratio of the Ti:Sr injection was required to achieve the stoichiometric cation composition of the seed and main layer STO. The RTA process for the crystallization of the seed STO layer largely degrades the barrier performance of the TiO_2 layer, while that of Al_2O_3 layer was minimally influenced. Therefore, the Al_2O_3 barrier layer has a superior ability in achieving the accurate cation composition control to TiO_2 . The

stoichiometric in situ crystallized films on the 1-nm-thick Al_2O_3 barrier layer show a dielectric constant as high as 173, quite a promising value. However, the presence of interfacial layers adversely interferes with the scaling down of equivalent oxide thickness. Therefore, another deposition process including different precursors and deposition temperatures must be pursued in the future.

2.5. Bibliography

1. S. K. Kim, S. W. Lee, J. H. Han, B. Lee, S. Han, and C. S. Hwang, *Adv. Funct. Mater.*, 2010, 20, 2989.
2. H. J. Cho, Y. D. Kim, D. S. Park, E. Lee, C. H. Park, J. S. Jang, K. B. Lee, H. W. Kim, Y. J. Ki, I. K. Han, and Y. W. Song, *Solid-State Electron.*, 2007, 51, 1529.
3. S. K. Kim, G. -J. Choi, S. Y. Lee, M. Seo, S. W. Lee, J. H. Han, H. -S. Ahn, S. Han, and Cheol Seong Hwang, *Adv. Mater.*, 2008, 20, 1429.
4. J. H. Han, S. Han, W. Lee, S. W. Lee, S. K. Kim, J. Gatineau, C. Dussarrat, and Cheol Seong Hwang, *Appl. Phys. Lett.*, 2011, 99, 022901.
5. J. H. Han, S. W. Lee, S. K. Kim, S. Han, C. S. Hwang, C. Dussarrat, and J. Gatineau, *Chem. Mater.*, 2010, 22, 5700.
6. S. K. Kim, J. H. Han, G. H. Kim, and Cheol Seong Hwang, *Chem. Mater.*, 2010, 22, 2850.
7. J. H. Han, S. W. Lee, G. -J. Choi, S. Y. Lee, C. S. Hwang, C. Dussarrat, and J. Gatineau, *Chem. Mater.*, 2009, 21, 207.

8. M. Vehkamäki, T. Hatanpää, T. Hänninen, M. Ritala, and M. Leskelä, *Electrochem. Solid-State Lett.*, 1999, 2, 504.
9. O. S. Kwon, S. K. Kim, M. Cho, C. S. Hwang, and J. Jeong, *J. Electrochem. Soc.*, 2005, 152, C229.
10. M. Vehkamäki, T. Hänninen, M. Ritala, M. Leskelä, T. Sajavaara, E. Rauhala, and J. Keinonen, *Chem. Vap. Deposition*, 2001, 7, 75.
11. O. S. Kwon, S. W. Lee, J. H. Han, and C. S. Hwang, *J. Electrochem. Soc.*, 2007, 154, G127.
12. C. S. Hwang, S. O. Park, C. S. Kang, H. -J. Cho, H. -K. Kang, S. T. Ahn, and M. Y. Lee, *Jpn. J. Appl. Phys.* 1995, 34, 5178.
13. C. S. Kang, C. S. Hwang, H. -J. Cho, B. T. Lee, S. O. Park, J. W. Kim, H. Horii, S. I. Lee, Y. B. Koh, and M. Y. Lee, *Jpn. J. Appl. Phys.*, 1996, 35, 4890.
14. M. A. Pawlak, B. Kaczer, M.-S. Kim, M. Popovici, J. Swerts, W.-C. Wang, K. Opsomer, P. Favia, K. Tomida, A. Belmonte, B. Govoreanu, C. Vrancken, C. Demeurisse, H. Bender, V. V. Afanas'ev, I. Debusschere, L. Altimime, and J. A. Kittl, *Appl. Phys. Lett.*, 2011, 98, 182902.
15. S. W. Lee, O. S. Kwon, J. H. Han, and C. S. Hwang, *Appl. Phys. Lett.*, 2008, 92, 222903.

16. S. W. Lee, J. H. Han, and Cheol Seong Hwang, *Electrochem. Solid-State Lett.*, 2009, 12, G69.
17. S. W. Lee, J. H. Han, S. Han, W. Lee, J. H. Jang, M. Seo, S. K. Kim, C. Dussarrat, J. Gatineau, Y. -S. Min, and C. S. Hwang, *Chem. Mater.*, 2011, 23, 2227.
18. S. K. Kim, G. W. Hwang, W. -D. Kim, and C. S. Hwang, *Electrochem. Solid-State Lett.*, 2006, 9, F5.
19. S. W. Lee, J. H. Han, S. K. Kim, S. Han, W. Lee, and C. S. Hwang, *Chem. Mater.*, 2011, 23, 976.
20. S. W. Lee, J. H. Han, O. S. Kwon, and C. S. Hwang, *J. Electrochem. Soc.*, 2008, 155, G253.
21. M. RADECKA and M. REKAS, *J. Phys. Chem. Solids*, 1995, 56, 1031.
22. D. Gopireddy and C. G. Takoudis, *Phys. Rev. B*, 2008, 77, 205304.
23. S.-J. Won, S.Suh, S. W. Lee, G. -J. Choi, C. S. Hwang, and H. J. Kim, *Electrochem. Solid-State Lett.*, 2010, 13, G13.
24. S. K. Kim, G. J. Kim, J. H. Kim, and C. S. Hwang, *Chem. Mater.*, 2008, 20, 3723.

25. NIST. X-ray Photoelectron Spectroscopy Database.
<http://srdata.nist.gov/xps/>.
26. K. Benthema, C. Elsässer, and R. H. French, *J. Appl. Phys.*, 2001, 90, 6156.
27. M. Stengel and N. A. Spaldin, *Nature*, 2006, 443, 679.

3. Countervailing Excess Growth of Sr with Reactive Ti-precursor

3.1. Growth Behavior and Properties of SrTiO₃ Films

3.1.1. Introduction

Dynamic random access memory (DRAM) is one of the most important components in personal computers, servers, and mobile electronic devices. Highly scaling DRAM devices is vital for faster, smaller, and lower-power operation. However, even with a reduced size of the capacitor in DRAM, the capacitance and leakage current should be maintained at a certain level (25fF/cell and 1fA/cell) for fluent operation of the memory. Since the capacitance is determined by the permittivity, thickness of the dielectric, and the overlap area of the two electrodes, a material with a high dielectric constant is necessary for next-generation DRAM. The dielectric material presently being used in mass production is composed of a ZrO₂/Al₂O₃/ZrO₂ stacked layer, where ZrO₂ is used for increasing the dielectric constant, and Al₂O₃ is used for suppressing the leakage current.^[1-3] However, to scale down DRAM to the design rule of <20nm, employing materials with an even higher dielectric constant, such as SrTiO₃ (STO), is necessary.^[1] There have been

many reports on the atomic layer deposition (ALD) of STO considering its potential ability for use in controlling thickness precisely and conformal coverage over extreme three-dimensional structures, and for realizing optimal film properties. However, it is not a trivial task to achieve fluent ALD reaction and optimal electrical performance at the same time from STO using feasible metal electrodes, such as Ru, RuO₂, or even SrRuO₃.^[1, 4] Earlier reports on the ALD of STO from a group at university of Helsinki^[5] have not shown promising electrical properties on such metal electrodes, and technically meaningful reports considering both points have only been made recently mostly by two groups. One is the group at Interuniversity Microelectronics Centre (IMEC) which has reported the use of Sr(^tBu₃Cp)₂ and Ti(OMe)₄ as the Sr and Ti precursors, respectively, at a low growth temperature (T_g) of 250 °C, due to the limited thermal stability of Ti(OMe)₄ at higher T_g.^[6-9] Bu and Me are C₄H₉ and CH₃, respectively. As already noted by the group of the present authors, STO films grown at such low T_g have been accompanied by cracking problems during post-deposition annealing performed to crystallize the amorphous as-deposited films.^[10] The IMEC group reported that the film is crystallized with finer grains without cracking problems when the film composition is slightly Sr-rich (Sr/(Sr+Ti) ~ 62at.%). Therefore, they deposited Sr-rich STO film on a 1-nm-thick TiO₂ buffer layer to achieve stoichiometric STO after crystallization annealing. As a result, a minimum equivalent oxide thickness (t_{ox}) of 0.4 nm was achieved, with a leakage

current density of $\sim 1 \times 10^{-7} \text{ Acm}^{-2}$, which are the best electrical results reported so far for the ALD of STO films.^[8] However, such multi-step processes could suffer from unpredictable variations and issues with high cost due to the complicated sequences of the entire process.

ALD has also been attempted at a high T_g of 370 °C in a series of investigations by the authors' group in order to achieve in-situ crystallization, which precludes the use of simple Ti-alkoxides due to their inappropriate thermal stability at this temperature. Summary of such research history was given in one of the authors' recent publications.^[11] Molecules with 2, 2, 6, 6 - tetramethyl - 3, 5 - heptanedionato (tmhd) ligand or Cyclopentadienyl (Cp)-based ligand are promising precursor materials for achieving sufficient thermal stability of both the Sr and Ti precursors. While the precursors with tmhd ligand are a relatively conventional material for ALD, their reactivity to common oxygen sources, such as H_2O , is limited, making the growth rate very low.^[12] In contrast, the precursors with Cp-based ligand have been recently gaining more interest thanks to their sufficient thermal stability with much higher reactivity toward oxygen sources, making them quite feasible precursors for ALD. The authors have reported on the characteristics of the ALD of STO films using $\text{Sr}(\text{Pr}_3\text{Cp})_2$ and $\text{Ti}(\text{O-iPr})_2(\text{tmhd})_2$, with a growth rate (0.107nm/cycle) about six times higher than that using $\text{Sr}(\text{tmhd})_2$ and $\text{Ti}(\text{O-iPr})_2(\text{tmhd})_2$ (0.017nm/cycle).^[13] In both cases, the as-deposited films were amorphous even with the high T_g of 370 °C, and a two-step process was

required to achieve in-situ crystallized STO films. In the two-step process, about 3-nm-thick STO was first deposited and crystallized by rapid thermal annealing (RTA), which works as a crystalline seed layer for the subsequently grown main STO layer (7 – 10nm). This is an unfavorable aspect of such ALD processes. Another serious problem with the ALD process using $\text{Sr}(\text{iPr}_3\text{Cp})_2$ and $\text{Ti}(\text{O-iPr})_2(\text{tmhd})_2$ precursors is that when the STO film was deposited on Ru or RuO_2 substrate, which are appropriate electrodes for next-generation DRAM capacitors, the Sr incorporation rate during the first several ALD cycles was extremely high, which is also accompanied by the formation of unwanted SrCO_3 phase. This unwanted reaction was understood as chemical vapor deposition (CVD) like behavior of the SrO (SrCO_3) film due to the oxygen supply from the Ru substrate, which had been oxidized in-situ by O_3 , or from the reduced RuO_2 during the deposition process. SrO has a much higher formation energy per molar oxygen compared with RuO_2 (or even TiO_2), so if cleaved Sr atoms are present on the oxidized Ru or RuO_2 surface, they take oxygen atoms and grow the SrO layer, which prevents the self-limited growth behavior of ALD during the Sr precursor pulse step, even without simultaneously supplying an oxygen source. This is further aggravated by the high T_g of 370 °C, where the weak binding between the Sr atoms and modified Cp ligand is easily broken, while the stronger bond between the Sr atoms and tmhd ligand remains almost intact in other ALD processes. In order to alleviate such unwanted CVD-like reaction components,

a 3-nm-thick TiO₂ film^[13] or a 1-nm-thick Al₂O₃ layer^[11] was adopted as the reaction barrier between the STO layer and Ru (or RuO₂) substrate. However, these reaction barriers generally have lower dielectric constants than STO, making that the minimum attainable t_{ox}s with sufficiently low leakage current density (< 1 x 10⁻⁷ Acm⁻² at 0.8 V) were limited to 0.57 and 1.14 nm for the cases with the TiO₂ and Al₂O₃ reaction barriers, respectively, even though the dielectric constants of the STO layer were as high as 146 and 173, respectively.^[11, 13]

Therefore, it is necessary to avoid the adoption of such reaction barriers to further decrease the t_{ox} values, which is necessary for the DRAMs with sub-20 nm design rule. Given the fact that the Cp-based Sr precursor appears to be the only viable option at the moment, and Ti has a much wider variability in its precursor chemistry, a new Ti precursor, Cp*Ti(OMe)₃ (Cp*=C₅(CH₃)₅), is adopted in this work. This precursor is expected to show a reactivity toward oxygen similar to that of Sr(ⁱPr³Cp)₂. It is expected that the weak binding energy between the Cp* and Ti atom, and non-chelated nature of Ti-OMe bonding, result in easier cracking between the Ti and ligands in this Ti precursor molecule, such that there would also be a CVD-like incorporation of Ti during the early stage of ALD on Ru and RuO₂ substrate. The results section below reveals that this was indeed the case, and that the material can actually be used to make the cation composition ratio of the STO film close to the desired ratio of 1:1 from the beginning of the ALD, even without adopting

the reaction barrier layer. As a result, the saturated growth rate of STO film was 0.123 nm/cy, and the best electrical performance with a t_{ox} value of 0.43nm and acceptable leakage current density of $\sim 8 \times 10^{-8} \text{ A/cm}^2$ at 0.8 V were achieved.

3.1.2. Experimental

TiO₂ and STO films were deposited in a traveling wave-type ALD reactor (CN-1 Co, Plus-100) for a 4-inch-diameter single wafer. Sr(ⁱPr₃Cp)₂ and Ti(Me₅Cp)(OMe)₃ (synthesized by Air Liquide) were employed as the Sr and Ti precursors, respectively. Another Ti precursor, Ti(O-ⁱPr)₂(tmhd)₂ (Air Liquide), was also used as a reference to confirm the large reactivity of the Cp-based Ti precursor. Ti(O-ⁱPr)₂(tmhd)₂ and Cp*Ti(OMe)₃ are denoted henceforth as Ti-A and Ti-B, respectively, and their schematic structures are shown in Fig. 1. The canisters of the Ti-A, Ti-B, and Sr precursor were heated to 130, 80, and 90 °C to maintain the appropriate vapor pressures of the precursors. Ar carrier gas was bubbled through the canisters to deliver the Sr and Ti precursors to the reaction chamber at a flow rate of 200 sccm, and the working pressure of the ALD reactor fluctuated near 0.7 Torr. H₂O, which was used as the oxygen source for Sr precursor, was cooled down to 3 °C to control its high vapor pressure, and O₃ at a concentration of 250 g/m³ was used as the oxygen source for the TiO₂ sub-layers.^[13]

The ALD sub-cycle process for SrO and TiO₂ with Ti-A consisted of precursor injection (3s), followed by Ar purge (5s), oxygen source injection (2s), and Ar purge (5s), which was confirmed to be consistent with the saturated ALD conditions.^[11, 13] It was found that the same time schedule is appropriate for the well-saturated ALD of TiO₂ films using the Ti-B

precursor. The ALD super-cycles for STO deposition consist of ALD sub-cycles of SrO and TiO₂ layers with different cycle ratios to vary the cation composition. The T_g was set at 370°C, and Ru(30 nm)/Ta₂O₅(8 nm)/SiO₂(100 nm)/Si wafers or RuO₂(40 nm)/SiO₂(100 nm)/Si wafers were used as substrates. Since the single STO layer growth at this T_g still did not induce in-situ crystallization, the aforementioned two-step process was also employed in this work. Crystallization-annealing of the thin seed STO layer was performed in an RTA system at 650 °C for 2 minutes in an N₂ atmosphere (purity >99.99%).

The layer density and cation composition of STO films were confirmed by X-ray fluorescent spectroscopy (XRF, Themoscientific, ARL Quant'X). The physical thickness of the STO films on Ru substrate was measured using an ellipsometer, and that of the STO films on RuO₂ substrate was calculated by correlating the layer density and physical thickness of STO on Ru substrate. The impurity concentration in the films, including carbon, and the depth profile were examined by Auger electron spectroscopy (AES, Perkin-Elmer, PHI 660). The chemical binding states of the films were determined by X-ray photoelectron spectroscopy (XPS, ThermoVG, SIGMA PROBE). The crystal structure of the film was investigated by glancing angle mode X-ray diffraction using a Cu K α X-ray source (GAXRD, PANalytical, X'Pert Pro). The incidence angle, scan step size, and time per step during the GAXRD measurement were 2°, 0.02°, and 1 sec, respectively. The planar-structured

metal-insulator-metal capacitors were fabricated by depositing an 80-nm-thick top Pt electrode by e-beam evaporator through a shadow mask (with a 0.3-mm hole diameter). Cure-annealing was performed after deposition of the top Pt electrode at 400 °C in air for 30 min to cure the radiation damage during the electron beam evaporation. The electrical properties, including the capacitance and leakage current, were measured using an HP4194A impedance analyzer at 10 kHz and an HP4140 picoammeter, respectively.

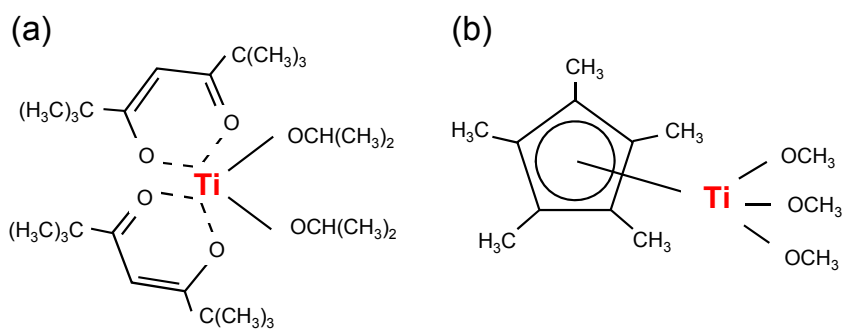


Figure 3.1 The schematic chemical structures of (a) Ti-A precursor and (b) Ti-B precursor.

3.1.3. Results and Discussion

First, the possibility was ascertained of whether the ALD-specific saturation behavior of TiO₂ could be achieved at 370°C with Ti-B precursor. ALD cycling was repeated 50 times on an Ru substrate, with each cycle consisting of precursor injection, precursor purge by Ar gas, O₃ injection, and O₃ purge by Ar gas. Figure 2a shows the variation of Ti layer density as functions of Ti-B precursor injection time and O₃ injection time. As the injection time of Ti-B precursor increases, the deposition amount of Ti element increases and is saturated with injection times over 3 sec. With different O₃ injection times, there was almost no variation over 1 sec. Figure 2b shows the results for the same experiment with increasing the two purge times, and there was almost no variation in the growth of Ti element when the purge time was over 1 sec. All deposited amounts of Ti after saturation injection and purge time in each step were almost identical to $\sim 1.2 \mu\text{g}/\text{cm}^2$, suggesting that the ALD behavior of TiO₂ with Ti-B precursor and O₃ was achieved appropriately at 370°C. Therefore, the durations of each step of the TiO₂ ALD sequence in all subsequent experiments were 3 sec, 5 sec, 2 sec, and 5 sec, for the Ti precursor injection, purge, O₃ injection, and purge times, respectively.

Figures 3a and 3b show the variation of the thickness of the films measured by ellipsometry, and the layer density of Ti measured by XRF as a function of deposition cycles, respectively. The same variations of TiO₂ films

deposited with Ti-A precursor in identical process conditions were also included for the comparison. The well-saturated ALD behavior of TiO₂ films with Ti-A precursor and O₃ was confirmed elsewhere.^[14] Two parameters could be extracted by the best-linear-fits of the graphs: the steady-state growth rate from the slope, and excessive growth of the film on the substrate surface from the y-axis intercept, which represents the reaction of the substrate and the precursor. The steady-state deposition rates of TiO₂ film with Ti-B precursor were 0.061 nm/cycle (17 ng/cm²cycle), whereas those with Ti-A precursor were 0.043 nm/cycle (12 ng/cm²cycle). This suggests that the ALD rate of TiO₂ film using Ti-B precursor is higher by ~1.4 times compared with Ti-A precursor. In addition, the Y-intercepts (Yⁱ) of both cases were positive, meaning that the Ru substrate enhances the initial growth of TiO₂ film. This can be understood from the former knowledge of the in-situ oxidation of Ru electrode and reduction of the oxidized layer during the Ti precursor injection.^[14] In Figs. 3a and b, the Yⁱ of the Ti-B precursor case was much larger than that of the Ti-A precursor case, which is ascribed to the higher reactivity of the Ti-B precursor. As mentioned in introduction section, tmhd ligand has stronger binding energy with metal ions than a Cp-based ligand does. Moreover, as the methyl group is substituted for the hydrogen in the Cp ring, the binding energy between the Cp ring and metal ion becomes even smaller.^[15] The Ti – O bonding involved in the methoxy ligand must be weaker than the chelated Ti – O bond in the tmhd ligand. Therefore, the

possibility of cleaving Ti atoms from the Ti-B precursor on the oxidized Ru surface must be higher than that associated with the Ti-A, making the initial CVD-like growth enhanced. This itself is not a merit of the Ti-B molecule as the Ti precursor for TiO₂ ALD. However, the situation becomes different when it is combined with the ALD cycles of SrO to deposit the STO films with the stoichiometric cation composition ratio, as shown below.

Figure 4a shows the variation in the STO film thickness as a function of ALD super-cycles, where 1 super-cycle consists of 4 TiO₂ sub-cycles (using Ti-B precursor) and 1 SrO sub-cycle. The growth always begins with the TiO₂ sub-cycles. When STO was deposited directly on Ru substrate (indicated by red squares in the figure), the ALD process showed a faster growth rate in earlier cycles than latter cycles. Only 1 super-cycle (5 sub-cycles) deposits a film with a thickness of ~ 3.5 nm, which corresponds to almost ten layers of crystalline STO (although the as-grown film is amorphous). The data corresponding to the right Y-axis of Fig. 4a shows the variation of the derivative of the figure, which corresponds to the thickness growth rate (per super-cycle). The decaying growth rate with the increasing number of super-cycles is clearly shown. In contrast, when the same ALD process was performed on the Ru substrate coated with a 3-nm-thick TiO₂ reaction barrier layer (indicated by black circles in the figure), stable low growth rate was achieved from the first super-cycle. The thickness of the TiO₂ reaction barrier was excluded in the data. The steady-state growth rate of the STO film per

sub-cycle was as high as 0.123 nm/cycle on Ru substrate, which is higher than that reported previously.^[13] For further understanding of this phenomenon, the variations of the layer densities of Sr and Ti were measured for two different substrates, as shown in Fig. 4b. It can be clearly understood that the initially excessive deposition of the SrO layer caused faster initial overgrowth of the STO film, while the initial growth enhancement of Ti element is almost negligible on non-passivated Ru substrate. The linearity in incorporation behavior of Sr could be recovered by covering the Ru substrate with TiO₂ barrier film. The seemingly slight initial retardation in the incorporation of Ti component on the TiO₂-passivated Ru substrate could be due to experimental error in the Ti layer density estimation. This result corresponds well with previous reports on STO deposition using the Sr(ⁱPr₃Cp)₂ and Ti-A precursor.^[11, 13]

However, there were critical differences in the variation of the cation composition ratio (Sr/(Sr + Ti)) of the STO films as a function of the number of super-cycles between the two cases, as shown in Fig. 5. Figure 5a comparatively shows the variations of the Sr-layer density for the STO films grown with either Ti-A (indicated by blue triangles, taken from Ref. 13), or Ti-B (red squares) as a function of ALD super-cycles. There are two notable findings from this figure. First, the initial overgrowth of the Sr component was relatively retarded for the Ti-B case compared with the other case, for up to about three super-cycles. Second, the saturated deposition rate of the Sr

component estimated from the slope of the best-linear-fitted graphs after the super-cycle number of about three was increased by about a factor of 1.6 for the case of Ti-B compared with the other. Such discrepancy in the Sr incorporation of the ALD processes using different Ti precursors resulted in different variations in the cation composition ratio with the increasing super-cycle number, as shown in Fig. 5b. While the Sr/Ti ratio of the STO film was as high as ~ 4 at the initial growth stage and decreased toward the stoichiometric composition with Ti-A precursor, the STO film deposited with the Ti-B precursor process showed a maximum cation ratio of < 2 , even at early super-cycles, and a smaller change in the ratio with the increasing super-cycle number was observed. Here, the TiO₂:SrO sub-cycle ratios of STO deposition with Ti-A and Ti-B were 3:1 and 4:1, respectively, which resulted in almost stoichiometric STO if there was no initial Sr incorporation (on TiO₂-passivated Ru substrate). Such a decreased excessive Sr concentration and small variation in the cation ratio with thickness (number of super-cycle) implies the possible deposition of high-quality STO films on Ru and RuO₂ substrates without intervening reaction barrier layers. The possible reasons for the variations in the incorporation behaviors of Sr and Ti components into the STO film depending on the types of Ti precursor during the given ALD conditions are schematically explained in Fig. 6.

Figure 6 schematically shows the reaction flow of the STO ALD process with Sr(ⁱPr₃Cp)₂ as the Sr precursor, and Ti-A (left hand panel) or Ti-B (right

hand panel) precursors as the Ti precursor. This figure shows the possible mechanism of STO deposition at early stage: O₃ cycle, Ti precursor cycle, O₃ cycle, Sr precursor cycle. First, as in Fig. 6a, when the Ru substrate is exposed to O₃, the surface of Ru metal is oxidized to form a thin (1 – 2 nm) RuO₂ layer by the strong oxidizing power of O₃.^[1] Additionally, as it is described in Fig. 6b, when the Ti precursors are injected onto the substrate surface, they chemically react with the oxidized Ru surface, and a part of the Ti precursor molecules is chemically adsorbed. The Gibbs free energy of the formation of TiO₂ (-833.972 kJ/mol at 600K) is lower than that of RuO₂ (-201.190 kJ/mol at 600K), which means that Ti can reduce the surface RuO₂ to RuO_x (x < 2) or even Ru, such that the oxygen can be evolved from previously oxidized Ru substrate to react with the incoming Ti precursors to form a TiO₂ layer, even before the subsequent oxygen source was injected.^[13] The Ti precursor's ability to reduce the substrate depends on the type of ligands linked to the Ti ions. As mentioned previously, the Ti-B precursor has weaker binding between the Ti atoms and Cp* and OMe ligands compared with the chelated Ti – O bonding in the Ti-A precursor. Therefore, when they are pulsed onto the oxidized Ru surface, Ti-B precursor has a much higher chance to take oxygen from the substrate. In contrast, the Ti-A precursor has a lower chance, since at least some part of the Ti – O bonding in the tmhd ligand part could remain, making the Ti atoms in Ti-A precursors have low probability to take oxygen from the substrate. This was confirmed by Fig. 3, where the Ti-B

precursor has a higher Y^i value and higher saturated growth rate, suggesting a lower steric hindrance effect due to the easier elimination of the bulky ligands during the Ti precursor pulse step. Therefore, after the Ti-injection cycle was completed, more oxygen ions remained in the oxidized Ru substrate for the Ti-A precursor case than in the Ti-B precursor case. In addition, a higher coverage of Ti-O layer is expected on the surface after the Ti-B precursor injection step due to its higher growth rate. When O_3 gas was subsequently injected as shown in Fig. 6c, the remaining ligands are removed and a desirable solid TiO_2 layer is formed. Naturally, the difference of the coverage of Ru (or RuO_2) substrate with TiO_2 layer in two cases results in the higher coverage of TiO_2 in Ti-B precursor case. Finally, as Fig. 6d, the Sr precursors are injected onto these substrates with different TiO_2 and RuO_2 coverage. Since the Gibbs free energy of the formation of SrO is lower than those of TiO_2 or RuO_2 (per molar oxygen), the incoming Sr precursor molecules could reduce both the TiO_2 or RuO_2 layers, but kinetic limitation may mostly result in the reduction of RuO_2 , and CVD-like growth of the SrO layer is obtained at this stage. Greater consumption of oxygen in the RuO_2 layer by the growing TiO_2 layer for the case of the Ti-B precursor during the previous TiO_2 ALD step corresponds to a lower amount of oxygen available for the CVD-like growth of the SrO layer at this stage. In addition, the diffusion of the oxygen ions is more difficult when the coverage of TiO_2 layer on Ru (or RuO_2) is higher. Therefore, the initially excessive incorporation of Sr component in the

STO ALD was retarded with the Ti-B precursor, and better cation stoichiometry was achieved from the early stage of the ALD STO, as shown in Fig. 5b. The higher saturated growth rate of SrO at the later stage of the ALD, mentioned in Fig. 5a, could be understood from the higher growth rate of SrO on TiO₂ compared to that on SrO itself.^[13] Since the surface coverage of the TiO₂ layer is higher on the SrO layer using Ti-B precursor, a higher chance of SrO growth was achieved when the STO ALD was attempted using the Ti-B precursor. Although TiO₂ layer and SrO layer are deposited in turn, the Sr ion and Ti ion easily diffuse to each other layer during the process and consequently form STO film instead of being remained separately layer by layer.

It has to be noted that, in this strategy, Ti-incorporation in an early stage of STO ALD, as well as Sr- incorporation, is enhanced by the CVD-like behavior in order to decrease the Sr-excess composition for the very thin STO film. However, this may not be the optimum solution for achieving the best electrical properties, since the CVD-like reaction can invoke several unwanted side effects, such as impurity incorporation, inappropriate step coverage, and imprecise thickness and composition control. Nevertheless, as shown below, this strategy resulted in the best electrical performance so far from the ALD STO processes at high T_g performed in the authors' group.

The cation composition control was clearly well performed, as shown in Fig. 7, even with the involvement of such CVD-like components. Figure 7 shows the variations in the cation composition ($\text{Sr}/(\text{Sr}+\text{Ti})$, in at %) on various substrate and super-cycles. In general, thinner films are richer in Sr than thicker films on Ru substrate, due to the oxygen supply effect. The Sr-incorporation is still higher than the Ti incorporation, even with the CVD-like effects in both Sr and Ti injections steps. The TiO_2 reaction barrier also works as an effective suppressor for the CVD-like reactions, as can be understood from the fact that STO films on Ru substrate are still slightly richer in Sr than the films deposited on TiO_2 -covered Ru substrate. In contrast, the Sr composition ratio of the STO films on the Pt substrate was the lowest among all the different types of samples, because no oxygen effect can be expected from the Pt substrate.^[13] It is interesting that the Sr-incorporation into the STO film on RuO_2 is even lower than that on Ru substrate when two super-cycles of deposition are performed, while it was expected that the higher oxygen content in the RuO_2 layer would have further enhanced the CVD-like deposition of SrO. This can be understood from the ALD sequence of STO deposition, where the TiO_2 layer is first deposited on the surface of the substrate. The abundant oxygen atoms present in the RuO_2 substrate further enhanced the TiO_2 deposition compared with the in-situ oxidized Ru substrate, which retarded the oxygen diffusion from the substrate to the surface of the already grown TiO_2 layer, where the CVD-like SrO deposition occurs during

the subsequent Sr precursor pulse step.^[13] Therefore, the thicker thickness of the first deposited TiO₂ on RuO₂ retarded the CVD-like reaction of SrO growth, which could be confirmed from the slightly higher layer density of Ti on RuO₂ compared with that on Ru substrate after the 2 STO ALD cycles (0.70 vs. 0.52 μg/cm²). The figure also shows the variation of cation composition of the main layer of STO deposited on the crystallized 3-nm-thick STO seed layer. Due to the barrier effect of the seed STO layer against oxygen diffusion, the Sr-composition is also lower compared with the STO film directly grown on Ru substrate, which is consistent with a previous report.^[11] According to the different cation composition ratios obtained on different substrates, appropriate sub-cycle ratios were determined, as indicated on the x-axis of the figure for the different process steps on Ru and RuO₂ substrates. Next, the chemical, structural, and electrical properties of the STO films grown under the optimized conditions for the seed and main layer growth on either Ru or RuO₂ substrates are reported.

The chemical natures of the STO films grown on Ru substrate with or without the 4-nm-thick TiO₂ reaction barrier are examined. Figures 8a and b show the XP spectra of C 1s and O 1s of the STO films grown directly on Ru substrate using a TiO₂:SrO sub-cycle ratio of 3:1. For this sample, 12 super-cycles were performed. The film was grown to an 11 nm-thickness, and the Sr composition was 52%. The black solid points are the measured data, and the open dotted symbols show the deconvoluted data assuming the presence of

SrCO₃ (288.1 eV) and C-C (284.5 eV). The C-C binding energy was used as a reference for the energy calibration. Similar deconvolution of the O 1s spectra was also performed, and two components corresponding to SrCO₃ (531.2 eV) and SrTiO₃ (529.2 eV) can be seen in Fig. 8b. The peak intensity of SrCO₃ in Fig. 8a is quite low, and a SrTiO₃ peak can be clearly separated

with sharp shape and a small full-width at half maximum from the SrCO₃ in Fig. 8b. Such a peak shape coincides well with the previous reports, where the SrCO₃ was mainly formed by air-exposure of the sample before the XPS measurement, not by the adverse ALD reaction caused by the excessive Sr incorporation.^[13] This was further confirmed by Figs. 8d and e, where the XPS results of the same STO films deposited on TiO₂ passivated Ru substrate are shown. 17 super-cycle depositions with a TiO₂:SrO sub-cycle ratio of 2:1 were performed to make the overall sub-cycle number almost equal to the other case (48 vs. 51 sub-cycles). The thickness of TiO₂ and STO layers were 4 nm and 6 nm, respectively, and the Sr composition of the STO layer was also 52%. As mentioned above and reported elsewhere,^[11,13] the adoption of such a TiO₂ layer completely suppresses the adverse CVD-like Sr-incorporation, and the STO film must have the optimal chemical and electrical properties. The C 1s and O 1s

spectra of this sample are almost identical to the other case, suggesting that the chemical nature of the STO film without the TiO₂ reaction barrier is quite

close to the optimum one, even though there was clear involvement of CVD-like components at the early stage of the film growth. However, defect structures such as oxygen vacancies appear to be influenced by the involvement of such CVD-like reaction. Figures 8c and 8f show the valence band edge structure of STO film on Ru and on TiO₂-passivated Ru substrates obtained by XPS, respectively. The offsets between the Fermi level of the Ru metal and the valence band edges of the STO films were 2.35 eV and 2.18 eV, suggesting that the conduction band offsets, which are the most critical parameters for leakage current suppression, are 0.85 eV and 1.02 eV, respectively, assuming a band gap of 3.2 eV. The details to infer the band structure from the XPS valence band spectra are described elsewhere.^[11] Both band structures suggested that the STO layer is n-type, and the majority carrier in the STO layer must be electrons when the bias is applied. The main reason for this could be the presence of oxygen vacancies in the film, and the presence of TiO₂ reaction barrier layer appears to be beneficial for inducing a higher electron barrier, perhaps due to the more ALD-like deposition reaction of the STO layer from the first cycles, even though the C 1s and O 1s XP spectra did not clearly reveal such discrepancy.

Figures 9a and b are the AES depth profiles of STO (Sr 53%) / Ru and STO (Sr 52%) / TiO₂ / Ru samples, respectively, where the STO layer was deposited via the two-step process described above. Since there were no appropriate standards for AES spectrum calibration, the atomic concentrations

must be considered only as relative numbers. The thicknesses of the films analyzed in Fig. 9 were both 9 nm. Since the Sr composition of the main layer the sample in Fig. 9b is lower than that of the sample in Fig. 9a, and the Sr atoms are partially diffused into the adjacent TiO₂ layer, the overall Sr composition in Fig. 9b is uniformly lower than in Fig. 9a. The figures show that the carbon impurity levels are generally quite low in the bulk of the STO films, confirming that the SrCO₃ component shown in XPS originated from the surface of the film. While the cation concentrations are generally uniform along the thickness direction in Fig. 9a, there was clearly high concentration of Ti at the interface in Fig. 9b, suggesting incomplete intermixing of the TiO₂ and STO layers during the ALD and the crystallization annealing. This coincides with the presence of interfacial t_{ox} component in the electrical property estimation, as shown below.

Figure 10 shows the GAXRD patterns of the two-step-processed 21-nm-thick STO layers grown on Ru and RuO₂ substrates. For the reference, GAXRD of the Ru and RuO₂ layers are also included in the same figure. Clear peaks near two-theta values of 32.5°, 40.0°, and 46.5° prove the in-situ crystallization of the STO layer with the help of the crystallized seed layer (3-nm thick). The STO film with the same composition and thickness without the seed layer did not show such diffraction peaks in GAXRD (data not shown). It can also be observed that clear Ru peaks are present with the RuO₂ peaks for the case of the RuO₂ substrate after the STO deposition, corroborating the

suggested RuO₂ reduction model. Ru substrate hardly shows any distinct RuO₂ peak, even after the STO deposition.

The electrical properties of Pt(top electrode)/STO(dielectric)/Ru(bottom electrode) capacitors were examined. A capacitor device can have many factors influencing the interfacial component of t_{ox} (t_{ox}^i), such as intrinsic dead layer effect^[17] and low interfacial dielectric layer formation, which can adversely affect the total capacitance density. Because of this, examining a single capacitor is not appropriate to accurately estimate the dielectric constant of the material. Therefore, many samples with different physical thicknesses (t_{phy}) were prepared to obtain the bulk dielectric constant (ϵ_r) of the material. The variation in the t_{ox} value, derived from the measured capacitance and capacitor area of the sample, are shown in Fig. 11a as a function of t_{phy} of the STO films for the two different sets of STO samples: STO films directly grown on Ru substrate using Ti-B precursor, and other STO films grown on 3-nm-thick TiO₂ passivated Ru substrate using Ti-A precursor (data taken from Ref. [13]). In both cases, the 3-nm-thick seed layer was adopted, and the TiO₂:SrO sub-cycle ratios for the Ti-A and Ti-B precursors were 3:1 and 6:1. By the best-linear-fitting of the data, ϵ_r of the STO film and t_{ox}^i were extracted from $t_{\text{ox}} = t_{\text{phy}} \times (3.9 / \epsilon_r) + t_{\text{ox}}^i$. The ϵ_r values of the STO films with Ti-A and Ti-B precursors were 146 and 111, respectively, revealing the adverse influence of the CVD-like reactions of Sr and Ti incorporation for the Ti-B case. The CVD-like reaction was almost

completely suppressed for the Ti-A case, because the TiO₂ reaction barrier was adopted. However, the t_{ox} values using the Ti-B precursor are generally smaller than the other case, even with the smaller ϵ_r , which is ascribed to the absence of a discrete reaction barrier. The t_{ox}^i value of the Ti-B case is smaller than that of the Ti-A case by ~ 0.32 nm, which is a significant number considering the target t_{ox} value of $\ll 0.5$ nm. Thanks to such improvement, the minimum t_{ox} value with stably low leakage current density ($< 10^{-7}$ Acm⁻² @ 0.8V) could be decreased to 0.46 nm (t_{phy} was 12 nm), as shown in Fig. 11b, while the minimum t_{ox} in the other case remained at 0.57 nm.^[13] The t_{ox}^i values estimated from the y-axis intercepts in Fig. 11a are vulnerable to error due to the general ellipsometric inaccuracy of the STO film thickness in this thickness range. It appears that the thickness is slightly overestimated from the t_{ox}^i value (~ 0.05 nm) of the Ti-B case, which is too small to be real.

Even further enhancement of the electrical performance of the STO film could be achieved when the film was deposited on RuO₂ substrate, as shown in Fig. 12. For this case, the TiO₂:SrO sub-cycle ratios of 5:1 and 6:1 were adopted for the seed STO and main STO layers, respectively, and the film was well crystallized in-situ (GAXRD data not shown). Figure 12a shows the variations of t_{ox} and dielectric constant versus applied voltage of STO films on Ru and RuO₂ substrates, which were derived from the capacitance – voltage measurements. The data of the Pt/STO(11.8nm)/Ru sample showed a dielectric constant of 101 and t_{ox} of 0.46 nm, which correspond to the best

data of Fig. 11b. The Pt/STO(14.2nm)/RuO₂ capacitor showed a dielectric constant of 128 and t_{ox} of 0.43 nm. The current density – voltage (J – V) plots of the same samples are shown in Fig. 12b. The Pt/STO(14.2nm)/RuO₂ sample showed better J – V performance, even with the smaller t_{ox} value (0.43 vs. 0.46 nm). The low J level was maintained up to ~1.2 V, whereas the other sample showed a J level higher by ~2 orders of magnitude. This is primarily due to the thicker t_{phy} of the STO film on RuO₂, but the higher work function of RuO₂ (~ 5.2 eV) compared with Ru (~ 4.6 eV) may also contribute to the lower J level.^[18-20] Therefore, eliminating the TiO₂ reaction barrier by adopting the new Ti precursor largely contributes to the improvement of the dielectric performance of the ALD STO films.

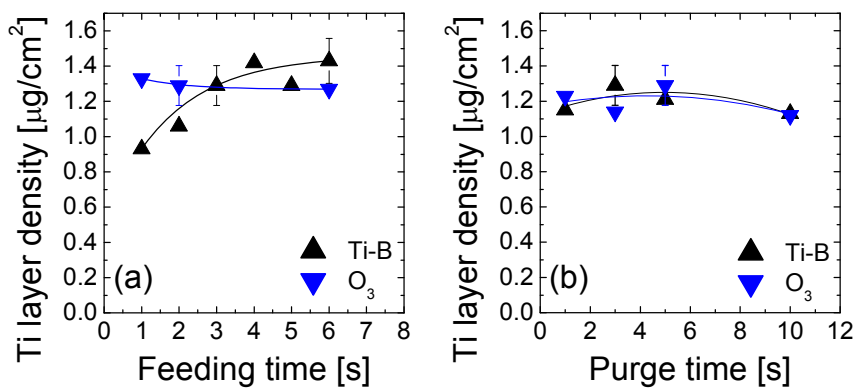


Figure 3.2 Variations of Ti layer densities of TiO_2 films as a function of (a) feeding times and (b) purge times of Ti-B precursor and ozone.

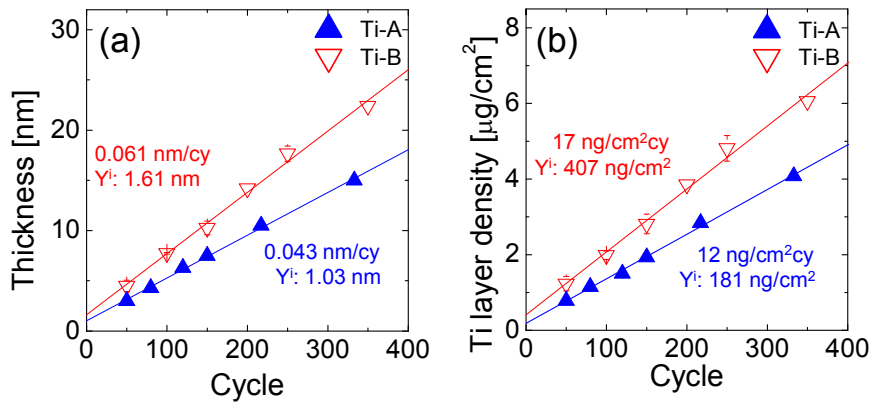


Figure 3.3 The comparison of (a) thickness and (b) Ti layer densities of TiO₂ films as a function of deposition cycles deposited by Ti-A precursor and Ti-B precursor.

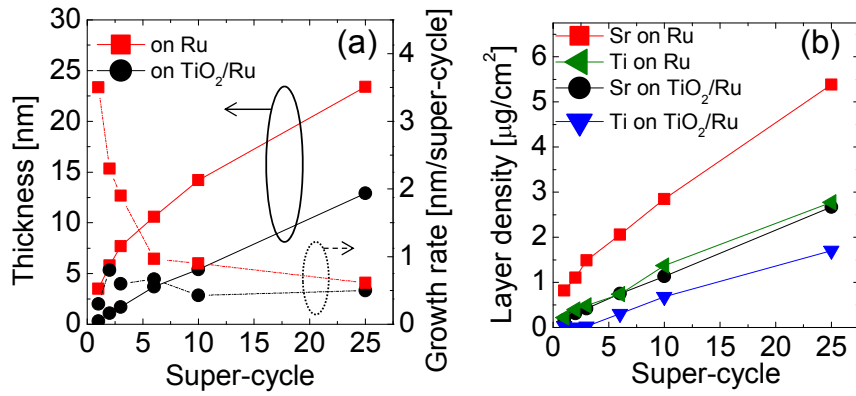


Figure 3.4 (a) Variations of film thicknesses and growth rates of STO films and (b) variations of layer densities of Sr and Ti in STO films on Ru substrate and on TiO₂ coated Ru substrate as a function of STO super-cycles (sub-cycle ratio TiO₂:SrO = 4:1).

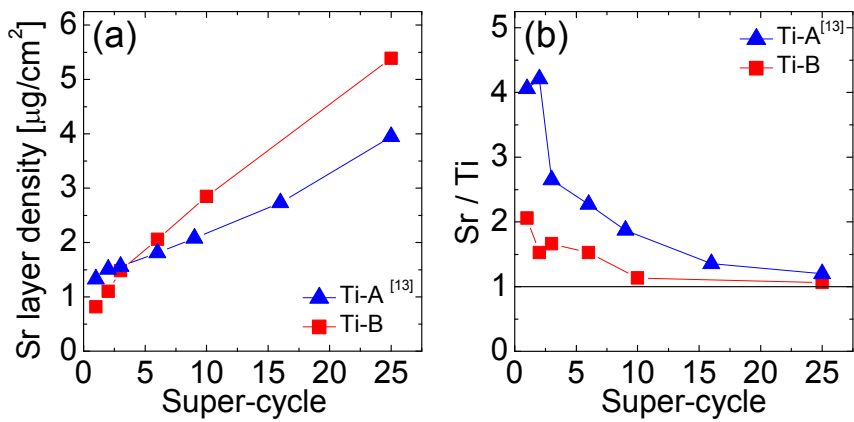


Figure 3.5 (a) Comparison of variations of Sr layer densities and (b) cation ratio (Sr / Ti) of STO films as a function of super-cycles deposited with Ti-A precursors (sub-cycle ratio $\text{TiO}_2:\text{SrO} = 4:1$) and with Ti-B precursors (sub-cycle ratio $\text{TiO}_2:\text{SrO} = 3:1$) Data for Ti-A precursor case was reproduced from Ref.13.

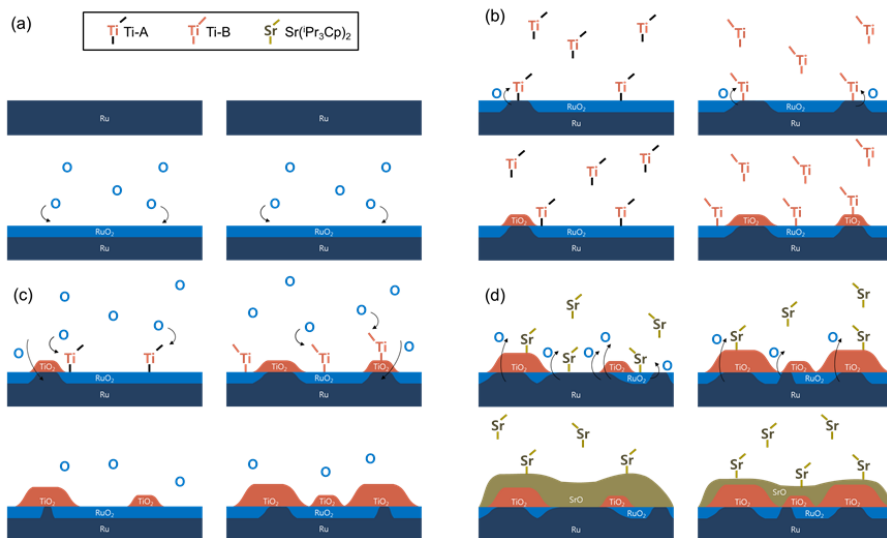


Figure 3.6 The schematic diagrams of the reaction flow of the STO ALD process with $\text{Sr}(\text{Pr}_3\text{Cp})_2$ as Sr precursor and Ti-A (left hand panel) or Ti-B (right hand panel) precursors as Ti precursor: (a) O_3 injection step, (b) Ti precursor injection step, (c) O_3 injection step and (d) Sr precursor injection step. At this stage, TiO_2 and SrO already diffuse and form SrTiO_3 even though the schematic figure does not show the inter-diffusion.

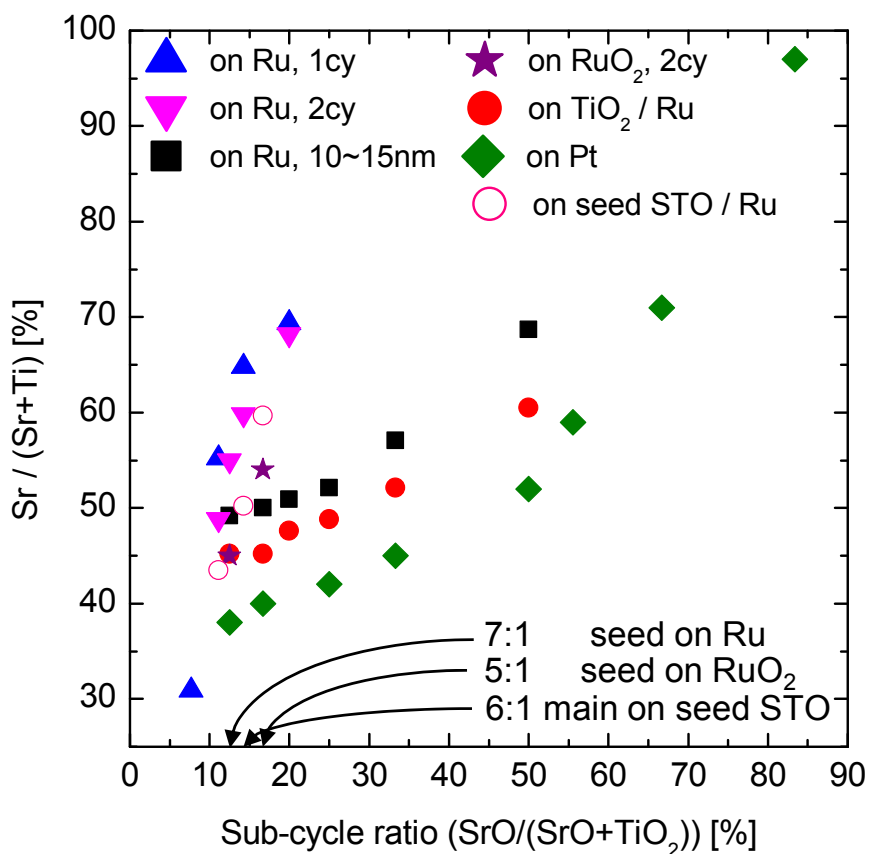


Figure 3.7 Variations of the cation compositions (Sr/(Sr+Ti)) of STO films deposited on various substrate with various super-cycles as a function of sub-cycle ratio (SrO/(SrO+TiO₂))

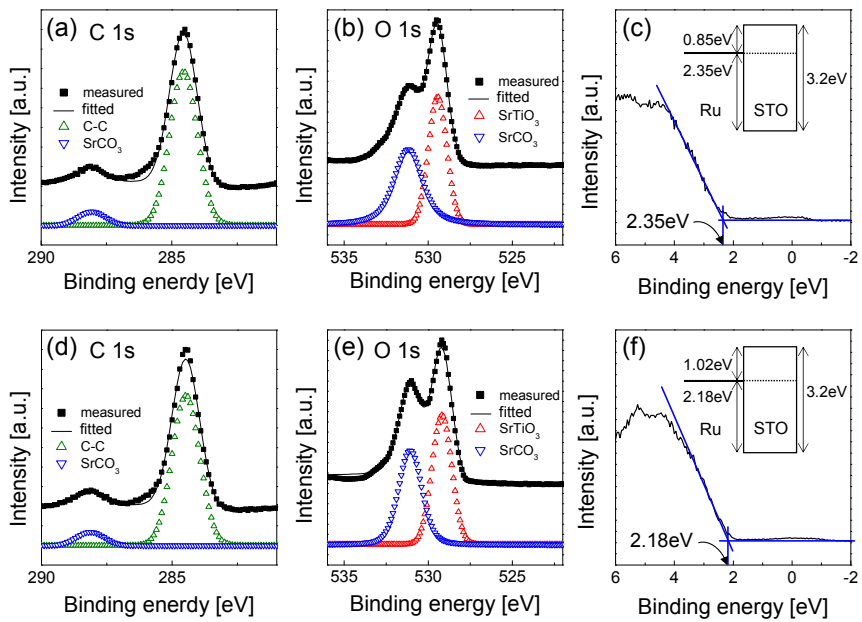


Figure 3.8 The XPS spectra of (a) C 1s, (b) O 1s, and (c) valence band structure of STO(11 nm)/Ru and (d) C 1s, (e) O 1s, and (f) valence band structure of STO(6nm) /TiO₂-(4 nm)/Ru.

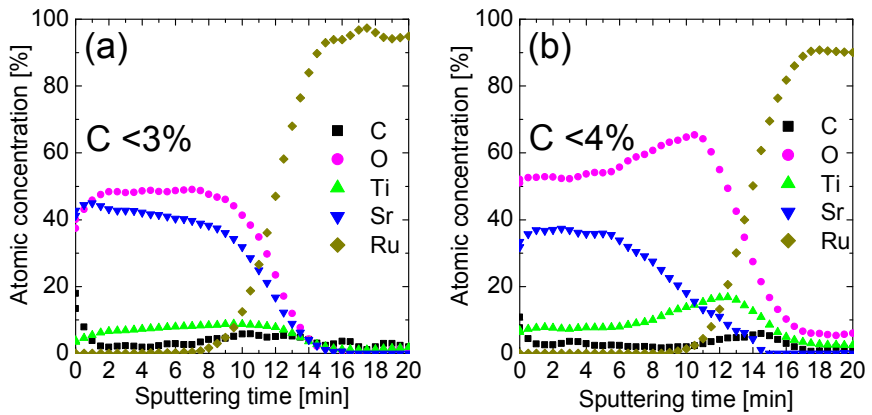


Figure 3.9 The AES depth profiles of (a) 6-nm-thick main STO layer with Sr composition of 50% + 3-nm-thick seed STO layer with 55% Sr composition, which was initially 6-nm thick before crystallization annealing; (b) 4-nm-thick main STO layer with Sr composition of 47% + 2-nm-thick seed STO layer with 55% Sr composition, which was 3-nm thick before RTA + 3-nm-thick TiO₂ barrier layer).

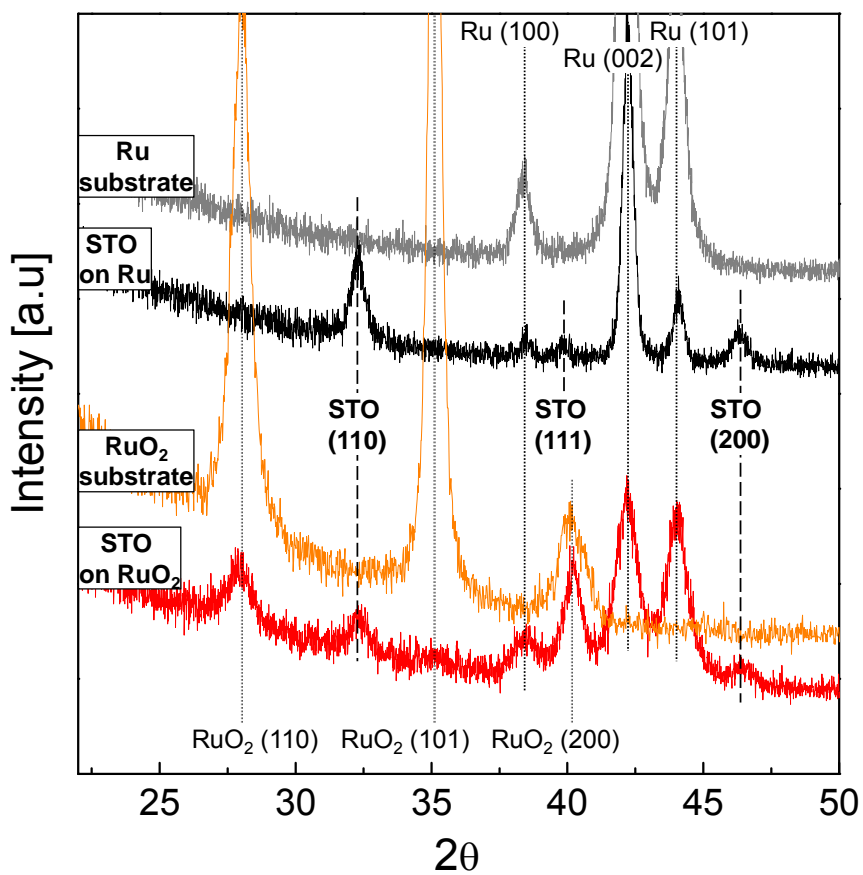


Figure 3.10 Glancing angle mode X-ray diffraction patterns of Ru and RuO₂ substrates, and STO films on Ru and RuO₂ substrates.

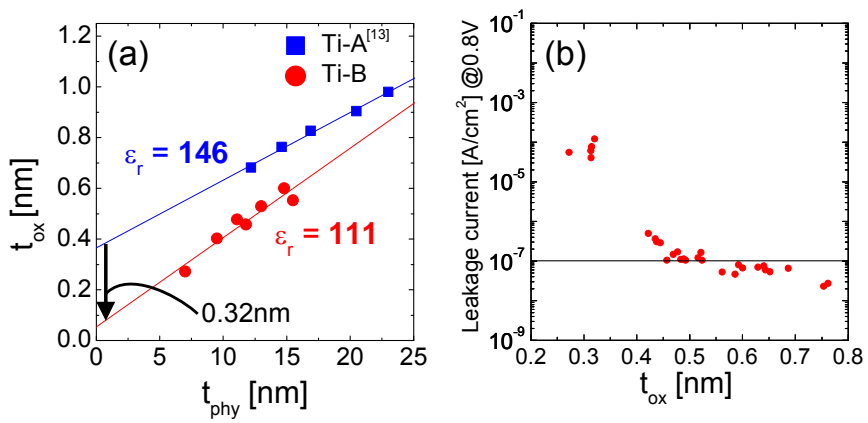


Figure 3.11 Variations of t_{ox} of STO films deposited with different Ti precursors as a function of t_{phy} and (b) the leakage current density(@0.8 V) versus t_{ox} plot of STO films deposited on Ru substrate with Ti-B precursor. Data for Ti-A precursor case was reproduced from Ref.13.

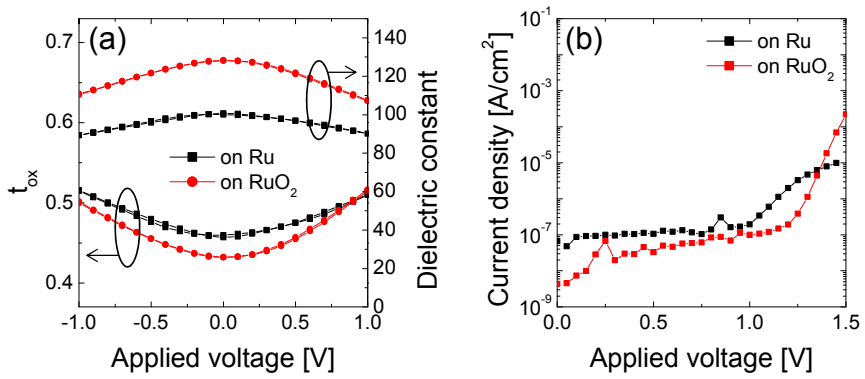


Figure 3.12 The t_{ox} and the dielectric constant and (b) the leakage current density versus applied voltage plot of the in-situ crystallized STO deposited on Ru substrate and on RuO₂ substrate with Ti-B precursor.

3.1.4. Summary

STO thin films were prepared by an ALD method at a substrate temperature of 370 °C on Ru and RuO₂ substrates, employing the Sr(ⁱPr₃Cp)₂ and Cp*Ti(OMe)₃ as the Sr and Ti precursors, respectively. While the Cp*Ti(OMe)₃ precursor showed enhanced CVD-like deposition behavior at the initial stage of the deposition process on both substrates, it was beneficial to control the cation stoichiometry from an early stage of ALD STO given the vigorous CVD-like reaction of SrO deposition. When the influences of the substrate were suppressed by the thicker STO layer thickness, the saturated growth rate was enhanced to 0.123 nm/cycle, which is even higher than the previous STO ALD using the same Sr precursor and Ti(O-*i*Pr)₂(tmhd)₂. An even more important aspect of this new ALD route lies in the elimination of the interfacial reaction barrier layer, such as TiO₂ or Al₂O₃, which largely degrades the maximum attainable capacitance density. When the optimized STO layer was deposited on the RuO₂ substrate via the two-step process, a minimum t_{ox} of 0.43 nm with a very low leakage current density ($8 \times 10^{-8} \text{ Acm}^{-2}$ at 0.8 V) was achieved, which is ascribed to the largely decreased interfacial capacitance component. Even with the involvement of the CVD-like component at the early stage of the ALD process, high controllability of the composition and thickness depending on the types of substrate was confirmed, making this ALD process highly promising for the mass-production of STO capacitor for DRAMs with a design rule <20 nm.

3.1.5. Bibliography

1. S. K. Kim, S. W. Lee, J. H. Han, B. Lee, S. Han, and C. S. Hwang, *Adv. Funct. Mater.*, 2010, 20, 2989.
2. D.-S. Kil, H.-S. Song, K.-J. Lee, K. Hong, J.-H. Kim, K.-S. Park, S.-J. Yeom, J.-S. Roh, N.-J. Kwak, H.-C. Sohn, J.-W. Kim, S.-W. Park, *VLSI Symp. Technol. Dig.*, 2006, 38.
3. H. J. Cho, Y. D. Kim, D. S. Park, E. Lee, C. H. Park, J. S. Jang, K. B. Lee, H. W. Kim, Y. J. Ki, I. K. Han, Y. W. Song, *Solid-State Electron.*, 2007, 51, 1529.
4. J. H. Han, W. Lee, W. Jeon, S. W. Lee, C. Ko and J. Gatineau, and C. S. Hwang, *Chem. Mater.* 2012, 24, 4686.
5. M. Vehkamäki, T. Hänninen, M. Ritala, M. Leskelä, T. Sajavaara, E. Rauhala, and J. Keinonen, *Chem. Vap. Deposition*, 2001, 7, 75.
6. N. Menou, M. Popovici, S. Clima, K. Opsomer, W. Polspoel, B. Kaczer, G. Rampelberg, K. Tomida, M. A. Pawlak, C. Detavernier, D. Pierreux, J. Swerts, J. W. Maes, D. Manger, M. Badylevich, V. Afanasiev, T. Conard, P. Favia, H. Bender, B. Brijs, W. Vandervorst, S. Van Elshocht, G. Pourtois, D. J. Wouters, S. Biesemans, and J. A. Kittl, *J. Appl. Phys.*, 2009, 106, 094101.

7. M. A. Pawlak, B. Kaczer, M.-S. Kim, M. Popovici, K. Tomida, J. Swerts, K. Opsomer, W. Polspoel, P. Favia, C. Vrancken, C. Demeurisse, W.-C. Wang, V. V. Afanas'ev, W. Vandervorst, H. Bender, I. Debusschere, L. Altimime, and J. A. Kittl, *Appl. Phys. Lett.*, 2010, 97, 162906.
8. M. A. Pawlak, B. Kaczer, M.-S. Kim, M. Popovici, J. Swerts, W.-C. Wang, K. Opsomer, P. Favia, K. Tomida, A. Belmonte, B. Govoreanu, C. Vrancken, C. Demeurisse, H. Bender, V. V. Afanas'ev, I. Debusschere, L. Altimime, and J. A. Kittl, *Appl. Phys. Lett.*, 2011, 98, 182902.
9. M. A. Pawlak, J. Swerts, M. Popovici, B. Kaczer, M.-S. Kim, W.-C. Wang, K. Tomida, B. Govoreanu, J. Delmotte, V. V. Afanas'ev, M. Schaekers, W. Vandervorst, and J. A. Kittl, *Appl. Phys. Lett.* 2012, 101, 042901.
10. O. S. Kwon, S. K. Kim, M. Cho, C. S. Hwang and J. Jeong, *J. Electrochem. Soc.*, 2005, 152, C229.
11. W. Lee, J. H. Han, S. W. Lee, S. Han, W. J. Jeon, and C. S. Hwang, *J. Mater. Chem.*, 2012, 22, 15037.
12. S. W. Lee, O. S. Kwon, J. H. Han and C. S. Hwang, *Appl. Phys. Lett.*, 2008, 92, 222903.

13. S. W. Lee, J. H. Han, S. Han, W. Lee, J. H. Jang, M. Seo, S. K. Kim, C. Dussarrat, J. Gatineau, Y.-S. Min and C. S. Hwang, *Chem. Mater.*, 2011, 23, 2227.
14. S. W. Lee, J. H. Han, S. K. Kim, S. Han, W. Lee and C. S. Hwang, *Chem. Mater.*, 2011, 23, 976.
15. T. P. Holme and F. B. Prinz, *J. Phys. Chem. A*, 2007, 111, 8147.
16. NIST, X-ray Photoelectron Spectroscopy Database, <http://srdata.nist.gov/xps/>.
17. C. S. Hwang, *J. Appl. Phys.* 2002, 92, 432.
18. E. V. Jelenkovic and K. Y. Tong, *J. Vac. Sci. Technol. B*, 2004, 22, 2319.
19. S. K. Kim, S. Han, W. Jeon, J. H. Yoon, J. H. Han, W. Lee, and Cheol Seong Hwang, *ACS Appl. Mater. Interfaces*, 2012, 4, 4726.
20. J. H. Han, S. Han, W. Lee, S. W. Lee, S. K. Kim, J. Gatineau, C. Dussarrat, and C. S. Hwang, *Appl. Phys. Lett.*, 2011, 99, 0229

3.2. Reducing Microdefects Formation by Adjusting Rapid Thermal Annealing Cooling Rate

3.2.1. Introduction

Although researches of various kinds of memory devices with new operation principles are reported in a recent few decades, dynamic random access memory (DRAM) is still one of the most significant main memory units for computers and mobile devices. Since DRAM has noticeable density, read / write / erase time and read / write cycles than other being developed memories such as ferroelectric, resistive switching, and magnetic random access memory, continuous researches on DRAM should be performed.^[1]

DRAM consists of one transistor and one capacitor and as the device scaling continuous, securing a certain value of capacitance (20~25fF/cell) confronts with difficulty. As capacitance is proportional to the electrode area and is inverse proportional to the dielectric thickness, the effort of retaining the necessary capacitance in decreasing cell size was containing both two methods: increasing the electrode area by adopting complicated three dimensional structure with high aspect ratio and reducing the dielectric thickness by replacing material with high insulating dielectric and electrode pair to consider the leakage current increase. However, since capacitance is

also proportional to the permittivity of dielectric, employing higher dielectric constant material such as TiO_2 and SrTiO_3 (STO) is a promising approach.^[2-6]

The deposition method as well as the kind of material should be selected with cautions. Not only that the deposited film must be conformal on three dimensional structure, but also that the film should contain little defects in the film. However, the films suffer from various detrimental conditions during film growth, annealing, doping, sequential film deposition and so forth, which can cause developments of defects. Since these defects worsens the film properties including reliability, endurance, and fundamental target properties, formation of defects should be restrict to the utmost.^[7-11]

In this study, the fabrication process of metal-insulator-metal capacitor with atomic layer deposited (ALD) STO films was controlled elaborately. By lowering the cooling rate after crystallization annealing, stress was reduced and better bulk properties could be obtained by adjusting the crystallization annealing process. Comparison of two processes, rapid cooling and slow cooling, was performed by analyzing the film properties in various methods to confirm the feasibility of STO films to DRAM capacitor application.

3.2.2. Experimental

STO films were deposited in a traveling wave-type ALD reactor (CN-1 Co, Plus-100) for a 4-inch-diameter single wafer. $\text{Sr}(\text{iPr}_3\text{Cp})_2$ and $\text{Ti}(\text{Me}_5\text{Cp})(\text{OMe})_3$ (synthesized by Air Liquide) were employed as the Sr and Ti precursors, respectively. The canister of the Ti and Sr precursor were heated to 80 and 90 °C, respectively, to maintain the appropriate vapor pressures of the precursors. Ar carrier gas was bubbled through the canisters to deliver the Sr and Ti precursors to the reaction chamber at a flow rate of 200 sccm, and the working pressure of the ALD reactor fluctuated near 0.7 Torr. H_2O , which was used as the oxygen source for Sr precursor, was cooled down to 3 °C to control its high vapor pressure, and O_3 at a concentration of 250 g/m³ was used as the oxygen source for the TiO_2 sub-layers.^[5]

The ALD sub-cycle process for SrO and TiO_2 consisted of precursor injection (3s), followed by Ar purge (5s), oxygen source injection (2s), and Ar purge (5s), which was confirmed to be consistent with the saturated ALD conditions.^[5] The ALD super-cycles for STO deposition consist of ALD sub-cycles of SrO and TiO_2 layers with different cycle ratios to vary the cation composition. The T_g was set at 370°C, and Ru(30 nm)/ Ta_2O_5 (8 nm)/ SiO_2 (100 nm)/Si wafers were used as substrates. Since the single STO layer growth at this T_g still did not induce in-situ crystallization, the two-step process was also employed in this work. Crystallization-annealing of the thin seed STO layer

was performed in an RTA system at 650 °C for 2 minutes in an N₂ atmosphere (purity >99.99%).^[5]

The layer density and cation composition of STO films were confirmed by X-ray fluorescent spectroscopy (XRF, Themoscintific, ARL Quant'X). The physical thickness of the STO films on Ru substrate was measured using an ellipsometer. The chemical binding states of the films were determined by X-ray photoelectron spectroscopy (XPS, ThermoVG, SIGMA PROBE). The crystal structure of the film was investigated by glancing angle mode X-ray diffraction using a Cu K α X-ray source (GAXRD, PANalytical, X'Pert Pro). The incidence angle, scan step size, and time per step during the GAXRD measurement were 2°, 0.02°, and 1 sec, respectively. The planar-structured metal-insulator-metal capacitors were fabricated by depositing an 20-nm-thick RuO₂ and 80-nm-thick Pt, in sequence, as a top electrode by sputter through a shadow mask (with a 0.3-mm hole diameter). The electrical properties, including the capacitance and leakage current, were measured using an HP4194A impedance analyzer at 10 kHz and an HP4140 picoammeter, respectively.

3.2.3. Results and Discussion

STO films for application of DRAM capacitor dielectrics should have crystal structure of Perovskite. Well crystallized STO material has bulk dielectric constant of about 150 even the thickness of the film is under 20 nm. [3-5] However, in the recent study with $\text{Sr}(\text{Pr}_3\text{Cp})_2$ and $\text{Ti}(\text{Me}_5\text{Cp})(\text{OMe})_3$ as Sr and Ti precursor, deposited STO films on Ru with O_3 at high temperature which enables in-situ crystallization on crystallized seed layer showed bulk dielectric constant of only 111, which is relatively lower than another previous reports. Therefore, detailed analyses were performed to find the reason of poor electrical property.

Figure 13 (a) and (b) shows the surface morphology of 14 nm thick STO films which were grown by so-called 2 step growth, which RTA process was included in after 5 nm thick seed layer deposition. Many dark regions are easily seen which seems to be nanocracks. However, RMS roughness measured by AFM was only 1.06nm which is within acceptable range taking into account that the whole thickness of deposited STO film is 14nm. (Figure 13 (c) and (d)) In consideration that two results are contrary to each other, the surface morphology of each step of STO fabrication was confirmed. Figure 14 (a), (b), and (c) shows the SEM and AFM image of STO seed layer, annealed STO seed layer, and STO main layer, respectively. RMS roughness of film measured by AFM was included in the image. Before crystallization annealing

of the STO seed layer, the surface of the film is smooth and any defect was detected. However, after RTA process, nanocracks appeared obviously and RMS roughness of the films surface increased. When STO main layer was additionally grown on annealed STO seed layer, defects became more clearly and grain size increased while porous sapce enlarged. The RMS roughness was also increased after main layer deposition. These step-by-step analyses indicate definitely that the defects were developed during RTA step.

Such nanocracks in films are usually caused by biaxial stress. There are commonly two kinds of stresses in films: intrinsic and extrinsic stress.^[12, 13] Intrinsic stress means growth stress which arose by volume shrinkage during grain growth. When the film becomes thicker, the grain size of the film becomes thicker by coalescence of the already existing small grains with each other. In this stage, decreased grain boundary region is remained as empty space and induces tensile stress to the films. Origin of the intrinsic stress is in figure 15 (a). The tensile stress of the film causes cracks or sunken grains which are observed in figure 13 (a) and (b). However, if the intrinsic stress was the main reason, defects should also be seen before annealing process. In addition, that the crystal structure varied from amorphous to perovskite structure when heat was applied to the film means that the atoms are mostly rearranged.^[3] Although if there was existing weak intrinsic stress in the film, since enough energy was delivered by heat to the atoms to move the position, the film should be in stress free state after RTA process. However, intrinsic

stress could be a good explanation of the morphology of STO main layer. While the thickness of whole STO film became larger than before main layer deposition, the crystallized grain would be also grown and intrinsic stress could enlarge the nanocracks and voids.

Extrinsic stress is caused by difference of thermal expansion coefficient (TEC) between film and substrate. The stress can be expressed as equation 1,

$$\varepsilon = - (TEC_A - TEC_B)(T - T_0) = -\Delta TEC \Delta T \dots\dots\dots\text{equation 1}$$

where ε is stress, TEC is the thermal expansion coefficient, and T is the temperature. As the TECs of STO and Si are $9.4 \times 10^{-6} \text{ K}^{-1}$ and $2.6 \times 10^{-6} \text{ K}^{-1}$, STO expands over 4 times more than Si substrate does with equivalent temperature increase.^[14-16] Therefore, if the thermal stress induced by temperature increase is the main cause of defect formation, STO films should have the compressive stress, and hillocks or extrusions must be seen instead of porous surface. On the other hand, appearing many cracks and voids indicate that tensile stress during the temperature lowering is the major origin of defects observed by SEM. This coincides well with the explanation that since the nanocracks are created before main layer deposition, RMS roughness of surface of STO main layer is not severely high. The self-limited

reaction of ALD process of STO main layer almost maintains the original features of STO seed layer.

Since the STO seed layer could be less crystallized or remained in amorphous around the defects, main STO layer which should be in-situ crystallized on well crystallized bottom matrix would fail to be well crystallized. Therefore, cooling process after RTA was adjusted. Two kind of cooling process is included in Figure 16. While the temperature of the substrate was cooled down to room temperature at once by cooling water around the annealing chamber after 2 min annealing at 650°C in N₂ atmosphere (indicated as 'rapid cooling'), 3 step were added when the RTA process is finished. ('slow cooling') More heat and time were supplied to maintain the films for 30 sec at 500°C, for 30 sec at 350°C, and for 30 sec at 200°C to give composure to atoms in films to find the most stable positions. This can reduce the thermal stress applied to the STO seed layer.

Figure 17 (a) and (b) shows the surface morphology of STO seed layer after RTA with newly introduced slow cooling process and STO main layer which was grown on the equivalent annealed seed layer, respectively. Nanocracks are still observed in both SEM and AFM images in figure 5 (a), however, the gap between normal texture was shrank compared with figure 2 (b). Moreover, it is more apparent that thermal stress was reduced in slow cooling system, although the intrinsic stress still induced tensile stress to the 15 nm thick STO

film in figure 17 (b). Figure 18 summarizes the roughness of the films confirmed in this study. Although the RMS roughness increased after main layer deposition, there was negligible variation after seed layer deposition in both processes. The remarkable point is that RMS roughness was even decreased after RTA process when the slow cooling rate was adopted, while annealing step was the most worsening through the whole fabrication process when the rapid cooling rate was taken.

Figure 19 shows the chemical nature of STO films analyzed by XPS. Examining the C 1s and O 1s in figure 19 (a) and (b), respectively, there was almost no difference between two cooling processes. There are still carbon and strontium carbonate peaks in XP spectra, which is thought to be indicated that the film surface was contaminated by carbon from the air exposure before the sample analyzing. STO peak was also seen in figure 19 (b) and after surface etching before XPS analysis, all carbon and carbonate peak was disappeared (data not shown), while the STO peak was remained. Crystallinities of two samples were also confirmed by GAXRD in figure 20. Sharp and obvious peaks of STO (110), (200), (211) were obtained with the crystal peaks of Ru substrate.

Electrical properties of RuO₂ - STO - Ru, metal-insulator-metal capacitors were investigated in figure 21. Figure 21 (a) show equivalent oxide thickness, t_{ox} in the variation of physical thickness, t_{phy} . The thicknesses of STO seed

layer were fixed to 3 nm after annealing and only the thickness of main layer was controlled. By the best-linear-fitting of the data, bulk dielectric constant ϵ_r of the STO film and interfacial equivalent oxide thickness t_{ox}^i were extracted from $t_{ox} = t_{phy} \times (3.9 / \epsilon_r) + t_{ox}^i$. The ϵ_r values of the STO films of rapid cooling process was 101, a little smaller than the previous result. [5] This is more reliable value since the number of data points was increased; electrical results of rapid cooling process with RuO₂ top electrode and Pt top electrode which show in similar trend were both employed to the linear fitting. The bulk dielectric constant of STO film which slow cooling process after RTA adopted to was 135 which was 34% improved. However, the Y-axis intercept which indicates dielectric property lowering by the interface of dielectric and electrode was increased from 0.19 nm to 1.21 nm for about 1.02 nm. Because of the worsened interface by long annealing time, the slow cooling progressed capacitors do not have any advantage in the overall electrical property. The critical thickness of STO film which satisfied the leakage current density specification required in DRAM capacitors industry ($<10^{-7} \text{ A/cm}^2$ @ 0.8V) was 10nm with rapid cooling process which was further reduced than previous report by adopting RuO₂ instead of Pt as top electrode. However, rapidly cooled STO sampled after seed layer annealing needed 13 nm for equivalent leakage property. Consequently, 0.39 nm and 0.46 nm of t_{ox} was obtained with leakage current density of $9 \times 10^{-8} \text{ A/cm}^2$ and $1 \times 10^{-7} \text{ A/cm}^2$ with rapid cooling process and slow cooling process, respectively.

For further consideration, STO films were analyzed by TEM. Figure 22 shows the cross-section image of Pt - in-situ crystallized STO - Ru structure with rapid cooling process. STO film showed small non-uniformity in thickness within 2 nm. The region of STO with relatively smaller thickness which corresponds to the void region was almost amorphous, whereas that of larger thickness which is normal grain was mostly crystalline which are confirmed by HRTEM. This indicate that the STO films deposited with slow cooling have more portion of normal grain with better crystallinity than that with rapid cooling. Although the slow cooled STO film had also many amorphous regions, which is the reason of relatively low dielectric constant in comparison that STO materials in bulk state have permittivity of ~ 300 .^[6]

The reason of difference of leakage current property and Y-intercept of figure 21a between STO based capacitors with rapid cooling process and slow cooling process could be argued in figure 23b. Since the total annealing time is different between two processes, the slow cooling process gives higher energy and longer time to the interface of STO layer and Ru substrate. Therefore, Ru and STO could be further intermixed each other in slow cooling process than in rapid cooling process. It is easily noticed that the interface of STO and Ru is clearer in rapid cooling sample in both crystallized and amorphous region, which caused better dielectric property of interface and smaller degradation of insulating property.

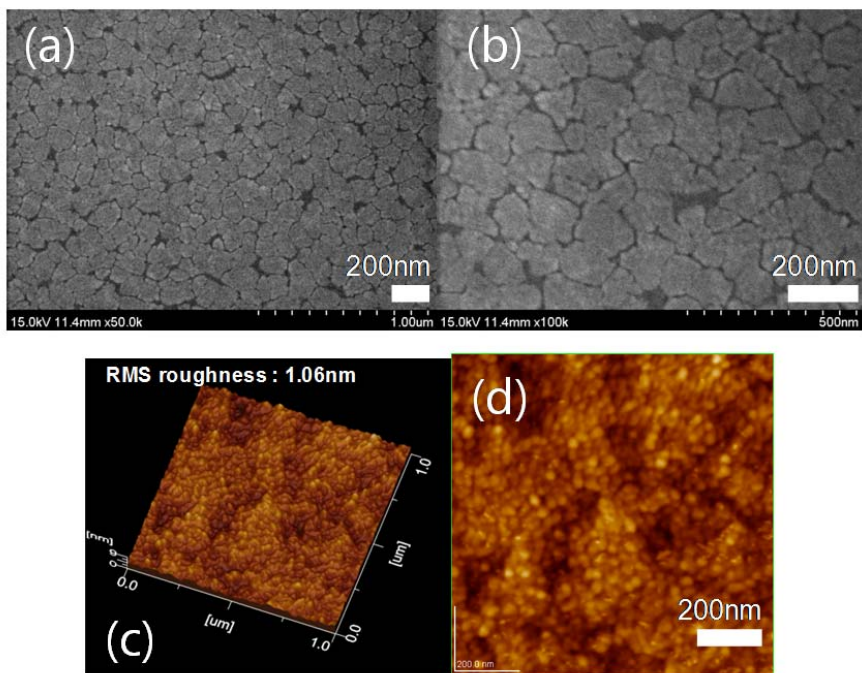


Figure 3.13 SEM and AFM image of 14nm thick STO film

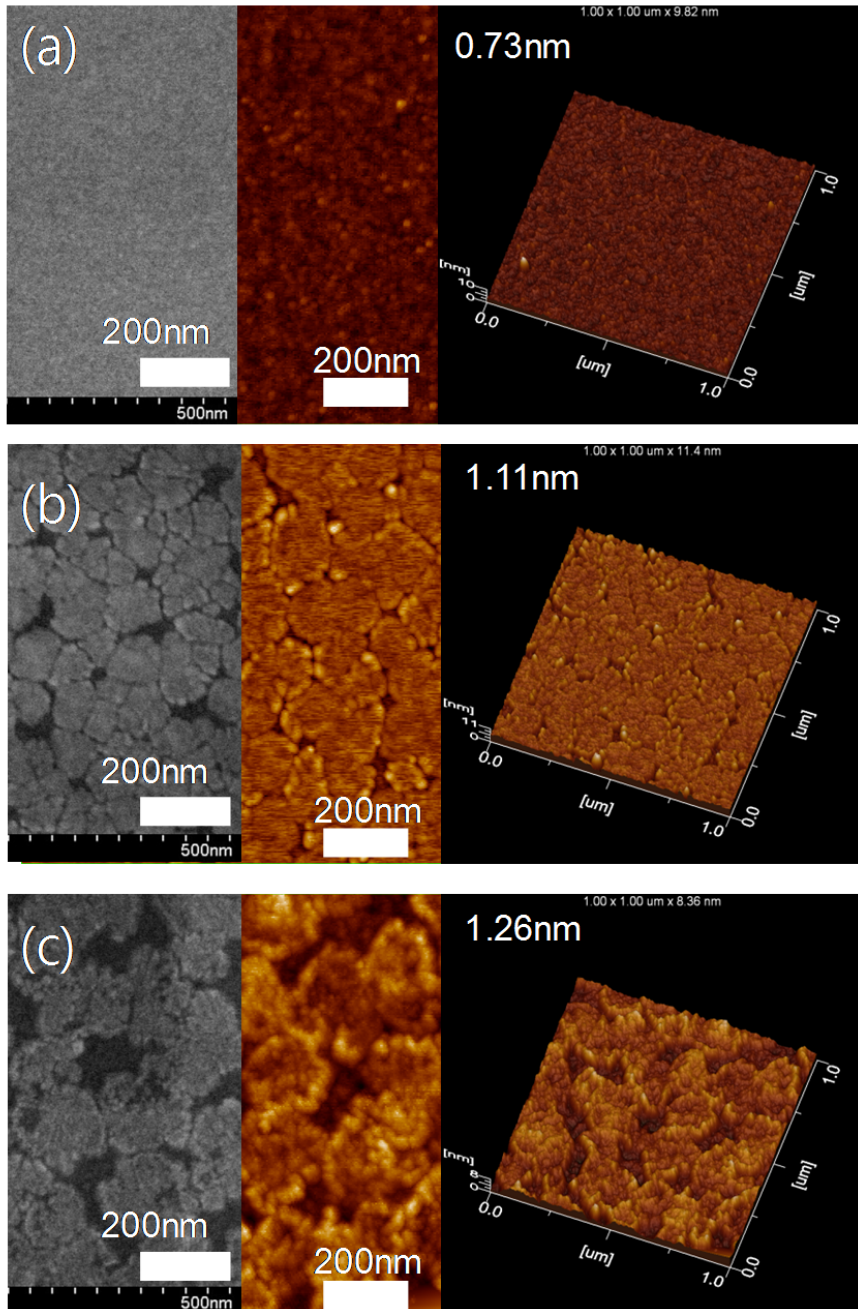


Figure 3.14 SEM and AFM image of (a) STO seed layer (b) annealed STO seed layer (c) STO main layer

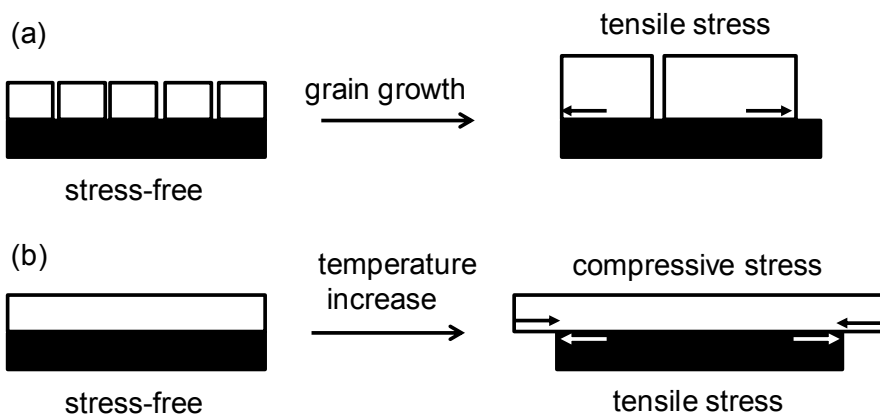


Figure 3.15 The schematic diagram of origins of (a) intrinsic stress induced by grain growth and (b) extrinsic stress induced by temperature increase

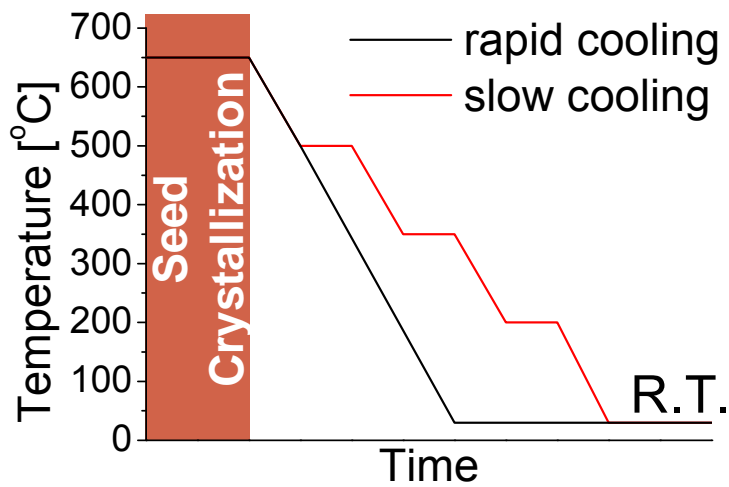


Figure 3.16 rapid cooling (650 °C → room temperature) and slow cooling (650°C → 500°C 30s → 350°C 30s → 200°C 30s → room temperature) after RTA process

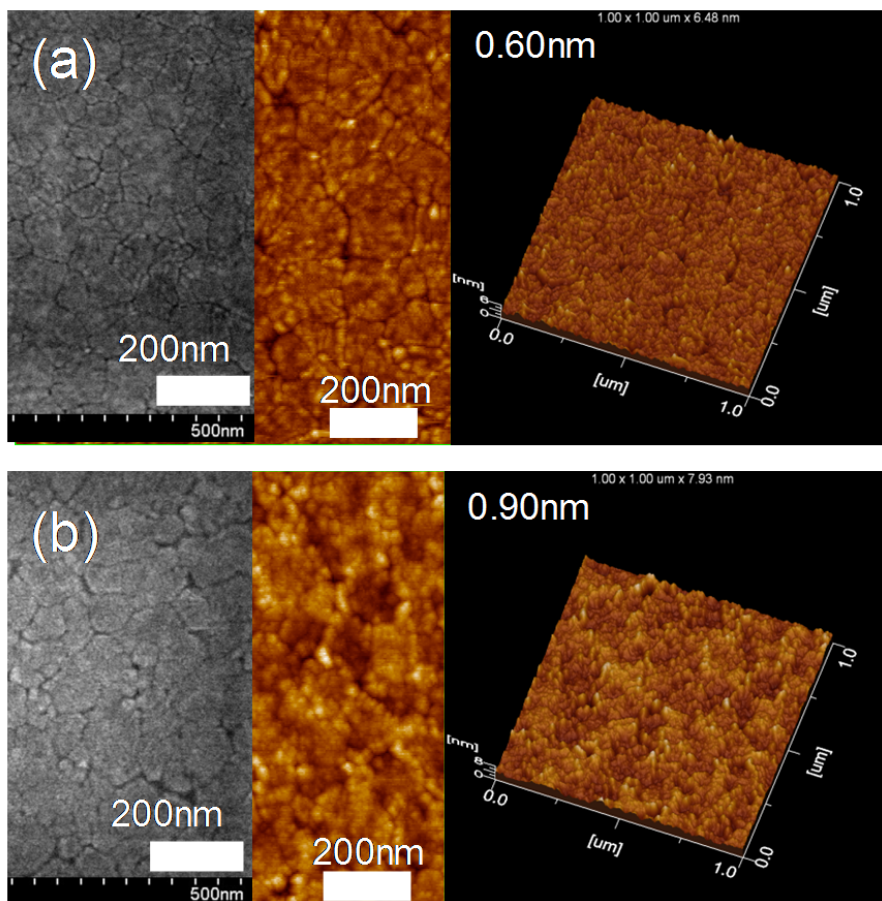


Figure 3.17 SEM and AFM images with RMS roughness of (a) STO seed layer after slow cooling and (b) STO main layer

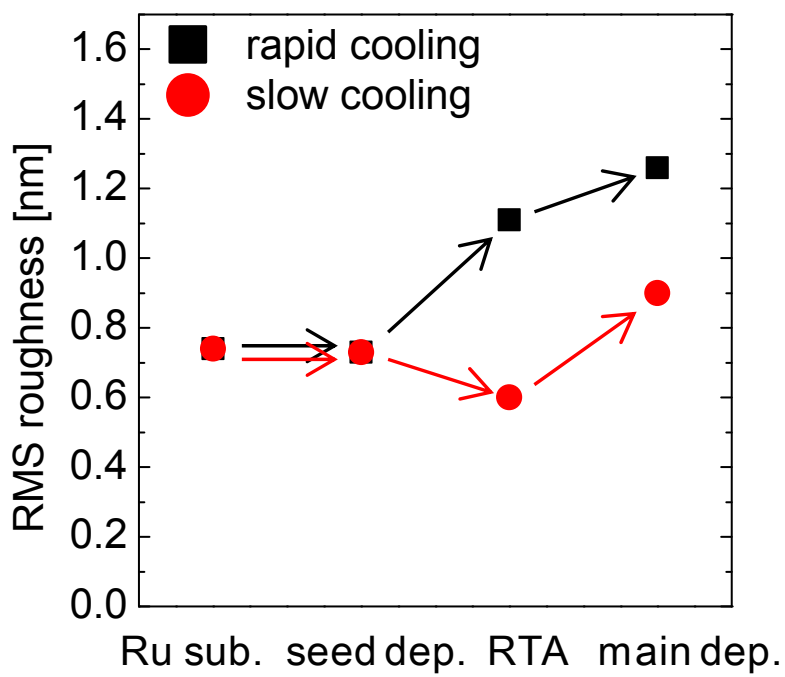


Figure 3.18 The variations of RMS roughness of sample surface variation at each step

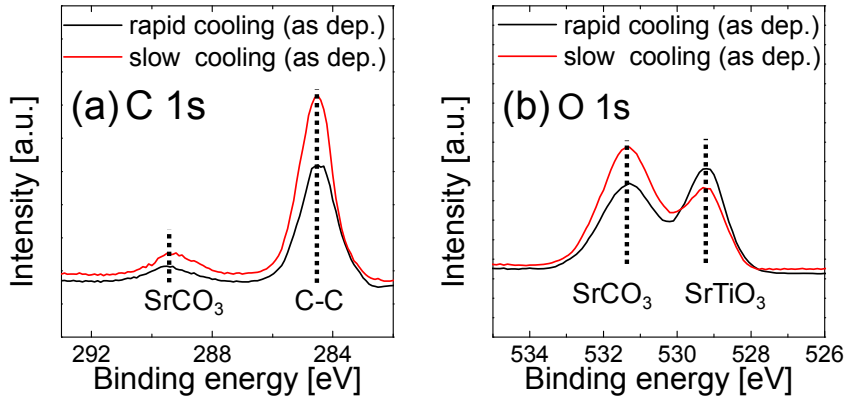


Figure 3.19 XP Spectra of (a) C 1s and (b) O 1s of STO films with rapid cooling process and slow cooling process

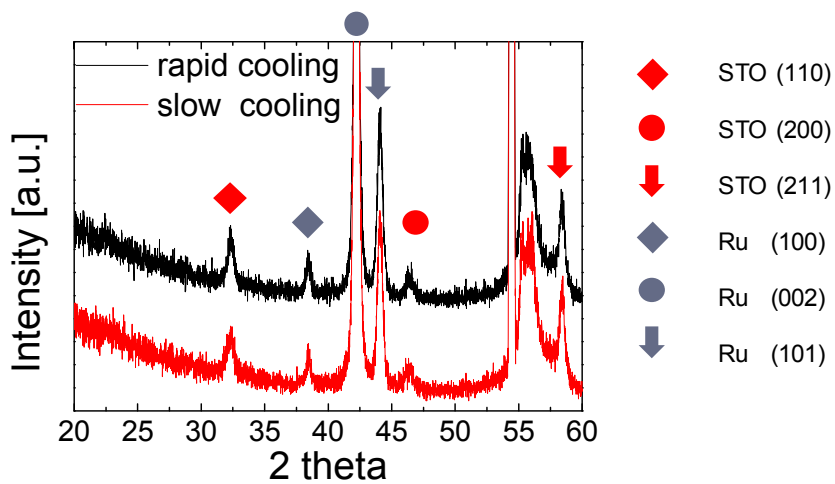


Figure 3.20 GAXRD of STO films with rapid cooling process and slow cooling process

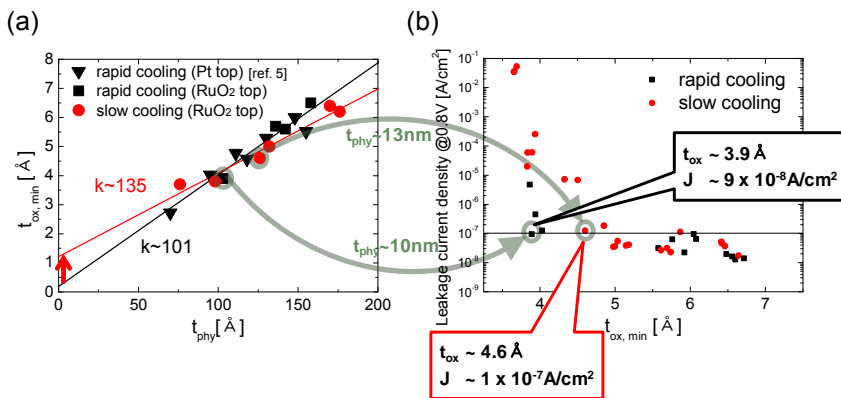


Figure 3.21 Electrical properties of STO films. (a) Minimum equivalent oxide thickness vs. physical oxide thickness and (b) leakage current density vs. minimum equivalent oxide thickness.

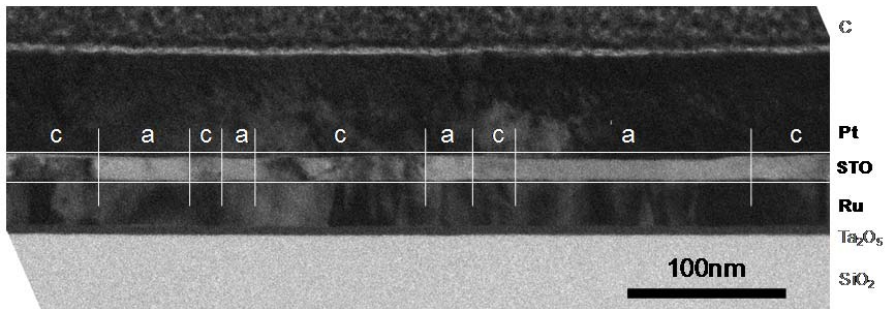


Figure 3.22 cross-section TEM image of Pt - in-situ crystallized STO - Ru structure with rapid cooling process

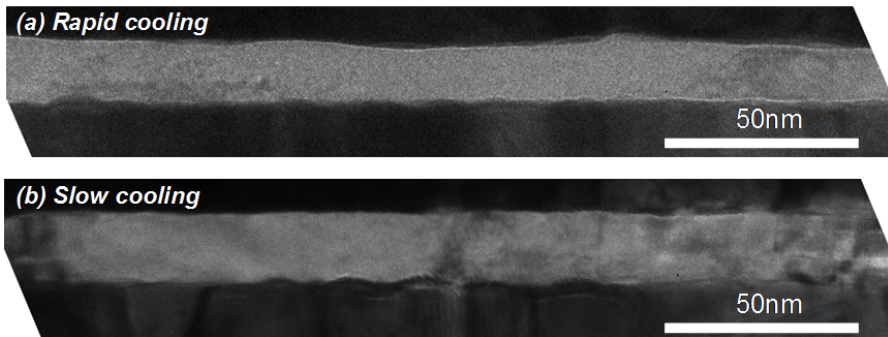


Figure 3.23 cross-section TEM image of Pt - in-situ crystallized STO - Ru structure (a) with rapid cooling process and (b) with slow cooling process.

3.2.4. Summary

Cooling rate after RTA of STO seed layer was lowered to improve the microstructure with less defects. Ameliorated surface morphology and roughness were implied better crystallinity of STO films and RuO₂ - STO - Ru capacitors showed higher bulk dielectric constant of 135 with 34% improvement. However, interfacial properties were degraded and enhancement of net electrical property was not obtained as a result. Nevertheless, it is worthwhile that this result indicates the possibility of advance in STO film as a capacitor dielectric with t_{ox} under 0.4nm with low leakage level.

3.2.5. Bibliography

1. ITRS roadmap 2013.
2. S. K. Kim, S. W. Lee, J. H. Han, B. Lee, S. Han, and C. S. Hwang, *Adv. Funct. Mater.*, 2010, 20, 2989.
3. S. W. Lee, J. H. Han, S. Han, W. Lee, J. H. Jang, M. Seo, S. K. Kim, C. Dussarrat, J. Gatineau, Y.-S. Min and C. S. Hwang, *Chem. Mater.*, 2011, 23, 2227.
4. W. Lee, J. H. Han, S. W. Lee, S. Han, W. J. Jeon, and C. S. Hwang, *J. Mater. Chem.*, 2012, 22, 15037.
5. W. Lee, J. H. Han, W. Jeon, Y. W. Yoo, S. W. Lee, S. K. Kim, C.-H. Ko, C. Lanslaot-Matras, C. S. Hwang, *Chem. Mater.*, 2013, 25, 953.
6. R. C. Neville, B. Hoeneisen, and C. A. Mead, *J. Appl. Phys.* 1972, 43, 2124.
7. M. A. Pawlak, B. Kaczer, M.-S. Kim, M. Popovici, K. Tomida, J. Swerts, K. Opsomer, W. Polspoel, P. Favia, C. Vrancken, C. Demeurisse, W.-C. Wang, V. V. Afanas'ev, W. Vandervorst, H. Bender, I. Debusschere, L. Altimime, and J. A. Kittl, *Appl. Phys. Lett.*, 2010, 97, 162906.

8. S. W. Lee, O. S. Kwon, J. H. Han, and C. S. Hwang, *Appl. Phys. Lett.*, 2008, 92, 222903.
9. S. W. Lee, J. H. Han, and Cheol Seong Hwang, *Electrochem. Solid-State Lett.*, 2009, 12, G69.
10. M. A. Pawlak, B. Kaczer, M.-S. Kim, M. Popovici, J. Swerts, W.-C. Wang, K. Opsomer, P. Favia, K. Tomida, A. Belmonte, B. Govoreanu, C. Vrancken, C. Demeurisse, H. Bender, V. V. Afanas'ev, I. Debusschere, L. Altimime, and J. A. Kittl, *Appl. Phys. Lett.*, 2011, 98, 182902.
11. M. A. Pawlak, J. Swerts, M. Popovici, B. Kaczer, M.-S. Kim, W.-C. Wang, K. Tomida, B. Govoreanu, J. Delmotte, V. V. Afanas'ev, M. Schaekers, W. Vandervorst, and J. A. Kittl, *Appl. Phys. Lett.* 2012, 101, 042901.
12. M. Ohring, "Materials Science of Thin Films", Academic Press, 2nd edition, 2001.
13. I. H. Shames, J. M. Pitarresi, "Introduction to Solid Mechanics", Prentice Hall, 3rd edition, 1999.
14. F. W. Lytle, *J. Appl. Phys.*, 1964, 35, 2212.
15. CINDAS, "Thermophysical Properties of Matter", The TPRC Data Series, Vol. 13. Thermal Expansion--Nonmetallic Solids, Plenum, 1977.

16. M. Okaji, *Int. J. Thermophys.*, 1988, 9, 1101.

4. Atomic Layer Deposition of SrTiO₃ Films with novel Sr-precursor

4.1. Introduction

For its extremely high permittivity compared with other typical materials, SrTiO₃ (STO) is a promising candidate material for dielectric of next generation DRAM capacitor. Many studies have been reported about STO as dielectric material in metal-insulator-metal capacitor and dielectric constants showed mostly over 100 even in thin films with thickness under 20nm.^[1-4] However, not only the material, but also the deposition method should be carefully considered. Since the capacitance is proportional to the electrode area of capacitor, DRAM capacitor is developed to increase the aspect ratio in 3D structure.^[5] Therefore, studies of fabrication method such as atomic layer deposition (ALD) which shows conformal film deposition due to its self-saturation growth are necessary. In addition, STO deposition for capacitor application needs several particular conditions: deposition at high process temperature, employing Ru based electrode, and using O₃ as oxidant.

First of all, the post deposition annealing of STO film over 600°C, which is the promising annealing temperature to crystallize the STO film to perovskite structure with high dielectric constant, causes nanocracks and voids in the

film. These nanodefects work as leakage paths of dielectric and the insulating property degrades after post deposition annealing. A group in Interuniversity Microelectronics Center (IMEC) suggested to employ Sr-rich STO films. The crystallization annealing of Sr-rich STO films restrict the grain growth and morphology of STO film was improved. By depositing another TiO₂ layer under STO layer, the overall cation composition of dielectric film could be reached to stoichiometric composition after intermixing of TiO₂ and Sr-rich STO during annealing process.^[4, 6, 7] However, as the film thickness of insulator decreases, separating TiO₂ layer and Sr-rich STO becomes difficult in the point of view that the total Sr to Ti ratio should be maintained near one to one. Another solution to avoid the formation of leakage paths is adopting so-called 2 step deposition which includes annealing process between two deposition: seed layer deposition and main layer deposition. In this way, the preliminarily deposited STO seed layer was crystallized to perovskite firstly, and the following STO main layer involves in-situ crystallization even though another additional annealing was absence after main layer deposition. At this point, deposition temperature of STO main layer should be preserved as high as over 350°C for successful in-situ crystallization on STO seed layer with perovskite structure. Since there is not any further annealing process, the morphology could be remained with fine grains and insulating property of in-situ crystallized STO films are superior than that of ex-situ crystallized STO films with post deposition annealing.^[8, 9]

Second, replacing electrode material from currently commercialized TiN to Ru based material assists improving the electrical property of metal-insulator-metal capacitor. Since Ru has higher work function (~ 4.7 eV) than TiN (~ 4.2 eV), the Schottky barrier at interface of dielectric and metal differs according to the kind of metals. With semiconductors of n-type property as the dielectrics, the Schottky barrier is determined by the subtraction of electron affinity of dielectric from the work function of metal. Therefore, with Ru, the Schottky contact can have higher barrier height for ~ 0.5 eV than with TiN as electrode. Considering the even higher work function of RuO_2 (~ 5.0 eV), Schottky barrier could be increased for ~ 0.8 eV with RuO_2 than TiN, which will lower the leakage current density of capacitor to a certain required level. (table 1) ^[10-12]

Lastly, water and ozone is the most renowned oxidant to grow metal oxide film in chemical deposition method. Ozone which has higher oxidation potential than water for its unstable oxygen radical leads to low impurity contamination in the deposited film.^[1, 13-15] Since STO ALD mostly employs metal organic precursors as Sr and Ti precursor, incomplete reaction of chemisorbed precursor and oxidant causes carbon residues in the deposited films. Although -OH radical is the main oxidation species in water, which is different from ozone, the oxidation power of water can be compared with ozone. Since water is generally less reduced than ozone in equivalent

condition, using ozone as oxidant has larger possibility to remain less carbon impurity in the grown film.

These three constraints cause the deposition of STO with abnormal growth behavior and make difficult to handle the process.^[1-3] The main reason of non-ideal growth of STO films was initial excess incorporation of Sr element. In early study, when Sr(tmhd)₂ was adopted for Sr-precursor, the growth rate of Sr in initial stage showed little difference with the saturated stage. However, the deposition rate was too slow as 0.17 Å/cy to be adopted for mass production.^[8] Therefore, Sr(iPr₃Cp)₂ which has weaker bond between metal and ligands than Sr(tmhd)₂ was adopted to increase the growth rate.^[16] With this Sr-precursor with Cp-based ligand, the deposition rate of STO films increased over six times to 1.07 Å/cy. However, there was a severe initial Sr excess growth, which caused SrCO₃ formation. This was mainly due to the unwanted reaction of Sr-precursor and oxidized Ru substrate during violent ozone injection step in the deposition process.^[1] Ti(O-iPr)₂(tmhd)₂ was replaced to another more reactive Ti-precursor, Ti(Me₅Cp)(OM)₃ to countervail the violent reactivity of Sr-precursor. With Sr(iPr₃Cp)₂ and Ti(Me₅Cp)(OMe)₃ for Sr-precursor and Ti-precursor, respectively, STO could be grown on Ru substrate without SrCO₃ formation. However, the oxygen supply from Ru substrate not only to Ti-precursor, but also to Sr-precursor was still remaining and initial overgrowth of Sr element disturbs ideal self-

saturated growth which effects to the step coverage on complicated 3D structure.^[3]

In this study, ALD of STO films deposited with the novel Sr precursor, $[\text{Sr}(\text{demamp})(\text{tmhd})]_2$, and $\text{Ti}(\text{Me}_5\text{Cp})(\text{OMe})_3$ were investigated. The growth behavior and film properties including chemical, morphological and electrical properties were estimated to confirm the applicability of next generation DRAM capacitor.

Table 4.1 Work functions of major electrode materials ^[10-12]

materials	work function [eV]
TiN	4.2
Ru	4.7
RuO ₂	5.0
Ir	5.3
IrO ₂	4.2
Pt	5.7
ITO	4.5
SrRuO ₃	5.2

4.2. Experimental

SrO and STO films were deposited in a traveling wave-type ALD reactor (CN-1 Co, Plus-100) for a 4-inch-diameter single wafer. $[\text{Sr}(\text{demamp})(\text{tmhd})]_2$ (synthesized by Korea Research Institute of Chemical Technology)^[17] and $\text{Ti}(\text{Me}_5\text{Cp})(\text{OMe})_3$ (synthesized by Air Liquide) were employed as the Sr and Ti precursors, respectively. $\text{Sr}(\text{}^i\text{Pr}_3\text{Cp})_2$ (synthesized by Air Liquide) was also used as Sr precursor for depositing reference of SrO and STO films to compare the growth behavior of novel Sr precursor, $[\text{Sr}(\text{demamp})(\text{tmhd})]_2$. The schematic structure of $[\text{Sr}(\text{demamp})(\text{tmhd})]_2$ is shown in Fig. 1. The canisters of the $[\text{Sr}(\text{demamp})(\text{tmhd})]_2$, $\text{Sr}(\text{}^i\text{Pr}_3\text{Cp})_2$, and $\text{Ti}(\text{Me}_5\text{Cp})(\text{OMe})_3$ were heated to 50, 90, and 80 °C to maintain the appropriate vapor pressures of the precursors. Ar carrier gas was bubbled through the canisters to deliver the Sr and Ti precursors to the reaction chamber at a flow rate of 200 sccm, and the working pressure of the ALD reactor fluctuated near 0.7 Torr. O_3 at a concentration of 250 g/m³ was used as the oxygen source for the SrO and TiO_2 sub-layers.

The ALD sub-cycle process for TiO_2 consisted of precursor injection (3s), followed by Ar purge (5s), oxygen source injection (2s), and Ar purge (5s), which was confirmed to be consistent with the saturated ALD conditions.^[2] The ALD super-cycles for STO deposition consist of ALD sub-cycles of SrO and TiO_2 layers with different cycle ratios to vary the cation

composition. The T_g was set at 370°C, and bare Si wafers, Ru(30 nm)/Ta₂O₅(8 nm)/SiO₂(100 nm)/Si wafers, or Pt(50nm)/Ti(20nm)/SiO₂(200 nm)/Si wafers were used as substrates. Since the single STO layer growth at this T_g still did not induce in-situ crystallization, the so-called two-step process was employed in this work. Crystallization-annealing of the thin seed STO layer was performed in an RTA system at 650 °C for 2 minutes in an N₂ atmosphere (purity >99.99%).

The layer density and cation composition of STO films were confirmed by X-ray fluorescent spectroscopy (XRF, Themoscintific, ARL Quant'X). The physical thickness of the STO films was measured using an ellipsometer. The impurity concentration in the films, including carbon and nitrogen, and the depth profile were examined by Auger electron spectroscopy (AES, Perkin-Elmer, PHI 660). The chemical binding states of the films were determined by X-ray photoelectron spectroscopy (XPS, ThermoVG, SIGMA PROBE). The crystal structure of the film was investigated by glancing angle mode X-ray diffraction using a Cu K α X-ray source (GAXRD, PANalytical, X'Pert Pro). The incidence angle, scan step size, and time per step during the GAXRD measurement were 2°, 0.02°, and 1 sec, respectively. The planar-structured metal-insulator-metal capacitors were fabricated by depositing an 60-nm-thick Pt layer on 20-nm-thick RuO₂ layer as a top electrode by sputter through a shadow mask (with a 0.3-mm hole diameter). The electrical properties, including the capacitance and leakage current, were measured using an

HP4194A impedance analyzer at 10 kHz and an HP4140 picoammeter, respectively.

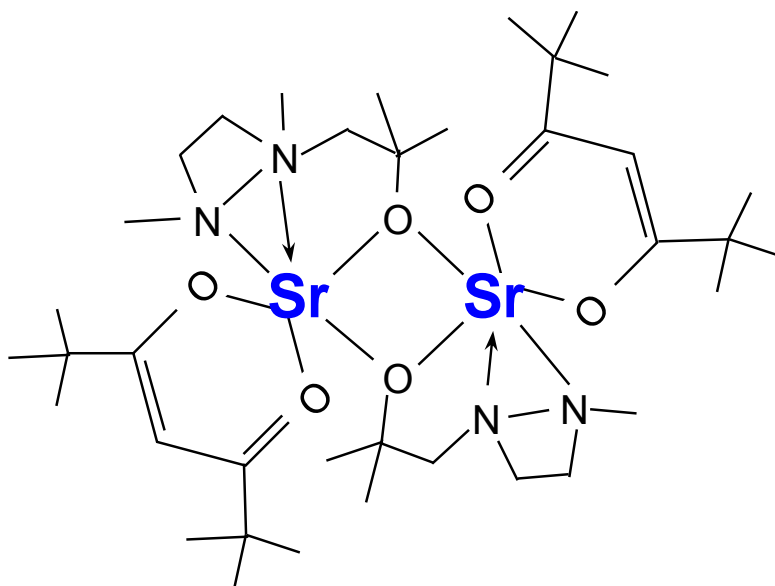


Figure 4.1 The schematic chemical structure of $[\text{Sr}(\text{demamp})(\text{tmhd})]_2$ precursor

4.3. Results and Discussions

The ALD saturation behavior of SrO film growth was firstly confirmed with $[\text{Sr}(\text{demamp})(\text{tmhd})]_2$ and O_3 as Sr-precursor and reactant, respectively. Figure 2a – c show the variation of deposition amount as a function of process step time on Ru, Si, and Pt substrate. The process time of precursor injection – Ar purge – oxidant injection – Ar purge were set to 10 s -10 s – 7 s – 10 s, which is confirmed in ALD saturation time, without the tested step. In every substrate, 3 s, 5 s, and 5 s were enough to obtain the saturated behavior for precursor purge, oxidant injection, oxidant purge time equivalently. Only 5 s of precursor supplying time were necessary on Si substrate to reach the saturated deposition level, while over 7 s were required on Ru and on Pt substrate. Since the deposition amounts of saturated levels were different in different substrates, which is indicated in Figure 2d, necessary dosage of Sr-precursor introduced to the process chamber is smaller on Si substrate and shorter precursor injection time of 5s was plenteous.

As it is mentioned in introduction section above, initial excess Sr incorporation causes SrCO_3 formation in the film and not only the composition is difficult to control in STO deposition, but the film property is also unsatisfactory. Accordingly, the growth behavior of SrO films deposited with $[\text{Sr}(\text{demamp})(\text{tmhd})]_2$ was examined. Figure 3 shows the comparison of growth behavior of SrO films deposited with $\text{Sr}(\text{iPr}_3\text{Cp})_2$ and

[Sr(demamp)(tmhd)]₂ precursors on various substrates. Initial excess growth was seen not only on Ru substrate, but also on Pt and Si substrate with Sr(iPr₃Cp)₂ precursor and O₃. Although the Pt substrate did not oxidize by ozone during the process, oxygen ions in oxidized Sr-precursor which is chemisorbed to the metal substrate could be extorted by the sequentially exposed Sr-precursor. On metal substrate such as platinum substrate, electron donation effect from substrate to precursor and oxygen ion would assist the oxygen supply to the Sr-precursor before next oxidant injection step. Since electrons are more difficult to be gotten out from the Si substrate than Ru or Pt substrate, the initial abnormal growth behavior was retarded in SrO deposition on Si substrate. However, since the reactivity of [Sr(demamp)(tmhd)]₂ is more appropriate than the violent Sr(iPr₃Cp)₂, the excess deposition in initial stage of SrO deposition was negligible with the novel precursor. The growth rate was still in equivalent tendency that Ru substrate gave the fastest growth rate because of the reduction of RuO₂ from surface and electron donation effect. In addition, the deposition amount on Si substrate was the smallest since the oxidized Si surface hardly passed the electrons. In the point of view that SrCO₃ was formed in the film when the growth behavior included initial rapid growth in previous studies, retarded carbonate formation would be anticipated with the freshly set SrO process.^[1] As it is shown in figure 4a left panel, carbon contamination was largely decreased with [Sr(demamp)(tmhd)]₂ as compared with Sr(iPr₃Cp)₂. In

addition, nitrogen element, which is contained in demamp ligand, was under detecting level of AES and XPS in SrO films on every substrate. (Figure 4a right panel, 4b) Moreover, depth profile of SrO films on every substrate showed very uniform composition of Sr, Ti, and O as indicated in figure 5. However, in spite of extremely low carbon contamination in SrO films, the deposited films had SrCO₃ nature instead of SrO nature, which is confirmed by XPS in figure 6. As it is shown in figure 6a, only C-C bonding and SrCO₃ bonding was observed instead of SrO peak which should be seen where the blue line points. Moreover, there was not any sign of SrO binding energy near O 1s and Sr 3d energy region. This corresponds to every substrate employed in this experiment even on Si substrate which is expected to have the least substrate effect to the film growth. As SrCO₃ is more stable than SrO in thermodynamics by comparing the Gibbs free energy at the investigated temperature, carbon permeated to the films when the sample is exposed to air. As the thicknesses of SrO films were below 5nm, the whole films altered to carbonate and SrCO₃ peaks were observed even after the surface etching by Ar plasma. (data not shown)

Secondly, STO was deposited with newly developed SrO ALD process with [Sr(demamp)(tmhd)]₂ and O₃ and TiO₂ ALD which is already prepared in the previous study with Ti(Me₅Cp)(OMe)₃ and O₃.^[3] The subcycle ratio of TiO₂ : SrO was changed to find the process condition of stoichiometric STO film deposition. As the subcycle ratio of Sr/(Sr+Ti) increased from 40 % to 67 %,

the cation composition $\text{Sr}/(\text{Sr}+\text{Ti})$ of STO film increased from 48% to 88% on Ru substrate. On Pt substrate, the cation composition was higher for 2 ~ 4 % than on Ru substrate and on Si substrate, higher for 4 ~ 6 % than on Pt substrate. For 2 : 3, TiO_2 : SrO subcycle ratio, stoichiometric STO film could be obtained on Ru. (Figure 7a) As the supercycle of STO which is consisted of TiO_2 , SrO, TiO_2 , SrO, and SrO was increased, the cation composition of STO films maintained in stoichiometric composition, while the exactly equivalent experimental result with $\text{Sr}(\text{iPr}_3\text{Cp})_2$ showed decrease of Sr concentration in an initial few supercycles. This indicate that absence of abnormal growth behavior induced better controllability of composition of STO films in different thickness. Moreover, the films would have more equivalent properties separately with the deposition cycle.

Figure 8 shows the variation of deposition amount in layer density and in thickness as a function of supercycle. In figure 8a, on every substrate, initial anomalous behavior was hardly observed except for the retardation of Ti incorporation on Si substrate. However, the growth rate of Sr element increased linearly on three substrates. Figure 8b shows the deposition rate of STO films with $\text{Sr}(\text{iPr}_3\text{Cp})_2$ and $[\text{Sr}(\text{demamp})(\text{tmhd})]_2$ precursors. Although the growth rate of STO film with the new precursor decreased to 0.5 Å/cy, it is still in an acceptable level.

Like the SrO films mentioned above, the chemical properties of STO films were also analyzed by XPS and AES in figure 9. Contrary to the SrO films,

STO films showed not only SrCO₃ peaks but also STO and SrO peaks. After surface etching by Ar plasma, every SrCO₃ peak was disappeared, remaining the SrO and STO peak obviously. Nitrogen was not detected in STO film as expected. Moreover, the carbon impurity in film was decreased to under 1%, which is improved than the previous report.^[3]

To have a high dielectric constant of STO films for capacitor, STO should be crystallized well. As it is mentioned in the introduction section, post deposition annealing after STO deposition causes nanocracks which are operated as leakage paths and worsen insulating property. Therefore, two-step process which rapid thermal annealing is interposed between was employed for superior electrical property. By annealing STO seed layer before main layer deposition, the whole STO film was well in-situ crystallized into perovskite structure without any additional annealing process which is indicated in figure 10a. Moreover, to compare the density of in-situ crystallized STO film and conventionally annealed ex-situ crystallized STO films, XRR analysis was looked into in figure 10b. The critical angle of XRR plot, which implies the density of the uppermost layer, of in-situ crystallized sample was as high as that of ex-situ crystallized sample. Graphs of both of the crystallized samples showed larger density than the as-deposited amorphous films. Surface morphology was investigated by SEM in figure 11. While the as-deposited STO film shows porous surface, ex-situ and in-situ STO film have very smooth surface with dense grains. This correlates well

with the XRR analysis. In addition, the STO films deposited with $[\text{Sr}(\text{demamp})(\text{tmhd})]_2$ and O_3 have more conformal surface whereas the layer had many void and nanocracks which was specifically studied elsewhere.^[18] The reason of improvement of surface morphology could be found by thinking figure 8 again. The point that not only the growth rate is slower, but also the step time increased with the new precursor than $\text{Sr}(\text{iPr}_3\text{Cp})_2$ indicate that the lately set STO process gives more time to atoms to find the equilibrium position and remains less stress after deposition. Therefore, less strain of STO film could be stayed in the film without any defect formation such as cracks or voids.

Electrical property of (top) RuO_2 -STO-Ru (bottom), metal-insulator-metal capacitor with planar structure was indicated in Figure 12. STO was deposited with five thicknesses to estimate the bulk dielectric constant. From the inverse slope of figure 12a, the calculated dielectric constant of STO films which exclude the interfacial electrical property influence was 143.^[2] Figure 12b shows the overall summary of capacitance and leakage current property. In consideration that the required leakage current density of DRAM capacitor specification is under $1 \times 10^{-7} \text{A/cm}^2$, the ultimate equivalent oxide thickness (t_{ox}) was 0.46 nm with leakage current as low as $9 \times 10^{-8} \text{A/cm}^2$.

Figure 13a shows the cross-section of TEM image of STO films deposited on SiO_2 hole structure. The three dimensional hole has opening diameter of ~ 100 nm and depth of $\sim 1 \mu\text{m}$ with aspect ratio $\sim 10:1$. STO was deposited for

80 supercycles and the deposited thickness was ~ 0.95 nm around the top of the hole. STO was also deposited in the bottom of the hole for ~ 0.80 nm. The composition of STO films deposited on flat SiO₂ was equivalent to that deposited on hole structure for 44 at% of Sr/(Sr+Ti). As it is seen in figure 13b, the cation compositions of STO film which were measured by EDS have small variation with the level analyzed by XRF irrespective of the position with different depth. The thickness step coverage and compositional uniformity were both $\sim 85\%$, which indicate the deposition process contains well self-limited growth behavior.

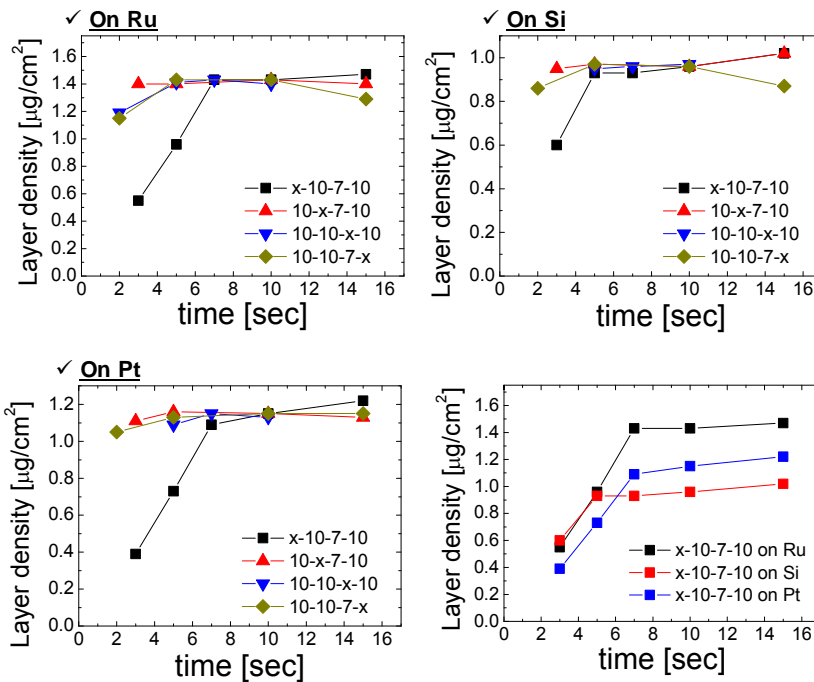


Figure 4.2 Variation of Sr layer densities of SrO films as a function of feeding times of precursor injection, precursor purge, oxidant injection, and oxidant purge time on (a) Ru, (b) Si, and (c) Pt substrate. (d) Summary of variation of Sr layer density as a function of precursor injection time on Ru, Si, and Pt substrate.

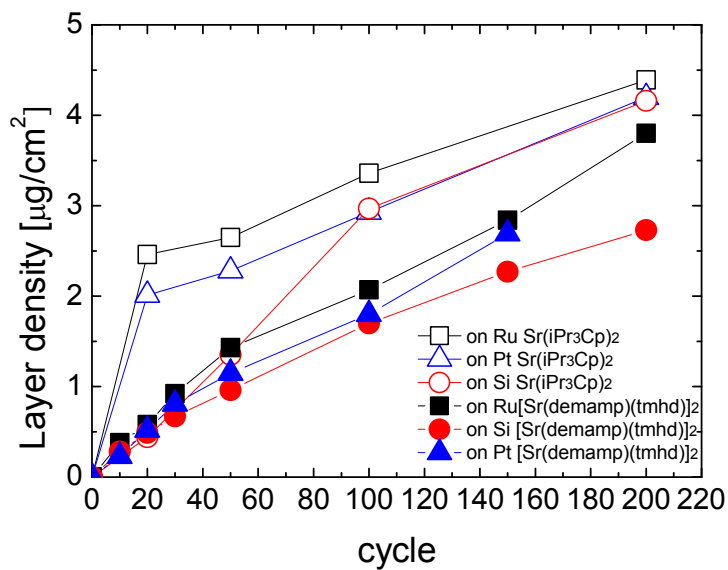


Figure 4.3 The comparison of growth behavior of SrO films deposited with Sr(iPr₃Cp)₂ and [Sr(demamp)(tmhd)]₂ on various substrates

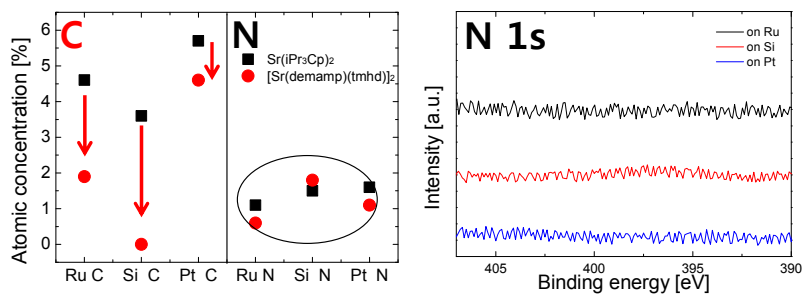


Figure 4.4 (a)Atomic concentration of C and N in SrO films by AES and (b) XP spectra of N 1s in SrO film

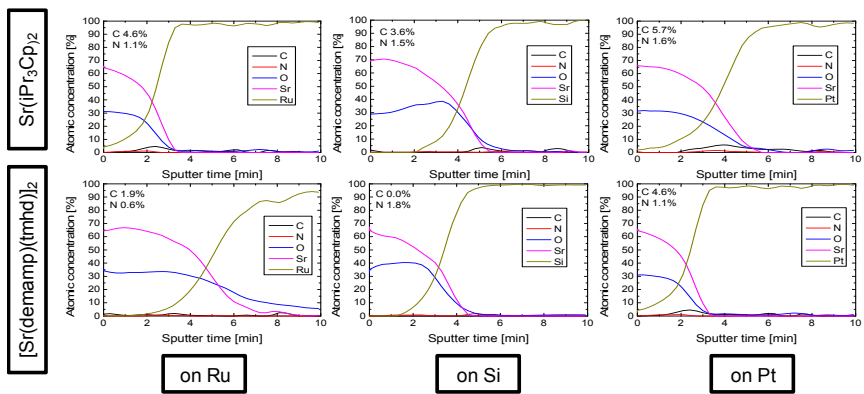


Figure 4.5 AES depth profile of SrO films deposited by $\text{Sr}(\text{iPr}_3\text{Cp})_2$ and $[\text{Sr}(\text{demamp})(\text{tmhd})_2]$ on Ru, Si, and Pt substrate.

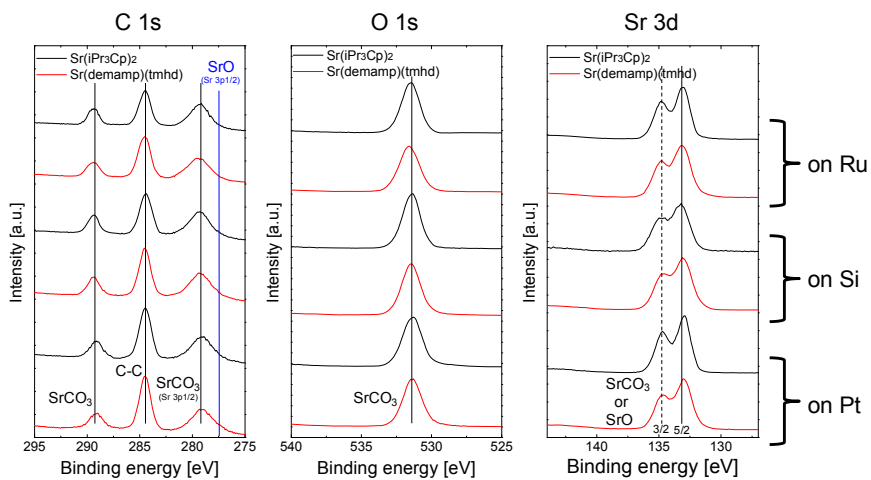


Figure 4.6 XPS spectra of (a) C 1s, (b) O 1s, and (c) Sr 3d in SrO films deposited by $\text{Sr}(\text{iPr}_3\text{Cp})_2$ and $[\text{Sr}(\text{demamp})(\text{tmhd})]_2$ on Ru, Si, and Pt substrate.

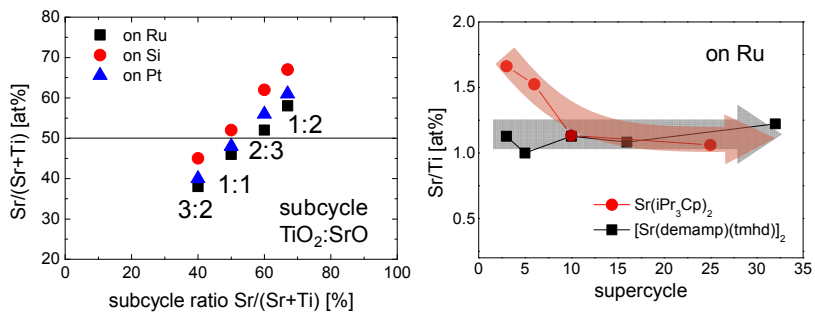


Figure 4.7 Variation of cation composition as a function of (a) subcycle ratio and (b) supercycle (TiO₂ : SrO = 2 : 3)

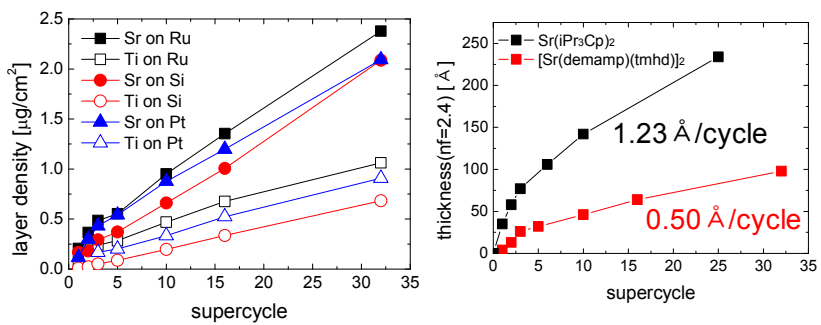


Figure 4.8 (a) Variation of layer density of Sr and Ti element and (b) thickness of STO films as a function of supercycle

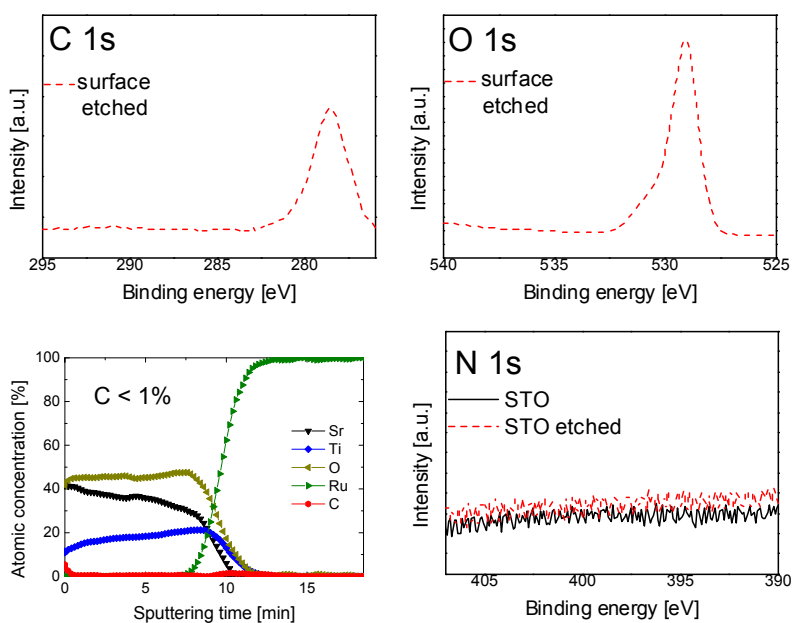


Figure 4.9 XPS spectra of (a) C 1s, (b) O 1s, and (d) N 1s of STO films and (c) AES depth profile of STO films

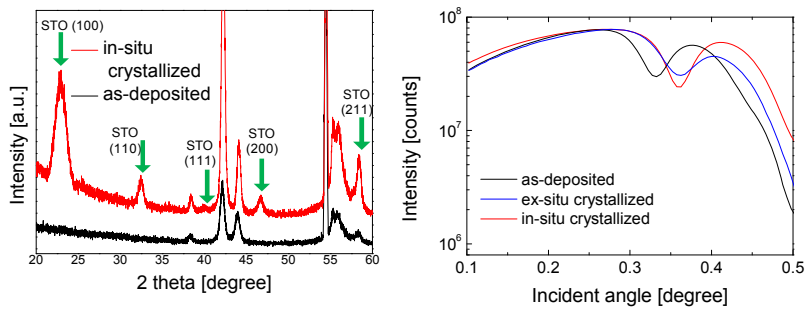


Figure 4.10 (a) Glancing angle XRD of STO films (b) XRR of as-deposited, ex-situ crystallized, and in-situ crystallized STO films

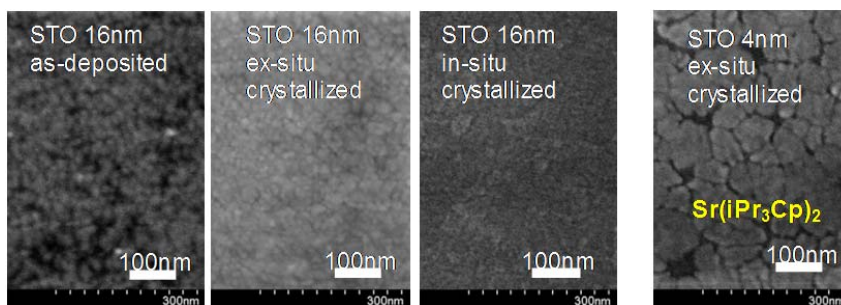


Figure 4.11 SEM images of (a) as-deposited, (b) ex-situ crystallized, (c) in-situ crystallized STO films deposited with [Sr(demamp)(tmhd)]₂, and (d) ex-situ crystallized STO films deposited with Sr(iPr₃Cp)₂.

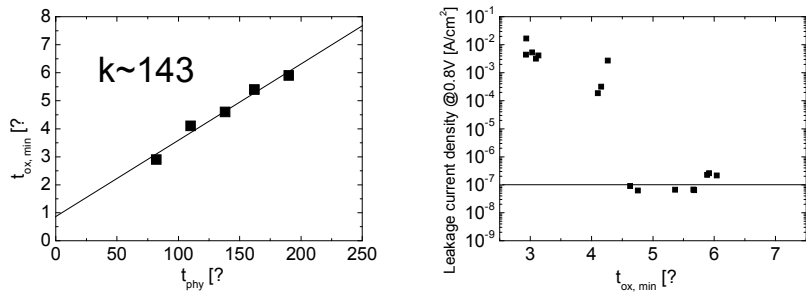


Figure 4.12 Electrical properties of STO films. (a) t_{ox} vs. t_{phy} and (b) J vs. t_{ox}

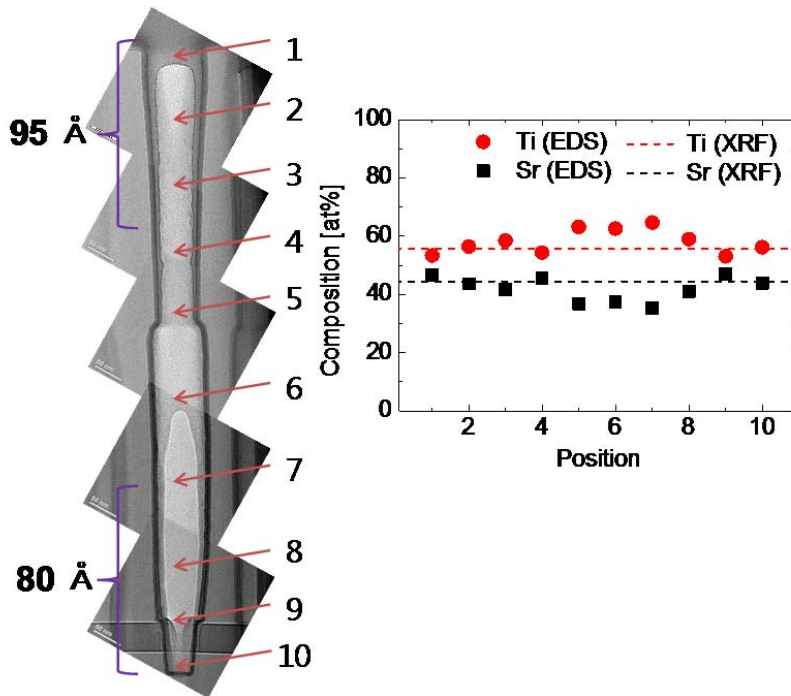


Figure 4.13 (a) Cross-section TEM image of STO films deposited on SiO₂ hole structure (opening diameter ~100 nm, depth ~1μm, aspect ratio~10:1) and (b) the variation of cation composition of STO films according to the hole position measured by EDS and XRF

4.4. Summary

In this study, SrO films were deposited with $[\text{Sr}(\text{demamp})(\text{tmhd})]_2$ and O_3 as Sr-precursor and oxidant, respectively, and STO films were grown by freshly set SrO process and TiO_2 process with $\text{Ti}(\text{Me}_5\text{Cp})(\text{OMe})_3$ and O_3 , as Ti-precursor and oxidant, respectively. Both SrO and STO film deposition did not show any abnormal initial growth which involves unwanted SrCO_3 formation. Sr and Ti element increased linearly as the deposition cycle increased and the film property was improved than before. Carbon contamination was decreased and more smooth surface could be obtained with fine grains. The dense STO films which are in-situ crystallized to perovskite structure showed bulk dielectric constant of 143. The optimized t_{ox} was 0.46 nm with acceptable leakage current density. ($9 \times 10^{-8} \text{ A/cm}^2$). With newly set STO deposition process with more ideal behavior, STO film showed conformal step coverage in hole structure of aspect ratio of 10:1.

4.5. Bibliography

1. S. W. Lee, J. H. Han, S. Han, W. Lee, J. H. Jang, M. Seo, S. K. Kim, C. Dussarrat, J. Gatineau, Y.-S. Min and C. S. Hwang, *Chem. Mater.*, 2011, 23, 2227.
2. W. Lee, J. H. Han, S. W. Lee, S. Han, W. J. Jeon, and C. S. Hwang, *J. Mater. Chem.*, 2012, 22, 15037.
3. W. Lee, J. H. Han, W. Jeon, Y. W. Yoo, S. W. Lee, S. K. Kim, C.-H. Ko, C. Lanslaot-Matras, C. S. Hwang, *Chem. Mater.*, 2013, 25, 953.
4. M. A. Pawlak, B. Kaczer, M.-S. Kim, M. Popovici, K. Tomida, J. Swerts, K. Opsomer, W. Polspoel, P. Favia, C. Vrancken, C. Demeurisse, W.-C. Wang, V. V. Afanas'ev, W. Vandervorst, H. Bender, I. Debusschere, L. Altimime, and J. A. Kittl, *Appl. Phys. Lett.*, 2010, 97, 162906.
5. S. K. Kim, S. W. Lee, J. H. Han, B. Lee, S. Han, and C. S. Hwang, *Adv. Funct. Mater.*, 2010, 20, 2989.
6. M. A. Pawlak, B. Kaczer, M.-S. Kim, M. Popovici, J. Swerts, W.-C. Wang, K. Opsomer, P. Favia, K. Tomida, A. Belmonte, B. Govoreanu, C. Vrancken, C. Demeurisse, H. Bender, V. V. Afanas'ev, I. Debusschere, L. Altimime, and J. A. Kittl, *Appl. Phys. Lett.*, 2011, 98, 182902.

7. M. A. Pawlak, J. Swerts, M. Popovici, B. Kaczer, M.-S. Kim, W.-C. Wang, K. Tomida, B. Govoreanu, J. Delmotte, V. V. Afanas'ev, M. Schaekers, W. Vandervorst, and J. A. Kittl, *Appl. Phys. Lett.* 2012, 101, 042901.
8. S. W. Lee, O. S. Kwon, J. H. Han, and C. S. Hwang, *Appl. Phys. Lett.*, 2008, 92, 222903.
9. S. W. Lee, J. H. Han, O. S. Kwon, and C. S. Hwang, *J. Electrochem. Soc.*, 2008, 155, G253.
10. S. K. Kim, S. Han, W. Jeon, J. H. Yoon, J. H. Han, W. Lee, and C. S. Hwang, *ACS Appl. Mater. Interfaces*, 2012, 4, 4726.
11. J. H. Han, S. Han, W. Lee, S. W. Lee, S. K. Kim, J. Gatineau, C. Dussarrat, C. S. Hwang, *Appl. Phys. Lett.*, 2011, 99, 022901.
12. H. B. Michaelson, *J. Appl. Phys.*, 1977, 48, 4729
13. M. Shirazi and S. D. Elliott, *Chem. Mater.*, 2013, 25, 878.
14. X. Liu, S. Ramanathan, A. Londergan, A. Srivastava, E. Lee, T. E. Seidel, J. T. Barton, D. Pang, and R. G. Gordon, *J. Electrochem. Soc.*, 2005, 152, G213.
15. S. Y. Lee, H. K. Kim, J. H. Lee, I.-H. Tu, J.-H. Lee, and C. S. Hwang, *J. Mater. Chem. C*, 2014, 2, 2558.

16. T. P. Holme and F. B. Prinz, *J. Phys. Chem. A*, 2007, 111, 8147.
17. S. M. George, B. K. Park, C. G. Kim, and T.-M. Chung, *Eur. J. Inorg. Chem.*, 2014, 2002.
18. submission preparation.

5. Conclusion

STO films were grown by ALD with various kinds of Sr and Ti precursors: $\text{Sr}(\text{}^i\text{Pr}_3\text{Cp})_2$, $[\text{Sr}(\text{demamp})(\text{tmhd})]_2$, $\text{Ti}(\text{O-}^i\text{Pr})_2(\text{tmhd})_2$, and $\text{Ti}(\text{Me}_5\text{Cp})(\text{OMe})_3$. The growth behavior of STO films with each Sr and Ti precursors set was investigated and film properties including electrical properties of fabricated metal-insulator-metal capacitors were evaluated in various points of view.

In deposition of multicomponent films, many hindrances were emerged, which caused abnormal ALD behavior in film growth. This unusual comportment was generated extremely by high temperature, unstable substrate, and reactant sources. Nevertheless, several ways were suggested to overcome the non-ideal growth behavior of STO films. Firstly, with $\text{Sr}(\text{}^i\text{Pr}_3\text{Cp})_2$ and $\text{Ti}(\text{O-}^i\text{Pr})_2(\text{tmhd})_2$, barrier layer such as Al_2O_3 layer was interposed between STO layer and Ru substrate. Since Al_2O_3 hardly diffused oxygen ion from Ru substrate to Sr-precursor, unwanted reaction between them could be suppressed and linear growth behaviors of both Sr and Ti element were achieved, although the deposition temperature was as high as 370oC and O_3 was included in the process as oxidant. Good crystallinity of STO films adopting crystallized seed layer was confirmed with very low impurity concentration in the films.

However, since the Al_2O_3 layer degraded the electrical properties of MIM capacitor, another method to skip the barrier layer deposition was necessary.

Therefore, $\text{Ti}(\text{O}^i\text{Pr})_2(\text{tmhd})_2$ was replaced by $\text{Ti}(\text{Me}_5\text{Cp})(\text{OMe})_3$ which has larger reactivity. With this Cp-based Ti-precursor, violent reaction between $\text{Sr}(\text{Pr}_3\text{Cp})_2$ and Ru substrate was countervailed and linearity of growth of Sr element increased to a certain degree. With Cp-based precursors, SrCO_3 formation was successfully prevented and equivalent oxide thickness of 0.39 nm was obtained with acceptable leakage current density, $9 \times 10^{-8} \text{ A/cm}^2$. Also, by controlling the cooling rate after crystallization annealing of STO seed layer, the microdefects was reduced and the bulk electrical property was improved.

Nonetheless, this STO deposition process still had CVD-like growth behavior and was anticipated to have insufficient step coverage property. Consequently, novel Sr-precursor, $[\text{Sr}(\text{demamp})(\text{tmhd})]_2$ was employed as Sr-precursor to resolve this issue. This recently developed Sr-precursor with appropriate reactivity showed deposition process with not only ideal growth behavior with O_3 on Ru substrate at 370°C , but also proper saturated deposition rate. In addition, the surface of STO film was very smooth and uniform grains were obtained. Promising electrical property including bulk dielectric constant of ~ 143 was also achieved. With exceedingly ideal ALD process, conformal STO film could be deposited with good compositional uniformity on three dimensional hole structure of aspect ratio 10:1.

In conclusion, various ways were suggested to overcome the non-ideal behavior of ALD STO films. The growth behaviors were investigated and the film properties including chemical nature, crystallinity, step coverage, surface morphology, electrical property, etc., were found to be advanced. This thesis introduces possible pathways for the next generation DRAM capacitor by presenting the systematic approach of overcoming the severe non-ideality of ALD STO films. Even though STO is still far from the adoption as dielectric of DRAM capacitor, the results in this thesis throw light on this field by showing promising properties of STO ALD.

List of publications

1. Refereed Journal Articles (SCI)

1.1 Domestic

1.2. International

1. Seol Choi, Byung Joon Choi, Taeyong Eom, Jae Hyuck Jang, Woongkyu Lee, and Cheol Seong Hwang, "Growth and Phase Separation Behavior in Ge-Doped Sb-Te Thin Films Deposited by Combined Plasma-Enhanced Chemical Vapor and Atomic Layer Depositions", J. Phys. Chem. C, 114, 17899 (2010)
2. Sang Woon Lee, Jeong Hwan Han, Seong Keun Kim, Sora Han, Woongkyu Lee, and Cheol Seong Hwang, "Role of Interfacial Reaction in Atomic Layer Deposition of TiO₂ Thin Films Using Ti(O-iPr)₂(tmhd)₂ on Ru or RuO₂ Substrates", Chem. Mater. 23, 976-983 (2011)
3. Sang Woon Lee, Jeong Hwan Han, Sora Han, Woongkyu Lee, Jae Hyuck Jang, Minha Seo, Seong Keun Kim, C. Dussarrat, J. Gatineau, Yo-Sep Min, and Cheol Seong Hwang, "Atomic Layer Deposition of SrTiO₃ Thin Films with Highly Enhanced Growth Rate for Ultrahigh Density Capacitors", Chem. Mater. 23, 2227 (2011)

4. Boris Hudec, Kristína Hušková, Aivar Tarre, Jeong Hwan Han, Sora Han, Alica Rosová, **Woongkyu Lee**, Aarne Kasikov, Seul Ji Song, Jaan Aarik, Cheol Seong Hwang, Karol Fröhlich, "Electrical properties of TiO₂-based MIM capacitors deposited by TiCl₄ and TTIP based atomic layer deposition processes", *Microelectron. Eng.* (2011)
5. Seong Keun Kim, Sora Han, Jeong Hwan Han, **Woongkyu Lee**, and Cheol Seong Hwang, "Atomic layer deposition of TiO₂ and Al-doped TiO₂ films on Ir substrates for ultralow leakage currents", *Phys. Status Solidi RRL* 5, No. 8, 262-264 (2011)
6. Jeong Hwan Han, Sora Han, **Woongkyu Lee**, Sang Woon Lee, Seong Keun Kim, Julien Gatineau, Christian Dussarrat, and Cheol Seong Hwang, "Improvement in the leakage current characteristic of metal-insulator-metal capacitor by adopting RuO₂ film as bottom electrode", *Appl. Phys. Lett.* 99, 022901 (2011)
7. Minha Seo, Sang Ho Rha, Seong Keun Kim, Jeong Hwan Han, **Woongkyu Lee**, Sora Han, and Cheol Seong Hwang, "The mechanism for the suppression of leakage current in high dielectric TiO₂ thin films by adopting ultra-thin HfO₂ films for memory application", *J. Appl. Phys.* 110, 024105 (2011)
8. Jeong Hwan Han, Sang Woon Lee, Seong Keun Kim, Sora Han, **Woongkyu Lee**, and Cheol Seong Hwang, "Study on Initial Growth Behavior of RuO₂ Film Grown by Pulsed Chemical Vapor Deposition: Effects of Substrate and Reactant Feeding Time", *Chem. Mater.* 24, 1407 (2012)

9. Taeyong Eom, Seol Choi, Byung Joon Choi, Min Hwan Lee, Taehong Gwon, Sang Ho Rha, **Woongkyu Lee**, Moo-Sung Kim, Manchao Xiao, Iain Buchanan, Deok-Yong Cho, and Cheol Seong Hwang, "Conformal Formation of $(\text{GeTe}_{2(1-x)}\text{Sb}_2\text{Te}_3)_x$ Layers by Atomic Layer Deposition for Nanoscale Phase Change Memories", Chem. Mater. 24 (11), 2099 (2012)
10. **Woongkyu Lee**, Jeong Hwan Han, Sang Woon Lee, Sora Han, Woo Jin Jeon and Cheol Seong Hwang, "Controlling the initial growth behavior of SrTiO_3 films by interposing Al_2O_3 layers between the film and the Ru substrate", J. Mater. Chem. 22, 15037 (2012)
11. Seong Keun Kim, Sora Han, Woojin Jeon, Jung Ho Yoon, Jeong Hwan Han, **Woongkyu Lee**, and Cheol Seong Hwang, "Impact of Bimetal Electrodes on Dielectric Properties of TiO_2 and Al-Doped TiO_2 Films", ACS Appl. Mater. Interfaces 4, 4726 (2012)
12. Jeong Hwan Han, **Woongkyu Lee**, Woojin Jeon, Sang Woon Lee, and Cheol Seong Hwang, Changhee Ko and Julien Gatineau, "Growth of Conductive SrRuO_3 Films by Combining Atomic Layer Deposited SrO and Chemical Vapor Deposited RuO_2 Layers", Chem. Mater., 24(24), 4686-4692, (2012)
13. **Woongkyu Lee**, Jeong Hwan Han, Woojin Jeon, Yeon Woo Yoo, Sang Woon Lee, Seong Keun Kim, Chang-Hee Ko, Clement Lansalot-Matras, and Cheol Seong Hwang, "Atomic Layer Deposition of SrTiO_3 Films with Cyclopentadienyl-Based Precursors for Metal-Insulator-Metal Capacitors", Chem. Mater. 25, 953-961 (2013)

14. Min Hyuk Park, Han Joon Kim, Yu Jin Kim, **Woongkyu Lee**, Hyo Kyeom Kim, and Cheol Seong Hwang, "Effect of forming gas annealing on the ferroelectric properties of $\text{Hf}_{0.5}\text{Zr}_{0.5}\text{O}_2$ thin films with and without Pt electrodes", Appl. Phys. Lett. 102, 112914 (2013)
15. Sang Woon Lee, Byung Joon Choi, Taeyong Eom, Jeong Hwan Han, Seong Keun Kim, Seul Ji Song, **Woongkyu Lee**, Cheol Seong Hwang, "Influences of metal, non-metal precursors, and substrates on atomic layer deposition processes for the growth of selected functional electronic materials", Coord. Chem. Rev., 257, 3154-3176 (2013)
16. Min Hyuk Park, Han Joon Kim, Yu Jin Kim, **Woongkyu Lee**, Taehwan Moon, and Cheol Seong Hwang, "Evolution of phases and ferroelectric properties of thin $\text{Hf}_{0.5}\text{Zr}_{0.5}\text{O}_2$ films according to the thickness and annealing temperature", Appl. Phys. Lett. 102, 242905 (2013)
17. Katsuhisa Murakami, Mathias Rommel, Boris Hudec, Alica Rosová, Kristina Hušeková, Edmund Dobročka, Raul Rammula, Aarne Kasikov, Jeong Hwan Han, **Woongkyu Lee**, Seul Ji Song, Albena Paskaleva, Anton J. Bauer, Lothar Frey, Karol Fröhlich, Jaan Aarik, and Cheol Seong Hwang, "Nanoscale Characterization of TiO_2 Films Grown by Atomic Layer Deposition on RuO_2 Electrodes", ACS Appl. Mater. Interfaces 6, 2486 (2014)

18. Woojin Jeon, Sang Ho Rha, **Woongkyu Lee**, Yeon Woo Yoo, Cheol Hyun An, Kwang Hwan Jung, Seong Keun Kim, and Cheol Seong Hwang, "Controlling the Al-Doping Profile and Accompanying Electrical Properties of Rutile-Phased TiO₂ Thin Films", ACS Appl. Mater. Interfaces 6, 7910-7917 (2014)

2. CONFERENCES

2.1 Domestic

1. Taeyong Eom, Seol Choi, Byung Joon Choi, Sang Ho Rha, **Woongkyu Lee**, Cheol Seong Hwang, Moo-Sung Kim, Manchao Xiao "Atomic Layer Deposition of (GeTe₂)_x(Sb₂Te₃)_y films for phase change memories"(Oral), 제 18회 한국 반도체 학술대회, 해비치 호텔 & 리조트 제주, February 16-18 (2011) - oral
2. Jeong Hwan Han, **Woongkyu Lee**, Sora Han, Julien Gatineau, and Cheol Seong Hwang, "Atomic layer/chemical vapor deposited SrRuO₃ thin films using RuO₄ and Sr(iPr₃Cp)₂ precursors for next generation DRAM capacitor electrode", 제 18회 한국 반도체 학술대회, 해비치 호텔 & 리조트 제주, February 16-18 (2011) - oral

3. **Woongkyu Lee**, Jeong Hwan Han, Sora Han, Sang Woon Lee and Cheol Seong Hwang, "Controlling initial growth of ALD-SrTiO₃ films with interposed ALD-Al₂O₃ layers", 제 18회 한국 반도체 학술대회, 해비치 호텔 & 리조트 제주, February 16-18 (2011) -poster
4. Taeyong Eom, Seol Choi, Byung Joon Choi, Min Hwan Lee, Taehong Gwon, Sang Ho Rha, **Woongkyu Lee**, Moo-Sung Kim, Manchao Xiao, Cheol Seong Hwang, "Atomic layer deposition of (GeTe₂)_{1-x}(Sb₂Te₃)_x film for phase change memory", 제19회 반도체학술대회, 고려대학교 2/15~2/17, Feb 17th (2012)-oral
5. **Woongkyu Lee**, Jeong Hwan Han, Woojin Jeon and Cheol Seong Hwang, "Atomic Layer Deposition of SrTiO₃ Films with Cp-based Precursors", 제19회 반도체학술대회, 고려대학교 2/15~2/17, Feb 17th (2012)-oral
6. Jeong Hwan Han, **Woongkyu Lee**, Woojin Jeon, and Cheol Seong Hwang, "Growth of conductive SrRuO_x films by combined CVD/ALD process", 제19회 반도체학술대회, 고려대학교 2/15~2/17, Feb 17th (2012)-poster
7. Woojin Jeon, **Woongkyu Lee**, Yeon Woo Yoo, and Cheol Seong Hwang, "EOT Scaling under 4.0Å with TiO₂ and Al-doped TiO₂ Film", Feb. 4-6, 성우리조트, 제 20회 한국 반도체 학술대회 (2013) – oral
8. Min Hyuk Park, Han Joon Kim, Yu Jin Kim, Hyo Kyeom Kim, **Woongkyu Lee**, Il-Hyuk Yu, and Cheol Seong Hwang, "The effects of grain size on the electrical properties of ferroelectric Hf_{1-x}Zr_xO₂ thin films", Feb. 4-6, 성우리조트, 제 20회 한국 반도체 학술대회 (2013) – oral

9. Yeon Woo Yoo, Woojin Jeon, **Woongkyu Lee** and Cheol Seong Hwang, "Study on atomic layer deposition behavior of TiO₂ films on SiO₂ and RuO₂ substrates with different growth temperatures", Feb. 4-6, 성우리조트, 제 20회 한국 반도체 학술대회 (2013) –poster
10. Min Hyuk Park, Han Joon Kim, Yu Jin Kim, **Woongkyu Lee**, Taehwan Moon, and Cheol Seong Hwang, "Evolution of Phases and Ferroelectric Properties of Thin Hf_{0.5}Zr_{0.5}O₂ Films According to the Thickness and Annealing Temperature" Feb. 24-26, 한양대학교, 제 21 한국 반도체 학술대회 (2014) - oral
11. Woojin Jeon, **Woongkyu Lee**, Yeon Woo Yoo, Cheol Hyun An, and Cheol Seong Hwang, "Evaluating the Change in Electrical Conduction Mechanism and Dielectric Properties of TiO₂ Thin-Film by Al Doping", Feb. 24-26, 한양대학교, 제 21 한국 반도체 학술대회 (2014) – oral
12. Cheol Hyun An, Woojin Jeon, **Woongkyu Lee**, Yeon Woo Yoo, and Cheol Seong Hwang, "Improving Conformality of SrRuO₃ Film Grown by Combined ALD SrO and CVD RuO₂ or Ru Layers", Feb. 24-26, 한양대학교, 제 21 한국 반도체 학술대회 (2014) – poster
13. **Woongkyu Lee**, Kyung Jean Yoon, Woojin Jeon, YeonWoo Yoo, Cheol Hyun An, and Cheol Seong Hwang, "Bipolar Resistive Switching in Amorphous SrTiO₃ Films Grown by Atomic Layer Deposition", Feb. 24-26, 한양대학교, 제 21 한국 반도체 학술대회 (2014) - poster.

2.2 International

1. Seol Choi, Byung Joon Choi, Taeyong Eom, Jae Hyuck Jang, **Woongkyu Lee** and Cheol Seong Hwang, "Growth and Crystallization Behavior of Ge Doped Sb_xTe_y Thin Films Deposited by a Plasma-enhanced CVD.", MRS spring meeting 2010 (poster), San Francisco Marriott, April 6 (2010) - poster
2. Taeyong Eom, Seol Choi, Byung Joon Choi, Sangho Rha, **Woongkyu Lee**, Cheol Seong Hwang and Moo Seong Kim, "Atomic Layer Deposition of $(GeTe_2)_x(Sb_2Te_3)_y$ Films Using Novel Precursors for Phase Change Memory.", MRS spring meeting 2010 (poster), San Francisco Marriott, April 6 (2010) - poster
3. Taeyong Eom, Seol Choi, Byung Joon Choi, Min Hwan Lee, Sang Ho Ra, **Woongkyu Lee**, Deok-Yong Cho, Moo-Sung Kim, Manchao Xiao, and Cheol Seong Hwang, "Thermal atomic layer deposition of $GeTe_2$ - Sb_2Te_3 films for the confined cell structured phase change memory", ALD 2010, Seoul, June 21~23 (2010) – oral
4. **Woongkyu Lee**, Sang Woon Lee, Jeong Hwan Han, Sora Han, Julien Gatineau and Cheol Seong Hwang, "Controlling initial growth behavior of ALD- $SrTiO_3$ films Using the interposed ALD- Al_2O_3 layers", ALD 2011, Cambridge, June 26~29 (2011) - poster

5. Sang Young Lee, **Woongkyu Lee**, Hyung-Suk Jung, Hyo Kyeom Kim and Cheol Seong Hwang, "The effects of ALD grown HfO₂ and TiO₂/passivation layer stacks on the electrical properties of metal gate/high-k Ge MOS capacitors", ALD 2011(posters), Cambridge, June 26~29 (2011) – oral
6. Jeong Hwan Han, **Woongkyu Lee**, Sora Han, Cheol Seong Hwang, "Deposition of Ru based electrodes using CVD/ALD for MIM capacitor of next generation DRAM device" EuroCVD 18, Kinsle, Co. Cork, Ireland, sept. 4~9,(2011) – oral
7. Woojin Jeon, Hyo Kyeom Kim, **Woongkyu Lee**, Yeon Woo Yoo, Jeong Hwan Han, and Cheol Seong Hwang, "Achieving EOT of 4.0 Å from Al-doped TiO₂ film with RuO₂ Top Electrode", ALD 2012, Dresden, Germany, June(17-20),June 18th (2012)-poster
8. Yeon Woo Yoo, Woojin Jeon, **Woongkyu Lee**, Jeong Hwan Han, and Cheol Seong Hwang, "Comparison between Atomic Layer Deposited TiO₂ Films on Various Substrates with Different Growth Temperature", ALD 2012, Dresden, Germany, June(17-20),June 19th (2012)-poster
9. Min Hyuk Park, Hyun Ju Lee, Yu Jin Kim, Jong Ho Lee, **Woongkyu Lee**, Han Joon Kim, and Cheol Seong Hwang, "Diode-Embedded Resistive Memory Using Stacked Ferroelectric/Dielectric Layer", WoDiM 2012, Dresden, Germany, 25th~27th June, 25th June (2012)-poster

10. **Woongkyu Lee**, Jeong Hwan Han, Woojin Jeon, Yeon Woo Yoo, Changhee Ko, Julien Gatineau and Cheol Seong Hwang, "ATOMIC LAYER DEPOSITION OF SrTiO₃ FILMS WITH Cp-BASED PRECURSORS FROM DRAM CAPACITORS", Nature Conference 2012, Aachen, Germany, June(17-20), June 18th (2012)-contribution talk
11. **Woongkyu Lee**, Jeong Hwan Han, Woojin Jeon, and Cheol Seong Hwang, "Recent Progress and current status of dielectrics for DRAM", WoDiM 2012, Dresden, Germany, 25th~27th June, 25th June (2012) - invited talk
12. Cheol Seong Hwang, Sang Woon Lee, Byung Joon Choi, Taeyong Eom, Jeong Hwan Han, Seong Keun Kim, Seul Ji Song, and **Woongkyu Lee**, "Uncommon aspects of atomic layer deposition processes for the growth of functional electronic materials" 2013 NIMS Conference, Japan, 01-03 July (2013)-Invited
13. Woojin Jeon, **Woongkyu Lee**, Yeon Woo Yoo, Cheol Hyun An and Cheol Seong Hwang, "Evaluating the Mechanism for Leakage Current Reduction of ALD TiO₂ film by Al-doping", ALD 2013, San Diego Marriott Marquis & Marina, San Diego, United States, July 28-31 (2013) – oral
14. **Woongkyu Lee**, Woojin Jeon, Yeon Woo Yoo, Cheol Hyun An and Cheol Seong Hwang, "Reducing Micro-defect Formation in Atomic Layer Deposited SrTiO₃ Films during Crystallization Annealing", ALD 2013, San Diego Marriott Marquis & Marina, San Diego, United States, July 28-31 (2013) – poster

15. An Cheol Hyun, Woojin Jeon, **Woongkyu Lee**, Yeon Woo Yoo and Cheol Seong Hwang, "Improving step coverage of SrRuO₃ film grown by combining ALD SrO and CVD RuO₂ or Ru layers", ALD 2013, San Diego Marriott Marquis & Marina, San Diego, United States, July 28-31 (2013) – poster
16. Yeon Woo Yoo, **Woongkyu Lee**, Woojin Jeon, Cheol Hyun An, Won Seok Han and Cheol Seong Hwang, "Atomic Layer Deposited ZrO₂ Films on Various Substrates with New Zr Precursor", ALD 2013, San Diego Marriott Marquis & Marina, San Diego, United States, July 28-31 (2013) – poster
17. Woojin Jeon, **Woongkyu Lee**, Yeon Woo Yoo, Cheol Hyun An, Cheol Seong Hwang, "Understanding the variations in leakage conduction mechanism of ALD TiO₂ film by Al-doping", CECAM-Workshop Functional oxides for emerging technologies, Bremen University, Bremen, Germany, Oct 14-18 (2013) - poster
18. **Woongkyu Lee**, Woojin Jeon, Yeon Woo Yoo, Cheol Hyun An, Cheol Seong Hwang, "Formation of micro-defects in atomic layer deposited SrTiO₃ films by rapid thermal annealing", CECAM-Workshop Functional oxides for emerging technologies, Bremen University, Bremen, Germany, Oct 14-18 (2013) – poster
19. Yeon Woo Yoo, **Woongkyu Lee**, Woojin Jeon, Cheol Hyun An, Cheol Seong Hwang, "Properties of atomic layer deposited ZrO₂ films on various substrates with new Zr precursor", CECAM-Workshop Functional oxides for emerging technologies, Bremen University, Bremen, Germany, Oct 14-18 (2013) – poster

20. Taehwan Moon, Min Hyuk Park, Han Joon Kim, Yu Jin Kim, **Woongkyu Lee**, Hyokyeom Kim and Cheol Seong Hwang, "The Effects of Evolution of Phases and Forming Gas Annealing on Ferroelectric Properties of Thin $\text{Hf}_{0.5}\text{Zr}_{0.5}\text{O}_2$ Films", MRS SPRING MEETING & EXHIBIT, San Francisco, California, April 21-25 (2014) - poster
21. Min Hyuk Park, Ju-Young Cho, Han Joon Kim, Yu Jin Kim, Deok Yong Cho, Hyo Kyeom Kim, **Woongkyu Lee**, Il-Hyuk Yu, Taehwan Moon, Tae Yeong Koo, Young-Chang Joo, and Cheol Seong Hwang, "The origin of the ferroelectricity in thin $\text{Hf}_{1-x}\text{Zr}_x\text{O}_2$ films: microstructure and in-plane tensile stress formed during island coalescence", MRS SPRING MEETING & EXHIBIT, San Francisco, California, April 21-25 (2014). – oral
22. Woojin Jeon, **Woongkyu Lee**, Yeon Woo Yoo, Cheol Hyun An, and Cheol Seong Hwang, "Initial Growth Behavior of Atomic Layer Deposited TiO_2 Film on $\text{RuO}_x(x=0\sim 2)$ Substrate", ALD 2014, Granvia Hotel, Kyoto, Japan, June 15-18 (2014) - oral
23. **Woongkyu Lee**, Woojin Jeon, Yeon Woo Yoo, Cheol Hyun An, Min Jung Chung, Taek-Mo Chung, Chang Gyoung Kim, Bo Keun Park, Sheby M. George, and Cheol Seong Hwang, "Atomic Layer Deposition of SrTiO_3 Films with $\text{Sr}(\text{demamp})(\text{tmhd})$ as Sr-precursor", ALD 2014, Granvia Hotel, Kyoto, Japan, June 15-18 (2014) - oral

24. Cheol Hyun An, Woojin Jeon, **Woongkyu Lee**, Yeon Woo Yoo, and Cheol Seong Hwang, "Pursuit of ALD possibility of Ru Thin Film with RuO₄ Precursor", ALD 2014, Granvia Hotel, Kyoto, Japan, June 15-18 (2014) - poster
25. Min Hyuk Park, Han Joon Kim, Yu Jin Kim, **Woongkyu Lee**, Taehwan Moon, and Cheol Seong Hwang, "Ferroelectricity in HfO₂-based films", Electroceramics XIV, Bucharest Romania, June 16-20th (2014). –invited talk

Abstract (in Korean)

현재 양산에 적용되고 있는 DRAM 커패시터의 유전물질은 누설전류를 낮추기 위해 Al_2O_3 를 삽입한 ZrO_2 를 사용하고 있다. 그러나 20 nm 급 이하 디자인 룰을 따르도록 DRAM 소자를 집적화하기 위해서는 현재보다 더 큰 유전율을 갖는 재료로 대체할 필요가 있다. 유전물질의 후보로는 Ta_2O_5 , TiO_2 등 여러 가지가 있으며, SrTiO_3 (STO) 역시 차세대 유전물질로 각광받고 있다. STO는 에너지 밴드갭은 상대적으로 작은 편이지만, 페로브스카이트 구조로 결정화되었을 때 뛰어난 유전상수를 갖기 때문에, 현재 어려움에 직면한 DRAM의 소형화 문제를 극복할 수 있을 것으로 생각된다. 그리고 STO를 DRAM 커패시터의 유전물질로 적용하기 위해서는, 좋은 단차피복성을 위한 원자층증착방법(Atomic Layer Deposition, ALD) 공정, 낮은 누설전류를 위한 루테튬과 같은 귀금속 전극과의 조화, in-situ 결정화를 위한 고온 성장의 세 가지 요건이 고려되어야 한다.

본 학위 논문에서는 $\text{Sr}(\text{}^i\text{Pr}_3\text{Cp})_2$, $[\text{Sr}(\text{demamp})(\text{tmhd})]_2$, $\text{Ti}(\text{O-}^i\text{Pr})_2(\text{tmhd})_2$, $\text{Ti}(\text{Me}_5\text{Cp})(\text{OMe})_3$ 와 같은 다양한 종류의 Sr 과 Ti 전구체를 이용하여 STO 박막을 ALD 방법으로 성장시킨 연구를 담고 있다. 이 전구체들의 다양한 조합을 이용한 STO 박막 증착 공정의 성장거동을 연구하였으며, 금속-절연체-금속 (metal-insulator-

metal, MIM) 구조 커패시터 제작을 통한 전기적 특성 분석 등 여러 가지 박막 특성 역시 평가하였다.

첫 번째로, $\text{Sr}(\text{Pr}_3\text{Cp})_2$ 과 $\text{Ti}(\text{O}-\text{Pr})_2(\text{tmhd})_2$ 를 각각 Sr과 Ti 전구체로 사용한 ALD STO에 대한 연구를 진행하였다. 동일한 전구체들을 사용한 선행 연구에 의하면, Ru 기판에 STO 박막을 증착할 때 성장 초기에 Sr 원소의 과잉 증착 현상이 발견되었다. 이러한 Sr 원소의 초기 과잉 성장은 두께의 미세 조절을 어렵게 할 뿐만 아니라 MIM 커패시터 제작 시 전기적 특성의 열화의 원인이 되는 SrCO_3 의 생성을 유발하였다. Sr의 과잉성장은 기체상의 $\text{Sr}(\text{Pr}_3\text{Cp})_2$ 과 Ru 기판에 포함되어 있는 산소 이온 간의 격렬한 반응에 의해 나타났기 때문에, 선행연구에서는 3 nm 이상의 두께의 TiO_2 층을 STO 성장 전에 증착하였다. 이러한 방법은 Sr의 초기 과잉 성장 현상을 성공적으로 억제할 수 있었으나, 전체 유전막의 물리적 두께가 10nm 밖에 되지 않는 것을 감안하였을 때 3 nm나 하부 TiO_2 박막에 할애하는 것은 DRAM 커패시터의 총 유전 특성에서 큰 손실을 가져왔다. 그리하여 본 연구에서는 TiO_2 보다 낮은 산소 확산계수를 갖는 Al_2O_3 를 TiO_2 대신에 차단층에 적용하여 이러한 문제를 해결하려 하였다. 그 결과 0.4 nm 두께의 Al_2O_3 층만으로도 눈에 띄게 Sr의 과잉 성장 현상을 방지할 수 있었으며, Al_2O_3 층 1 nm로도 TiO_2 층 3 nm와 동일한 차단 효과를 가짐을 알 수 있었다. 또한 3 nm 두께의 STO 박막을 먼저 증착한 뒤 열처리하여

결정화시킨 seed 층 위에 STO 박막을 370 °C에서 성장시키자 상부에 성장된 박막 역시 별다른 후열처리 없이 in situ로 결정화되었다. 1 nm 두께 Al₂O₃/Ru 위에 성장한 STO는 등가산화막두께 vs. 물리적 두께 그래프의 기울기를 통해 계산해본 결과 벌크유전율이 173이나 되었다. 그러나 Al₂O₃ 층의 정전용량에 대한 악영향은 TiO₂ 층보다 심각한 것으로 판단되었다.

다음으로, Cp계열의 전구체인 Sr(ⁱPr₃Cp)₂와 Ti(Me₅Cp)(OMe)₃를 이용한 ALD STO 박막에 대한 연구도 진행하였다. Ti(O-ⁱPr)₂(tmhd)₂에 비하여 더 반응성이 강한 새로운 Ti 전구체는 원하지 않는 Sr의 과잉증착현상을 in situ로 둔화시켰으며, SrCO₃의 생성 역시 억제되었다. 이러한 현상에 대한 자세한 예상 메커니즘을 제시하였다. 새로운 Cp 계열 전구체 공정을 이용하여 전기적 특성에 손실을 가져오는 반응차단층 없이도, SrO와 TiO₂의 sub-cycle 비율을 조절함으로써 조성이 잘 맞는 STO 박막을 얻을 수 있었다. 그 결과 RuO₂/STO/Ru 커패시터의 최소등가산화막두께를 0.39 nm 까지 줄이며 낮은 누설전류밀도(약 9x10⁻⁸A/cm²)를 얻을 수 있었다. 이는 이전 결과에 비해 약 46%의 정전용량을 향상시킨 결과다. 그러나 벌크유전율은 약 100 정도 밖에 되지 않아서, 커패시터의 전기적 특성을 더 향상시킬 수 있는 여지가 남아있음을 알 수 있었다. 박막에 대한 면밀한 분석을 통해 STO 박막 내에 미세결함이 존재함을 확인할 수 있었다. 이러한 결함은 STO 박막과 기판

사이의 열팽창계수 차이에 의해 발생된 응력에 의한 것이었으며, seed 층의 결정화 열처리 후 냉각속도를 조절함으로써, 비록 계면특성이 다소 열화되기는 하였지만, 약 135까지 벌크유전율을 향상시킬 수 있었다.

마지막으로, $[\text{Sr}(\text{demamp})(\text{tmhd})]_2$ 와 $\text{Ti}(\text{Me}_5\text{Cp})(\text{OMe})_3$ 를 각각 Sr과 Ti 전구체로 사용한 STO 증착에 대해 연구하였다. 이 Sr 전구체를 이용한 공정은 SrO 박막의 최종증착속도가 $\text{Sr}(\text{Pr}_3\text{Cp})_2$ 와 비슷한 수준이었지만, 성장초반에 어떠한 비정상거동도 나타나지 않았다. 비록 STO 박막의 성장속도는 이전에 비하여 조금 줄어들었지만, SrCO_3 는 전혀 생성되지 않았을 뿐만 아니라, 감소된 증착속도는 오히려 조밀한 박막을 성장시켜서 결정화 열처리 후에도 미세결함이 생성되지 않았다. 새로 개발된 STO 증착 공정은 이상적인 ALD 성장거동을 통해 중형비 10:1의 3차원 홀 구조에서도 균일한 두께와 조성의 박막을 확보할 수 있었다. 또한 벌크유전율이 약 143이나 되었기 때문에, 계면 특성 향상을 통해 뛰어난 전기적 특성을 확보할 수 있을 것임을 예상할 수 있었다.

결론적으로, Al_2O_3 층을 삽입하여 Sr 원소의 비정상적인 초기과잉 성장을 억제함으로써 SrCO_3 생성을 배제하고, 이미 결정화된 STO seed 층을 이용하여 in-situ로 결정화된 STO 박막을 성장시켰다. 또한, 더 반응성이 큰 Ti 전구체를 이용하여, 어떠한 차단층 없이도 조성이 잘 맞는 STO 박막을 증착할 수 있었으며, 등가산화막두께

0.39 nm와 누설전류밀도 $9 \times 10^{-8} \text{ A/cm}^2$ 의 전기적 특성을 확보할 수 있었고, 열처리 조건을 조절하여 미세구조 역시 개선할 수 있었다. 마지막으로, 적절한 반응성을 갖는 새로운 Sr 전구체를 이용하여 이상적인 ALD 성장거동을 확보하였으며 만족할만한 유전특성을 얻을 수 있었고, 중형비 10:1의 홀 구조에서 균일한 STO 박막을 얻을 수 있었다.

주요어: 디램, 커패시터, 유전물질, 전극, SrO, TiO₂, SrTiO₃, Ru, RuO₂, O₃, H₂O, 원자층증착방법, 고유전율, 등가산화막두께, 정전용량, 누설전류, in-situ 결정화

학번: 2009-23050

이 용 규